STRUCTURE OF TURBULENT FLOW IN A ROD BUNDLE

by
Armel Evrard Goa Don

A thesis submitted to
the Faculty of Graduate and Postdoctoral Studies
in partial fulfillment of
the requirements for the degree of

MASTER OF APPLIED SCIENCE

in Mechanical Engineering

Ottawa-Carleton Institute for Mechanical and Aerospace Engineering
University of Ottawa

Abstract

The structure of turbulence in the subchannels of a large-scale 60° section of a CANDU 37-rod bundle was studied at Reynolds numbers equal to 50,000, 100,000 and 130,000. Measurements were conducted at roughly 33.81 rod diameters from the inlet of the rod bundle using single-point, two-component hot-wire anemometry. Analysis of the axial velocity signal indicated a weak effect of Reynolds number on the axial velocity distribution and a bulging of axial velocity contours toward the narrow gaps. The normalised normal Reynolds stresses and the normalised turbulent kinetic energy were found to decrease as the Reynolds number increased. The radial Reynolds shear stress varied linearly with radial distance from the rod, crossing zero at the location of local maximum of the axial velocity. This stress was symmetric about the central rod whereas the azimuthal Reynolds shear stress was anti-symmetric. The Reynolds number effect was weak but measurable on the integral length scales of the axial and radial velocity fluctuations but negligible on the integral length scale of the azimuthal velocity fluctuations, especially in the gap regions. The Taylor and Kolmogorov microscales increased from the wall toward the centre of the subchannel and decreased as the Reynolds number increased. The wall shear stress stress distribution around the central rod indicated no effect of Reynolds number, when normalized by the corresponding average. The wall shear stress reached local minima at rod-wall and rod-rod gaps and local maxima in the open flow regions. Vortex streets were generated within the subchannels very close to the inlet of the rod bundle. The convection speed and frequency of the vortex street were found to increase proportionately to Reynolds number, whereas the vortex spacing was not affected by the Reynolds number.

Acknowledgements

I am very grateful to the many friends and family for their support and tolerance of the unremitting unsocial behaviour caused by the countless hours and days that this thesis consumed. Thanks also to my mother whose support I could always rely on.

I wish to express my deepest appreciation to Dr. Stavros Tavoularis for his full support, great interest in these studies as well as his guidance throughout my thesis. Without his persistent help, this dissertation would not have been possible.

I am indebted to Dr. Dongil Chang and Dr. Amir Behnamian whose knowledge and experience I have frequently relied on.

My sincere gratitude to the Department of Mechanical Engineering and the staff of the machine shop for their support.

Finally, I would like to thank the Engineering Research Council of Canada and the Atomic Energy of Canada Limited for financially supporting me and the project with research grants.

Table of Contents

Abstract i

Acknowledgements ii

Table of Contents iii

List of Tables vi

List of Figures vii

Nomenclature xiii

Chapter 1 Introduction 1

1.1 CANDU nuclear reactors 1

1.2 Motivation and objectives 2

1.3 Plan of thesis 3

Chapter 2 Literature review 4

2.1 Experimental studies 4

2.1.1 Wall shear stress measurements 4

2.1.2 Measurements of turbulence structure in rod bundles 6

2.1.3 Development of large-scale coherent vortices 7

2.2 Computational studies 8

Chapter 3 Background and Definitions 10

3.1 Hydraulic Diameter 10

3.2 Bulk velocity and bulk Reynolds number 12

3.3 Coordinate system 12

3.4 Turbulent kinetic energy 13

3.5 Turbulent length scales 13

3.6 Reynolds stress tensor 15
3.7 Coherent structures 15

Chapter 4 Experimental facility, instrumentation and measurement procedures 16

4.1 Rod bundle facility 16
4.2 Calibration jet 22
4.3 Instrumentation 24
4.3.1 Hot-wire anemometry 24
4.3.2 Pitot-static tube and Preston tube 26
4.3.3 Resistance thermometers 27
4.3.4 Weather forecast board and estimation of air density 27
4.4 Calibration techniques 28
4.4.1 Pressure transducer calibration 28
4.4.2 Cross-wire probe calibration and signal analysis method . . . 29
4.5 Signal conditioning and data acquisition systems 35
4.5.1 Signal conditioning 35
4.5.2 Data acquisition systems 35
4.6 Measurement procedures 36
4.6.1 Estimation of the correction factor and the bulk velocity . . . 36
4.6.2 Cross-wire velocity measurements 37
4.6.3 Wall shear stress measurements 38
4.6.4 Detection of Coherent structures 39
4.7 Hot-wire resolution and velocity measurement uncertainty 41
4.7.1 Hot-wire resolution 41
4.7.2 Velocity measurement uncertainty 41

Chapter 5 Experimental results and Discussion 44

5.1 Incoming flow conditions 44
5.2 Mean flow symmetry 46
5.3 Mean axial velocity distribution 46

5.4 Normal Reynolds stress distribution 53
5.5 Reynolds shear stress distribution 64
5.6 Turbulent kinetic energy distribution 71
5.7 Reynolds stress tensor anisotropy 75
5.8 Turbulent length scales 77
5.8.1 Integral length scale 77
5.8.2 Taylor microscale 88
5.8.3 Kolmogorov microscale 92
5.9 Wall shear stress variation 96
5.10 Comparison with pipe flows 98
5.11 Coherent structure characteristics 105

Chapter 6 Conclusion **111**
6.1 Summary of the results 111
6.2 Main contribution and recommendations for future work 112

References **114**

List of Tables

3.1	Specifications of an actual, a large-scale and the experimental model of a CANDU rod bundle.	11
4.1	Perforated plate configurations.	19
4.2	Positions of port centres on the top cover of the test section. . .	21
4.3	Cross-wire velocity measurements settings.	38
4.4	Measured and corrected values of $\overline{(\partial u/\partial x)^2}$, $\overline{(\partial u_r/\partial x)^2}$, the Taylor microscale and the Kolmogorov microscale. The corrected values are in bold.	41
4.5	Relative uncertainty (%) estimates of measured properties. . .	43
5.1	Summary of the wall shear stress and friction factor measurement	97

List of Figures

3.1	Cross-section of a 37-rod CANDU reactor bundle.	11
3.2	Illustration of the rod bundle's coordinate system.	13
4.1	Rod-bundle facility at the University of Ottawa.	16
4.2	Schematic diagram of the diffuser and the plenum; front and top views; all dimensions are in mm.	18
4.3	Test section inlet with endplate viewed from the plenum interior; dimensions are in mm and the rod diameter is $D = 168.3$ mm.	20
4.4	Rod bundle traversing system	22
4.5	Calibration jet. Picture from Bailey's thesis.	23
4.6	Right angle probe calibration traverse.	24
4.7	Sketch of the right angle cross-wire probe. Dimensions are in mm.	25
4.8	Sketch of the Preston tube. Not to scale.	26
4.9	Example of pressure transducer calibration results. Solid line indicates linear curve fit.	28
4.10	Example of sensor inclination angle result. Solid line indicates 5^{th} order polynomial curve fit.	30
4.11	Example of yaw calibration result. Solid line indicates linear curve fit.	32
4.12	Example of velocity calibration results. Solid lines indicate King's Law curve fits.	33
4.13	Example of velocity tests after calibration. Solid line indicates linear curve fit.	34
4.14	Throat area of the contraction.	37
4.15	Validation of Preston tube technique.	39
4.16	Representative cross-flow velocity cross-correlation coefficient.	40

5.1 Dimensionless mean velocity profiles inside the plenum, $3.15D$ upstream of the test section inlet and at $w/W = 0.23$ ($\bigcirc$), 0.43 ($\times$) and 0.57 ($\triangle$). 45

5.2 Dimensionless fluctuating velocity profiles inside the plenum, $3.15D$ upstream of the test section inlet and at $w/W = 0.23$ ($\bigcirc$), 0.43 ($\times$) and 0.57 ($\triangle$). 45

5.3 Dimensionless integral length scale profiles inside the plenum, $3.15D$ upstream of the test section inlet and at $w/W = 0.23$ ($\bigcirc$), 0.43 ($\times$) and 0.57 ($\triangle$). 46

5.4 Radial profiles of the normalised mean axial velocity at various azimuthal locations and $Re = 50,000$ ($\bigcirc$), $100,000$ ($\times$) and $130,000$ ($\triangle$). 49

5.5 Isocontour plots of the normalised mean axial velocity for (a) $Re = 50,000$, (b) $Re = 100,000$, (c) $Re = 130,000$. 51

5.6 Local maximum axial velocity variation around the central rod for $Re = 50,000$ ($\bigcirc$), $100,000$ ($\times$) and $130,000$ ($\triangle$). Solid lines indicate fourth-order polynomial curve fits. 52

5.7 Variation of the normalised local maximum axial velocity with Reynolds number at $\phi = 0°$ ($\bigcirc$), $105°$ ($\times$) and $180°$ ($\triangle$). . . . 52

5.8 Radial profiles of the normalised axial Reynolds stress at various azimuthal locations and for $Re = 50,000$ ($\bigcirc$), $100,000$ ($\times$) and $130,000$ ($\triangle$). 55

5.9 Isocontour plots of the normalised axial Reynolds stress for (a) $Re = 50,000$, (b) $Re = 100,000$, (c) $Re = 130,000$. 57

5.10 Radial profiles of the normalised radial Reynolds stress at various azimuthal locations and for $Re = 50,000$ ($\bigcirc$), $100,000$ ($\times$) and $130,000$ ($\triangle$). 58

5.11 Isocontour plots of the normalised radial Reynolds stress for (a) $Re = 50,000$, (b) $Re = 100,000$, (c) $Re = 130,000$. 60

5.12 Radial profiles of the normalised azimuthal Reynolds stress at various azimuthal locations and for $Re = 50,000$ ($\bigcirc$), $100,000$ ($\times$) and $130,000$ ($\triangle$). 61

5.13 Isocontour plots of the normalised azimuthal Reynolds stress for (a) $Re = 50,000$, (b) $Re = 100,000$, (c) $Re = 130,000$. . . 63

5.14 Radial profiles of the normalised radial Reynolds shear stress at various azimuthal locations and for $Re = 50,000$ ($\bigcirc$), $100,000$ ($\times$) and $130,000$ ($\triangle$). 65

5.15 Isocontour plots of the radial Reynolds shear stresses $\overline{uu_r}$ for (a) $Re = 50,000$, (b) $Re = 100,000$, (c) $Re = 130,000$. 67

5.16 Radial profiles of the normalised azimuthal Reynolds shear stress at various azimuthal locations and for $Re = 50,000$ ($\bigcirc$), $100,000$ ($\times$) and $130,000$ ($\triangle$). 68

5.17 Isocontour plots of the normalised azimuthal Reynolds shear stress for (a) $Re = 50,000$, (b) $Re = 100,000$, (c) $Re = 130,000$. 70

5.18 Radial profiles of the normalised turbulent kinetic energy at various azimuthal locations and for $Re = 50,000$ ($\bigcirc$), $100,000$ ($\times$) and $130,000$ ($\triangle$). 72

5.19 Isocontour plots of the normalised turbulent kinetic energy for (a) $Re = 50,000$, (b) $Re = 100,000$, (c) $Re = 130,000$. 74

5.20 Representative radial profiles of the axial Reynolds stress anisotropy for $Re = 50,000$ ($\bigcirc$), $100,000$ ($\times$) and $130,000$ ($\triangle$). 76

5.21 Representative radial profiles of the radial Reynolds stress anisotropy for $Re = 50,000$ ($\bigcirc$), $100,000$ ($\times$) and $130,000$ ($\triangle$). 76

5.22 Representative radial profiles of the azimuthal Reynolds stress anisotropy for $Re = 50,000$ ($\bigcirc$), $100,000$ ($\times$) and $130,000$ ($\triangle$). 77

5.23 Representative radial profiles of the axial Reynolds stress anisotropy for $Re = 50,000$ ($\bigcirc$), $100,000$ ($\times$) and $130,000$ ($\triangle$). 77

5.24 Radial profiles of the streamwise Eulerian integral length scale of the axial velocity fluctuations at various azimuthal locations and for $Re = 50,000$ ($\bigcirc$), $100,000$ ($\times$) and $130,000$ ($\triangle$). . . . 79
5.25 Isocontour plots of the normalised streamwise Eulerian integral length scale of the axial velocity fluctuations for (a) $Re = 50,000$, (b) $Re = 100,000$, (c) $Re = 130,000$. 81
5.26 Radial profiles of the streamwise Eulerian integral length scale of the radial velocity fluctuations at various azimuthal locations and for $Re = 50,000$ ($\bigcirc$), $100,000$ ($\times$) and $130,000$ ($\triangle$). . . . 82
5.27 Isocontour plots of the normalised streamwise Eulerian integral length scale of the radial velocity fluctuations for (a) $Re = 50,000$, (b) $Re = 100,000$, (c) $Re = 130,000$. 84
5.28 Radial profiles of the streamwise Eulerian integral length scale of the azimuthal velocity fluctuations at various azimuthal locations and for $Re = 50,000$ ($\bigcirc$), $100,000$ ($\times$) and $130,000$ ($\triangle$). 85
5.29 Isocontour plots of the normalised streamwise Eulerian integral length scale of the azimuthal velocity fluctuations for (a) $Re = 50,000$, (b) $Re = 100,000$, (c) $Re = 130,000$. 87
5.30 Radial profiles of the turbulent Reynolds number for $Re = 50,000$ ($\bigcirc$), $100,000$ ($\times$) and $130,000$ ($\triangle$). 88
5.31 Radial profiles of the streamwise Taylor microscale at various azimuthal locations and for $Re = 50,000$ ($\bigcirc$), $100,000$ ($\times$) and $130,000$ ($\triangle$). 89
5.32 Isocontour plots of the streamwise Taylor microscale for (a) $Re = 50,000$, (b) $Re = 100,000$, (c) $Re = 130,000$. 91
5.33 Radial profiles of the dissipation rate for $Re = 50,000$ ($\bigcirc$), $100,000$ ($\times$) and $130,000$ ($\triangle$). 92
5.34 Radial profiles of the Kolmogorov microscale at various azimuthal locations and for $Re = 50,000$ ($\bigcirc$), $100,000$ ($\times$) and $130,000$ ($\triangle$). 93

5.35 Isocontour plots of the Kolmogorov microscale for (a) Re = $50,000$, (b) $Re = 100,000$, (c) $Re = 130,000$. 95
5.36 Azimuthal wall shear stress variations for $Re = 50,000$ ($\bigcirc$), $100,000$ ($\times$) and $130,000$ ($\triangle$). The dashed lines represent the narrow gap locations and the solid lines are extrapolation curves. 97
5.37 Friction factors in the present study f ($\bullet$) and $\hat{f}$ ($\bigcirc$) and those by Subbotin et al. [1971] ($\square$), Kjellström [1974] ($\triangle$), Trupp and Azad [1975] ($\times$) and Ouma and Tavoularis [1991] ($+$) 98
5.38 Radial profiles of the normalised mean axial velocity. Present experiment: $Re = 50,000$ ($\bigcirc$), $100,000$ ($\times$) and $130,000$ ($\triangle$). Pipe flow: $Re = 50,000$ (—) and $500,000$ ($--$). 100
5.39 Radial profiles of the normalised axial fluctuating velocity. Present experiment: $Re = 50,000$ ($\bigcirc$), $100,000$ ($\times$) and $130,000$ ($\triangle$). Pipe flow: $Re = 50,000$ (—) and $500,000$ ($--$). 101
5.40 Radial profiles of the normalised radial fluctuating velocity. Present experiment: $Re = 50,000$ ($\bigcirc$), $100,000$ ($\times$) and $130,000$($\triangle$). Pipe flow: $Re = 50,000$ (—) and $500,000$ ($--$). 102
5.41 Radial profiles of the normalised azimuthal fluctuating velocity. Present experiment: $Re = 50,000$ ($\bigcirc$), $100,000$ ($\times$) and $130,000$ ($\triangle$). Pipe flow: $Re = 50,000$ (—) and $500,000$ ($--$). 103
5.42 Radial profiles of the normalised radial Reynolds shear stress. Present experiment: $Re = 50,000$ ($\bigcirc$), $100,000$ ($\times$) and $130,000$ ($\triangle$). Pipe flow: $Re = 50,000$ (—) and $500,000$ ($--$). 104
5.43 Sketch of idealized gap vortex street, according to Meyer and Rehme [1994]. Sketch from Choueiri [2014]. 105
5.44 Cross-flow power spectra in the centre of the rod-wall gap along the test section for (a) $Re = 50,000$, (b) $Re = 100,000$ and (c) $Re = 130,000$. 107
5.45 Peak frequencies of the cross-flow power spectra for $Re = 50,000$ ($\bigcirc$), $100,000$ ($\times$) and $130,000$ ($\triangle$). 108

5.46 Autocorrelation coefficient of the cross velocity fluctuations at $x/D = 33.81$ for $Re = 50,000$ (—), $100,000$ ($--$) and $130,000$ ($\cdots$).108
5.47 Strouhal number variation along the test section for $Re = 50,000$ ($\bigcirc$), $100,000$ ($\times$) and $130,000$ ($\triangle$). 109
5.48 Variation of the normalized convection speed of the coherent vortices with Reynolds number. Solid line indicates $U_c/U_b = 1.16$.109
5.49 Variation of the normalised wavelength of the coherent vortices with Reynolds number. Solid line indicates $\lambda_c/D = 4.95$. . . . 110

Nomenclature

A	cross-sectional area; also calibration constant
A_0	calibration constant
A_c	cross-sectional area of the intake contraction throat
A_i	calibration constant; also jet inlet cross-sectional area
A_o	jet out cross-sectional area
A_r	subchannel area
A_t	cross-sectional area of the experimental model
B	calibration constant
B_0	calibration constant
B_i	calibration constant
C	calibration constant
D	rod diameter
D_h	hydraulic diameter
E	hot-wire signal
E_{offset}	DC offset
E_{out}	anemometer output voltage
E_t	pressure transducer output voltage
E_θ	yaw voltage
H	ambient room humidity; also plenum height

L_r	streamwise integral length scale of the radial velocity fluctuations
L_u	streamwise integral length scale of the axial velocity fluctuations
L_ϕ	streamwise integral length scale of the azimuthal velocity fluctuations
P	wetted perimeter; also pitch distance
P_a	ambient room pressure
P_d	partial pressure of dry air
P_v	partial pressure of water vapour
Q	flow rate
R	resistance of the RTD at T
R_T	radius of CANDU 37-rod pressure tube
R_a	specific gas constant of water vapour
R_d	specific gas constant of dry air
R_o	resistance of RTD at 0°C
Re_b	bulk Reynolds number
Re_λ	Turbulent Reynolds number
St	Strouhal number
T	Temperature
T_a	ambient room temperature
T_f	fluid temperature
T_w	temperature of hot-wire sensor

U	instantaneous axial velocity
U_b	total bulk velocity
$\hat{U}_b$	subchannel bulk velocity
U_c	convection speed of the coherent vortices; also velocity at the centre of the intake contraction throat
U_{jet}	jet velocity
U_m	local maximum velocity
U_{max}	maximum velocity
U_p	plenum velocity
U_τ	friction velocity
V_e	effective cooling velocity
X	axial yaw function
Y	radial yaw function
b	bias error
c	correction factor
d	Preston tube inner diameter
f	average friction factor; also frequency
$\hat{f}$	average local friction factor
f_i	yaw function
f_p	peak frequency of coherent vortices
g	anemometer gain

g_i	yaw function
i	hot-wire sensor identifier
k	turbulent kinetic energy; also effective cooling coefficient
m_r	radial normal Reynolds stress anisotropy invariant
m_u	axial normal Reynolds stress anisotropy invariant
m_{ur}	radial Reynolds shear stress anisotropy invariant
m_ϕ	azimuthal normal Reynolds stress anisotropy invariant
n	calibration coefficient
n_0	calibration constant
n_i	calibration constant
p	precision error
t	time
u'	fluctuating component of the axial velocity
u'_r	fluctuating component of the radial velocity
u'_ϕ	fluctuating component of the azimuthal velocity
$\overline{u^2}$	variance of the instantaneous axial velocity
$\overline{u_r^2}$	variance of the instantaneous radial velocity
$\overline{u_\phi^2}$	variance of the instantaneous azimuthal velocity
x	distance from test section inlet
y_m	radial distance the rod surface and the subchannel midline

Greek symbols

ΔP	pressure difference
α	yaw angle
$\overline{\alpha}$	angle of hot-wire sensor
δ	measurement uncertainty
ϵ	dissipation rate of turbulent kinetic energy
ϵ_r	radial eddy viscosity
ϵ_ϕ	peripheral eddy viscosity
η	Kolmogorov microscale
θ	calibrator pitch angle
θ_{max}	pitch angle corresponding to maximum voltage
λ	Taylor microscale
λ_c	wavelength of the coherent vortices
μ	dynamic viscosity of air
ν	kinematic viscosity of air
ρ	air density
τ	separation time
τ_w	wall shear stress
$\tau_{w,av}$	average wall shear stress
ϕ	peripheral coordinate

Other Notation

$'$	RMS fluctuations
$\overline{\quad}$	time average
∂	partial derivative

Acronyms

PWR	Pressurized Water Reactor
GCR	Gas Cooled Reactor
BWR	Boiled Water Reactor
PHWR	Pressurized Heavy Water Reactor
RTD	Resistance Thermometer Detector
CANDU	CANadian Deuterium Uranium

Chapter 1

Introduction

1.1 CANDU nuclear reactors

Between the late 1950s and the early 1970s, the nuclear power industry grew very rapidly. Several nuclear reactor designs and concepts were investigated to demonstrate how nuclear fission could be harnessed to produce electrical energy for both industrial and residential use. Those reactors can be classified into four main categories: Gas Cooled Reactors (GCR), Boiling water Reactors (BWR), Pressurized Water Reactors (PWR) and Pressurized Heavy Water Reactors (PHWR). Regardless of their classification, the basic mode of operation of most nuclear reactors is the same: coolant flowing through the core of the reactor removes heat produced by nuclear fission and conveys it to a steam generator. The steam drives a turbine coupled to a generator, which produces electricity.

One successful model of the PHWR reactor is the CANadian Deuteurium Uranium (CANDU) reactor developed by the Atomic Energy of Canada Limited (AECL; currently Canadian Nuclear Laboratories - CNL).

The core of a CANDU nuclear reactor (Calandria) consists of typically 380 Zirconium alloy pressure tubes, 6 m in length, 103 mm in diameter and 4 mm thick. Each pressure tube contains twelve fuel bundles stacked end to end. Each fuel bundle has 37 identical fuel elements radially arranged about the axis of the bundle. Each fuel rod contains natural uranium fuel pellets loaded in a 500 mm long, 13.08 mm in diameter Zirconium alloy tube. The rods are cooled by heavy water (D_2O) flowing axially in the subchannels formed between the rods or between the rods and the inner wall of the pressure tube.

The overall efficiency of the reactor depends on the performance of the fuel bundles, which in turn relies on the flow structure, and temperature distribution in the subchannels. Therefore, an accurate prediction of the flow and temperature fields in

the subchannels is critical for the safe and reliable operation of the nuclear power plant.

1.2 Motivation and objectives

In tightly packed rod bundles, such as the 37-rod bundle of the CANDU reactor, flow and heat transfer phenomena are complicated by the formation of vortex networks, which contribute significantly to the mixing of streams in different subchannels across narrow gaps. A good knowledge of the effects of these vortices on the flow structure is key to improving current thermalhydraulics codes and on-going numerical studies. The Reynolds number in rod-bundles of an operating CANDU reactor is typically of the order of 5×10^5. During different accident scenarios, this Reynolds number can drop to much lower values, in addition to be subjected to a wide range of dynamic conditions. Although a large number of experimental and computational studies have examined flows in rod bundles, the effect of Reynolds number within the entire range of interest has not been documented sufficiently, particularly as far as the structure of turbulence and the development of vortex networks are concerned. The present work aims at contributing to our understanding and predictive ability of these phenomena. The specific objectives of this study can be summarized as follows:

- Investigate the formation of coherent structures along a rod bundle.
- Study the effects of Reynolds number on turbulent flow characteristics in a rod bundle.
- Provide an extensive set of measurement data that can be used to validate subchannel codes and CFD analyses.

The model of the rod bundle used in this study was made sufficiently large to permit insertion of various measurement probes into the subchannels with limited flow disturbance. The experiment was carried out in two main stages. The first stage consisted of measuring turbulence parameters and the wall shear stress for Reynolds numbers equal to 50,000, 100,000 and 130,000. The second stage consisted of studying the frequency, convection speed, and spacing of the coherent structures.

1.3 Plan of thesis

In addition to the introductory chapter, this thesis includes five other chapters. Chapter 2 is a review of previous experimental and numerical studies related to turbulent flows in various non-circular channels. Some background information and definitions of the turbulent statistics under investigation are provided in Chapter 3. Chapter 4 describes the experimental facility used in the present work, while Chapter 5 presents the experimental results and related discussion. A summary and the main contributions of this work as well as some recommendations for future work are presented in Chapter 6.

Chapter 2

Literature review

The design, operation and safety analysis of nuclear rod bundles require knowledge of the turbulent flow structure and temperature field in the subchannels. Research investigating the turbulent flow structure through rod bundles has been conducted both experimentally and numerically in various arrays of rod configurations. This research is vital to improving the thermal hydraulic performance of current nuclear facilities and design better facilities for the future.

Generally, experiments and numerical studies on nuclear rod bundles focus on two main aspects: heat transfer and turbulent flow structure. This study, however, is only concerned about the latter. For this reason, this literature review solely summarises previous findings related to turbulent flows in rod bundles. Comprehensive literature reviews of the heat transport and temperature distribution in rod bundles have been presented by many authors including Guellouz [1989].

2.1 Experimental studies

2.1.1 Wall shear stress measurements

In nuclear thermalhydraulics, the wall shear stress is one of the key parameters used to assess methods to predict the turbulent flow behaviour as well as the heat transfer and consequently the performance of nuclear fuel bundles. One of the first wall shear stress and friction factor measurements in rod bundles was conducted by Gunn and Darling [1963]. They found that, for turbulent flows, the friction factors for all channels of their test rig, which consisted of a square array cluster of four rods, were lower than for a pipe flow. They also investigated the friction factor for laminar flows in non-circular channels and reported that it obeyed the relationship

$$f = \frac{K}{Re} \tag{2.1}$$

where K is a geometry factor. Gunn and Darling [1963] observed that the transition to turbulence in non-circular channels appeared to take place in a series of stages and at much lower Reynolds number than in circular pipes.

Trupp and Azad [1975] measured the wall shear stress distribution and found that the local wall shear stresses did not increase monotonically from the narrow gap toward the open channel. They suggested that the presence of secondary flows within the subchannels may be affecting the wall shear stress distribution. They also reported higher friction factors in non-circular channels than in pipe flows at similar Reynolds numbers.

Unlike Trupp and Azad [1975], who reported the presence of secondary flow in their subchannel, Fakory and Todreas [1979] found no detectable evidence of secondary flow from their wall shear stress measurements. They found the wall shear stress to be dependent on the flow area with the highest stress occurring at the largest flow area. This is consistent with the assumption that the velocity gradient near the wall will increase with increasing channel size as a result of high mass flow and momentum. They also observed no significant effect of the Reynolds number on the distribution the normalized wall shear stresses. Nevertheless, they reported the Reynolds number to have a significant effect on the static pressure, which they found to be non-uniform around the rod. Fakory and Todreas [1979] concluded that this non-uniformity was incompatible with most analytical studies, which assume that the gradient of static pressure at the periphery of the subchannel is uniform.

Ouma and Tavoularis [1991] measured the wall shear stress distribution around the periphery of the central rod of a 5-rod segment of a 37-rod CANDU nuclear bundle model using a Preston tube. They found that the distribution had local minima in the narrow gap regions and local maxima near the open flow regions. They reported that the stresses at the rod-rod gaps were greater than those in the rod-wall gaps. They also observed that a decrease in the gap size resulted in a decrease of the wall shear stress. Similar observations were reported by Guellouz and Tavoularis [2000], who studied the effects of rod spacing on wall shear stresses using a hot-wire film.

2.1.2 Measurements of turbulence structure in rod bundles

Although various experimental studies have found good similarities between pipe flows and flows in some areas within rod bundle subchannels, many have reported that these similarities highly depend on several factors such as the pitch-to-diameter ratio. In rod bundle, the pitch is the centre to centre distance between adjacent rods. Many studies have observed that, as the pitch-to-diameter ratio decreases, the turbulence field within the subchannels, especially in the narrow gaps, deviates significantly from pipe data. For the most part, this was attributed to large-scale coherent vortices, which caused high transport of momentum across the gaps. These vortices are believed to be coupled and caused quasi-periodic behaviour of the fluctuating velocities in the gap regions. Trupp and Azad [1975] conducted hot wire velocity measurements over a wide range of Reynolds number (12,000-84,000) in a triangular array rod bundle for three pitch-to-diameter ratios P/D = 1.20, 1.35 and 1.50. They observed that the friction factor highly depended on P/D and was higher for all three test sections than for flow through smooth tubes. The mean axial velocity distribution was also found to be affected by the pitch-to-diameter ratio while the radial Reynolds shear stresses were similar in distribution to pipe flow but lied below the radial shear stresses distribution corresponding to the pipe flow.

The effect of rod spacing on Reynolds shear stresses was also investigated by Hooper [1980] in a square array of rod bundles. He reported that for his largest rod spacing (P/D = 1.194), the radial Reynolds shear stresses had a linear distribution similar to observations made by Trupp and Azad [1975] in all the subchannels around the rod. For a tighter rod packing (P/D = 1.107), Hooper [1980] found that the Reynolds stresses $-\rho\overline{uv}$ were no longer linear.

Ouma and Tavoularis [1991] investigated the structure of turbulent flow in a triangular subchannel of an outer 5-rod segment of a 37-rod CANDU rod bundle model. The experiment was conducted for the design geometry and for cases with one rod displaced toward or away from the wall. They measured the Reynolds shear stress $-\rho\overline{uv}$ and found it to be positive at the wall and decreased to zero near the centerline of the subchannel. This is consistent with the Trupp and Azad [1975] and Hooper [1980] findings. They also conducted a detailed investigation of turbulent length scales

and reported that integral length scale, the Taylor microscale and the Kolmogorov microscale increased from the rod surface toward the centre of the subchannel for both cases. The magnitude of the integral length scales and Taylor microscales at design condition were higher than those for a rod-wall contact condition.

In an experimental study on a triangle array rod bundle at two different pitch-to-diameter ratios ($P/D = 1.12$ and $P/D = 1.06$), Krauss and Meyer [1998] observed that the turbulent intensities were comparable to those of pipe data only away from the rod-rod gap and decreased from the surface of the rod toward the centre of the channel. The deviation was more pronounced for the pitch-to-diameter ratio of $P/D = 1.06$. Although the reduction of the gap size at $P/D = 1.06$ caused a reduction of the mean axial velocity, the axial turbulent intensities were very high especially close to the rod-rod gap even further away from the rod surface.

Similar observations were reported by Guellouz and Tavoularis [2000] who used hotwire anemometry to measure turbulence statistics in a square duct with a displaceable cylindrical rod to simulate the effect narrow gaps on the flow structure. They found that the mean axial velocity contours bulged toward the gap as a result of the action of coherent vortices, which enhanced the turbulent intensity as the gap got narrower.

2.1.3 Development of large-scale coherent vortices

Previous authors have observed the formation of large-scale vortices in rod bundles and investigated the mechanisms triggering them and the effects they have on the overall flow field. Guellouz and Tavoularis [2000] visualized coherent structure formation in a rectangular channel containing a single cylindrical by injecting smoke at the centre of the rod-wall gap and illuminated it using a laser sheet placed on the equidistant plane. Their visualization showed low frequency periodic structures across the gap. They also attempted to construct a physical model of the coherent structures based on their hot-wire data and showed that the frequency of pulsation increased with the flow velocity.

In a laminar flow experiment in a rectangular channel with a cylindrical core,

Gosset and Tavoularis [2006] found through extensive observations that flow instability started to occur at a critical Reynolds number and eventually developed into large-scale quasi-perodic laminar vortices.

Baratto et al. [2006] carried out an experimental study on an outer 5-rod segment of a 37-rod CANDU fuel bundle. In their experiment, they showed that the pulsations in a rod-wall gap and an adjacent rod-rod gap were synchronized. Therefore, they concluded that coherent structures in rod bundles were highly correlated and interfere with each other.

In a recent experimental study, Choueiri and Tavoularis [2014] used LDV and PIV to study the flow structure along an eccentric annular channel. They reported formation of coherent vortices, which tended to grow rapidly and caused strong quasi-periodic velocity fluctuation, especially near the narrow gap region. In a following article, Choueiri and Tavoularis [2015] found that the properties of the coherent vortices depended on the inner-to-outer diameter ratio, eccentricity, Reynolds number and inlet conditions.

A comprehensive review of large-scale quasi-periodic vortices was presented by Meyer [2010], who summarised past experimental studies that investigated these phenomena. He noted that in most rod bundles the vortices are unstable and their periodicity start to deteriorate at pitch-to-diameter ratio higher than 1.2. In general, these large-scale vortices emphasize the anisotropy of the turbulent transport processes in the subchannels of the rod bundle, especially in the narrow gap. This creates several challenges because the strong anisotropy caused by these vortices cannot be easily reproduced in numerical models without suitable empirical data.

2.2 Computational studies

Early computational studies of rod bundle flows were notoriously inaccurate. Nevertheless, in recent years, several research groups have published realistic numerical simulations of turbulent flow and heat transfer in rod bundles.

Chang and Tavoularis [2005] solved the unsteady Reynolds averaged Navier-Stokes (URANS) equations to numerically simulate the formation of coherent vortices and

predict their effect on the flow structure in a rectangular channel containing a cylindrical rod. Their simulation predicted that most of the total turbulent kinetic energy in the gap region was associated to the effect of coherent vortices. In a later study on a similar geometry, Chang and Tavoularis [2012] did a comparative analysis between Reynolds averaged Navier-Stokes (RANS) solutions, URANS solutions and large eddies simulation (LES) and concluded that, although LES yielded the most accurate results, URANS results were also fairly accurate. They also confirmed that URANS could be used to simulate turbulent flows in more complex geometries such as rod bundles.

Chang and Tavoularis [2007] used standard CFD procedures to solve the URANS equations coupled with the Reynolds stress model to determine the turbulent characteristics of a single-phase, isothermal flow in a 60° sector of a CANDU 37-rod bundle. They claimed their approach worked by separating the coherent fluctuations from the non-coherent fluctuations and resolved the first numerically while the latter was modelled. They found their technique to yield results, which were in good agreement with experimental work.

Home et al. [2009] used URANS to simulate flow pulsations across a narrow channel connecting two square channels. Their simulation showed periodic behaviour, which they attributed to a large-scale network of vortices. Their simulation results showed good agreement with previous experimental studies conducted by Meyer and Rehme [1994].

A numerical study of flow structure in a rod bundle was conducted by Ikeno and Kajishima [2010] using large-scale eddy simulation (LES). Their study agreed with previous experimental and numerical studies, which investigated formation of gap vortex networks and their implications in the transfer of energy and momentum throughout the interconnected subchannels via the narrow regions of the rod bundles.

Chapter 3

Background and Definitions

3.1 Hydraulic Diameter

The hydraulic diameter provides a means by which flows in non-circular channels could be treated as flows in circular pipes. It is defined as

$$D_h = \frac{4A}{P}, \tag{3.1}$$

where A is the cross-sectional area and P is the wetted perimeter of the cross-section.

For a full 37-element CANDU rod bundle (see Figure 3.1), the hydraulic diameter is given by

$$D_{h_{CANDU}} = \frac{\pi(4R_T^2 - 37D^2)}{2\pi R_T + 37\pi D}, \tag{3.2}$$

where R_T is the radius of the pressure tube and D is the diameter of the rods. As shown in figure 3.1, the experimental model consisted of six full rods, one-sixth segment of a rod, one-sixth segment of the pressure tube and two plane side walls, which are absent from the full rod bundle. Its cross sectional area and wetted perimeter were calculated as

$$A = \frac{\pi(4R_T^2 - 37D^2)}{24} \tag{3.3}$$

and

$$P = \frac{(2\pi + 12)R_T + (37\pi - 6)D}{6} \tag{3.4}$$

and so its hydraulic diameter was calculated as

$$D_{h_{model}} = \frac{\pi(4R_T^2 - 37D^2)}{(2\pi + 12)R_T + (37\pi - 6)D}. \tag{3.5}$$

The hydraulic diameters of the experimental model, the large-scale model of a full CANDU rod bundle as well as the actual CANDU rod bundle are given in Table 3.1 and are nominally 73.6 mm, 95.2 mm and 7.4 mm, respectively. The difference in hydraulic diameter between the experimental model and the large scale CANDU model

arises from additional wetted perimeter due to the side walls in the experimental model, which are not present in a full CANDU rod bundle configuration.

	CANDU rod bundle	Large-scale 37 rod model	Experimental model
Scale	1:1	12.9:1	12.9:1
Number of rods	37	37	6+1/6
D (mm)	13.08	168.73	168.73
R_T (mm)	51.69	666.80	666.80
Configuration	full bundle	full bundle	1/6 of a full bundle with side walls
D_h (mm)	7.4	95.2	73.6

Table 3.1: Specifications of an actual, a large-scale and the experimental model of a CANDU rod bundle.

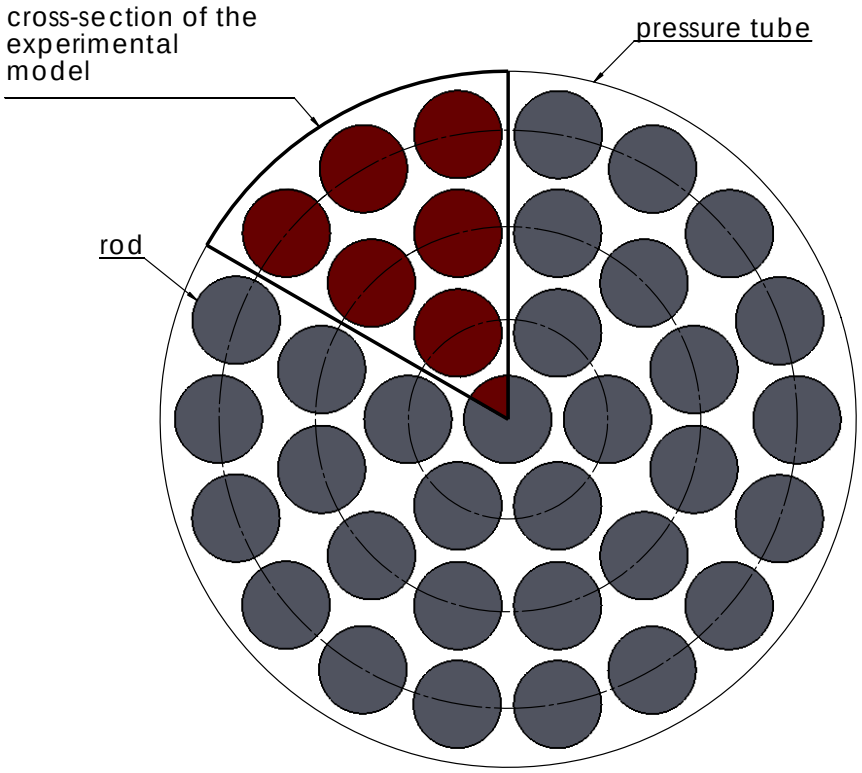

Figure 3.1: Cross-section of a 37-rod CANDU reactor bundle.

3.2 Bulk velocity and bulk Reynolds number

The bulk velocity U_b in this experiment was defined as the ratio of the volumetric flow rate and the cross-sectional area of the test section, namely as

$$U_b = \frac{1}{A}\int_A \overline{U} dA. \tag{3.6}$$

The bulk velocity was determined by the following procedure. A Pitot tube was first used to measure the local flow velocity U_c. The flow rate was then calculated as

$$Q = cU_cA_c \ , \tag{3.7}$$

where c is a correction factor, to be discussed in section 4.6 and A_c is the the cross-sectional area of the intake contraction throat. Then the bulk velocity through the test section was estimated as

$$U_b = \frac{Q}{A_t} = \frac{cU_cA_c}{A_t} \ , \tag{3.8}$$

where the A_t is the test section cross-sectional area. The bulk Reynolds number was defined as

$$Re_b = \frac{\rho U_b D_h}{\mu} \ , \tag{3.9}$$

where ρ and μ are the air density and viscosity, respectively, at room temperature.

3.3 Coordinate system

An illustration of the coordinate system used in this study is shown in figure 3.2. Axial, radial and azimuthal components of the turbulent statistics were oriented along axes x, r and ϕ, respectively. The axis x was parallel to the axis of the central rod and its origin started from the inlet of the experimental rod bundle. The axis r was oriented along the radial direction of the central rod and the axis ϕ was normal to the plane containing the axes x and r.

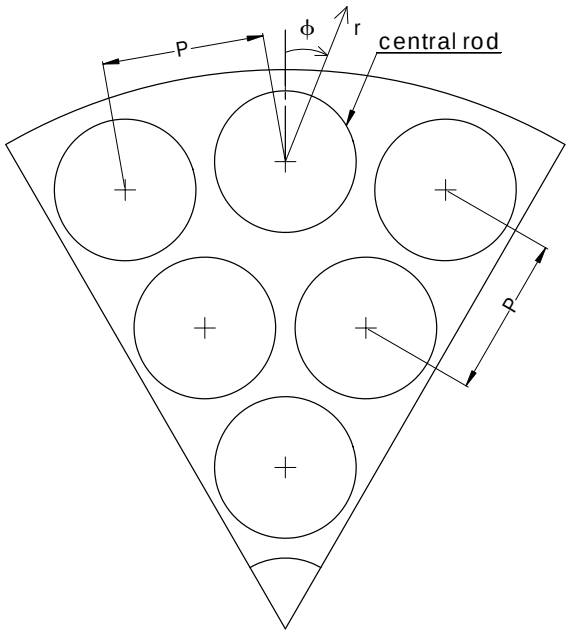

Figure 3.2: Illustration of the rod bundle's coordinate system.

3.4 Turbulent kinetic energy

The turbulent kinetic energy was defined as $k = \frac{1}{2}\left(\overline{u^2} + \overline{u_r^2} + \overline{u_\phi^2}\right)$, where $\overline{u^2}$, $\overline{u_r^2}$ and $\overline{u_\phi^2}$ are the variances of the instantaneous axial, radial and azimuthal velocity components, respectively. In this study, the axial velocity was taken as the velocity parallel to the axis of the rods. The radial component of the velocity was always parallel to radius of the central rod and the azimuthal velocity component was in a plane normal to the plane containing the axial and radial velocities. The turbulent kinetic energy is associated with turbulent eddies in the turbulent flow and dominates the transport of heat, momentum and mass.

In general, as the flow becomes more turbulent, the turbulent intensity increases especially near the wall regions. In nuclear reactors for instance, this correlates to a higher local heat transfer coefficient.

3.5 Turbulent length scales

Turbulent motions have wide ranges of time and length scales. Turbulent length scale refers to the typical size of structures in the flow. Three main turbulent length

scales are commonly used: the integral length scale, the Taylor microscale and the Kolmogorov microscale.

The integral length scale is a measure of the size of the most energetic eddies in the turbulent flow. The streamwise integral time scale was first calculated by integrating the corresponding autocorrelation coefficient to its first zero crossing. Then, the use of Taylor's frozen flow approximation was applied to determine the streamwise integral length scale as

$$L_u = \overline{U} \int_0^{\tau_0} \frac{\overline{u(t+\tau)u(\tau)}}{\overline{u^2}} \, d\tau \ , \tag{3.10}$$

where $\overline{U}$ is the mean axial velocity. Similar expressions were used to determine the streamwise integral length scales L_r and L_ϕ of the radial and azimuthal velocity fluctuation components.

The streamwise Taylor microscale was measured as

$$\lambda = \overline{U} \sqrt{\frac{\overline{u^2}}{\overline{(\partial u/\partial t)^2}}}. \tag{3.11}$$

The importance of the streamwise Taylor microscale in nuclear thermalhydraulic is indirect because this property does not represent the scale of a physical mechanism. Nevertheless, in numerical studies, with the exception of direct numerical solutions, the streamwise Taylor microscale may serve as a guideline for the mesh requirements. Chang and Tavoularis [2007] found that to perform a large eddy simulation for this experiment, one would require at least 3×10^7 grid elements to resolve motions of scale equal to λ.

The relative strength of turbulence was indicated by the turbulence Reynolds number, which was determined as

$$R_\lambda = \frac{u'\lambda}{\nu}. \tag{3.12}$$

The rate of kinetic energy dissipation per unit mass was calculated with the use of the locally isotropic expression

$$\epsilon = 15\nu \frac{\overline{u^2}}{\lambda^2}. \tag{3.13}$$

The Kolmogorov microscale is comparable to the size of the smallest eddies in turbulent flows. It is the scale at which the turbulent kinetic energy is fully dissipated into heat. At this scale, the turbulence structure is assumed to be isotropic. The Kolmogorov microscale was determined as

$$\eta = \left(\frac{\nu^3}{\epsilon}\right)^{(1/4)}. \tag{3.14}$$

3.6 Reynolds stress tensor

The components of the Reynolds stress tensor represent the corresponding average momentum fluxes caused by the fluctuating velocity field. This tensor is symmetric and consists of nine components, six of which are independent. These are the normal stresses $-\rho\overline{u^2}$, $-\rho\overline{u_r^2}$, $-\rho\overline{u_\phi^2}$ and the shear stresses $-\rho\overline{uu_r}$, $-\rho\overline{uu_\phi}$, $-\rho\overline{u_r u_\phi}$. The shear stresses play a key role in the transfer of energy by turbulent motions. Measurement with cross-wires typically allows direct measurement of all stresses except $-\rho\overline{u_r u_\phi}$.

3.7 Coherent structures

Coherent structures can be defined as interconnected large-scale structures with a phase-correlated vorticity (Hussain [1983]) or as recurring patterns in turbulent flow which cause transport of momentum across a certain distance (El Tahry [1990]). Lesieur [2008] states that coherent structures are regions within the flow, where at a given time, the turbulent quantities such as velocity, vorticity, pressure density or temperature tend to remain unaffected by the random motion of the flow.

In tightly-packed nuclear rod bundles, such as the CANDU 37-rod bundle, coherent structures cause strong momentum and mass transfer across the narrow gaps. This results in an increase of the local heat transfer coefficient and improves the thermalhydraulic performance of the nuclear reactor.

Chapter 4

Experimental facility, instrumentation and measurement procedures

4.1 Rod bundle facility

All measurements in this study were conducted in a scaled up (12.9:1) model of a 60° section of a CANDU 37-rod bundle at the University of Ottawa.

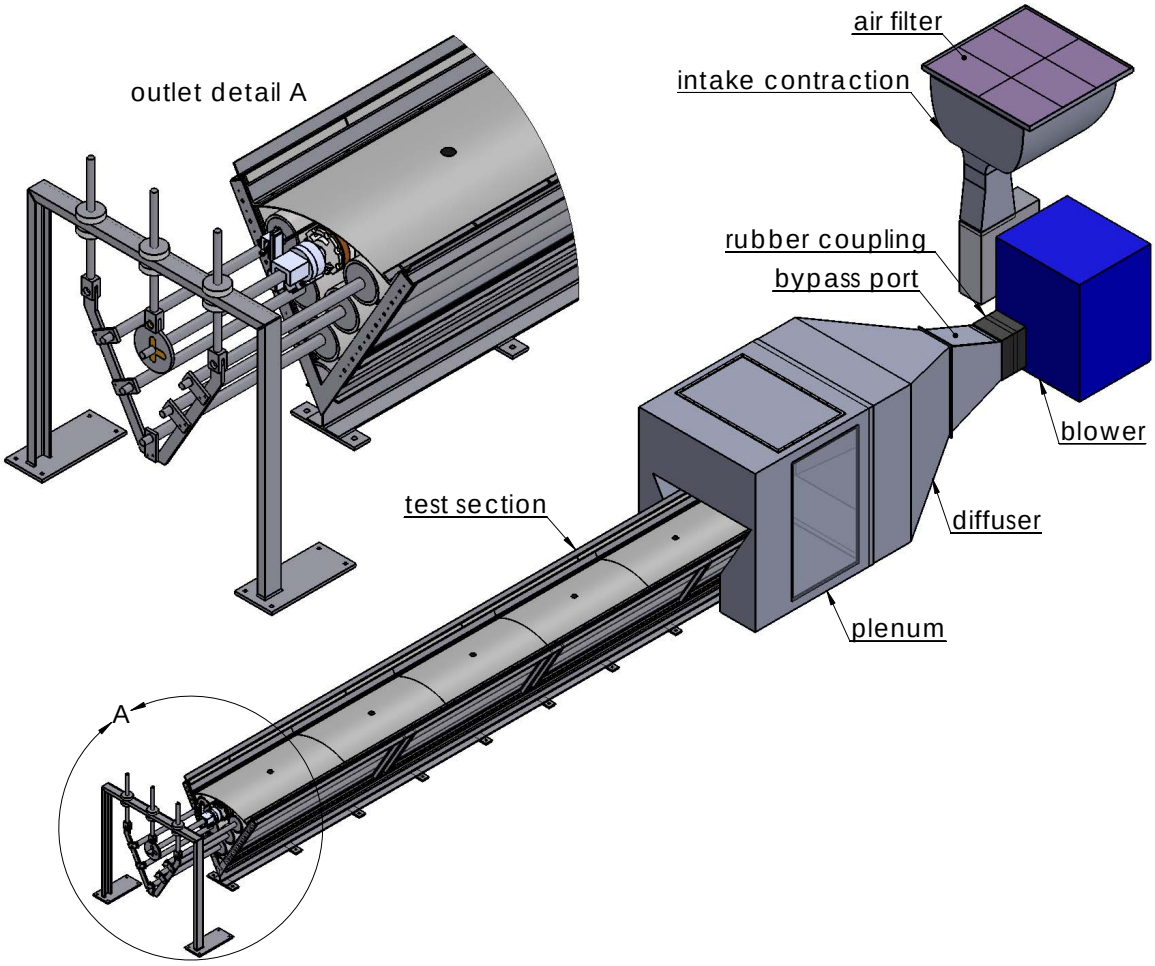

Figure 4.1: Rod-bundle facility at the University of Ottawa.

A schematic diagram of the experimental rod bundle facility is shown in figure 4.1. The facility's Reynolds number ranged from 43,000 to 140,000, which corresponds to a range from 55,600 to 181,000 for a similar scale CANDU rod bundle. This difference arose from the additional wetted perimeter of the present facility due to the side walls, which are not present in the CANDU rod bundle. The rod bundle facility used air as the medium. The main components of the facility are described in the following subsections.

Intake contraction

The intake contraction was constructed from 3 mm thick 6061 aluminium metal sheets and was 1770 mm in length. The contraction design was based on a procedure described by Downie et al. [1984]. It had a 1110 mm $\times$ 1110 mm inlet cross section and a 251 mm $\times$ 302 mm throat cross-section, which provided a contraction ratio of approximatively 16.25.

Flow was accelerated through the intake contraction and discharged toward the diffuser and plenum by a centrifugal blower (Canadian Blower and Forge, model 71G-2526T). The fan was powered by a 14.9 kW (20 hp), 21 A, three-phase AC motor. The AC motor was controlled via a variable frequency drive (MGI Technology, model M7600-00320).

To improve flow quality and reduce dust particles, which can damage the measurement probes, air filters were placed at the inlet of the intake contraction. The filters were supported by wire frames stretched across the inlet of the contraction. The filters consisted of polypropylene sheets (Filtration Group, model MERV 11), which reduced 85 percent of particles larger than 1 μm.

Diffuser and plenum

Further flow quality management was performed in the diffuser and plenum, which are shown in figure 4.2.

The diffuser was constructed with 3 mm thick aluminium metal sheets and consisted of two sections. The upstream section had a removable cover that served as the port for the bypass system. It had inlet and outlet dimensions of 406 mm high

× 343 mm wide and 910 mm high × 343 mm wide, respectively, and a length of 762 mm. It was connected to the blower discharge using a rubber coupling to reduce vibrations from the blower. The downstream section had five perforated plates (type A in Table 4.1) that broke down large-scale motions at the exit and caused pressure drop, which counteracted the adverse pressure gradient in the diffuser and prevented flow separation form the walls. It had a 910 mm × 343 mm inlet cross section and a 1645 mm × 1391 mm outlet cross section over a length of 1016 mm.

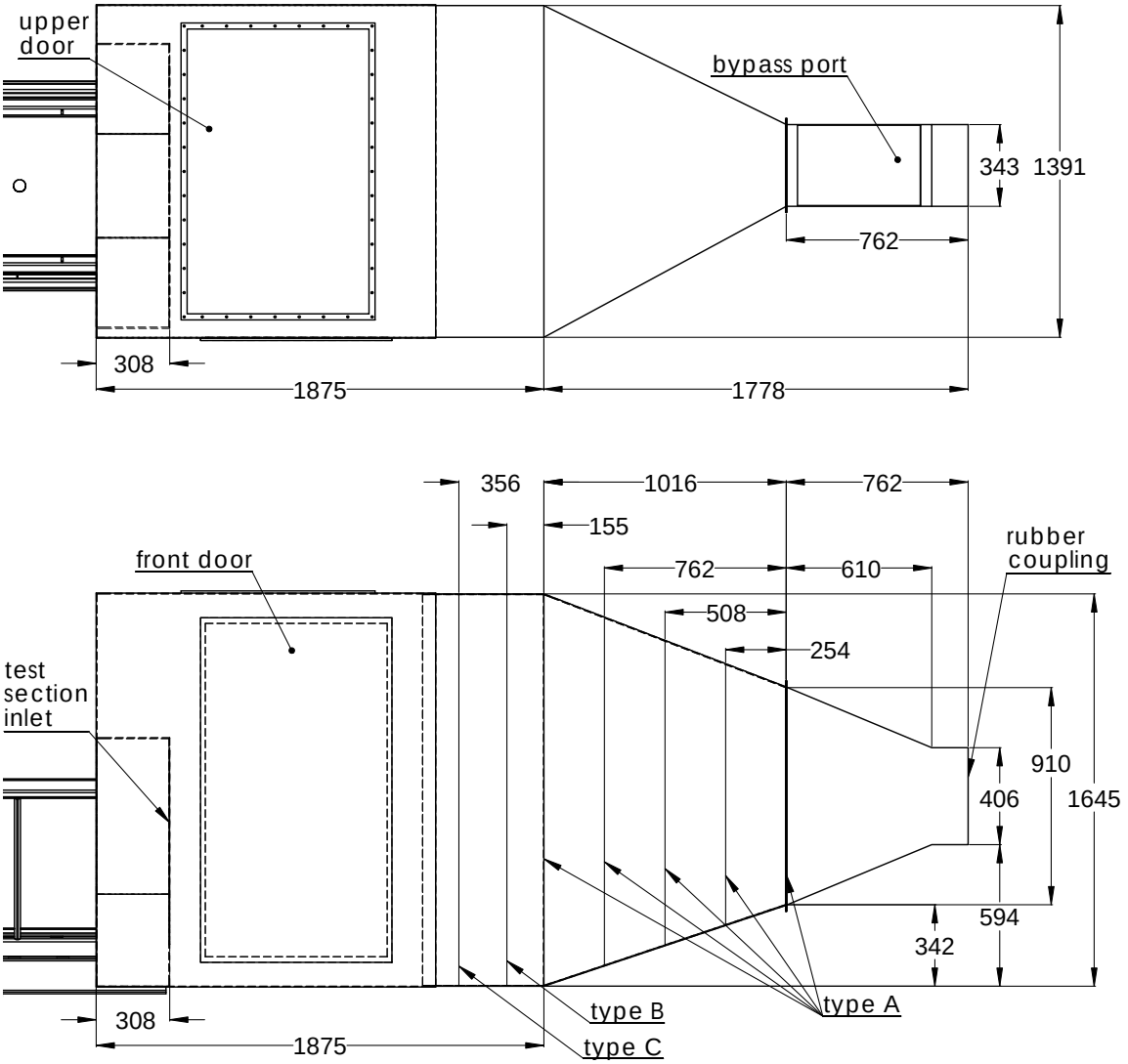

Figure 4.2: Schematic diagram of the diffuser and the plenum; front and top views; all dimensions are in mm.

The plenum was a 1875 mm long × 1645 mm high × 1391 mm wide chamber

with an upper and a front access door. It was fitted with a honeycomb (type B in Table 4.1), to straighten and improve the uniformity of the flow. An additional perforated plate (type C in Table 4.1) was placed after the honeycomb to further reduce the turbulence level at the test section inlet. Specific locations of the plates and honeycomb are shown in figure 4.2. The plenum was directly connected to the inlet of the test section.

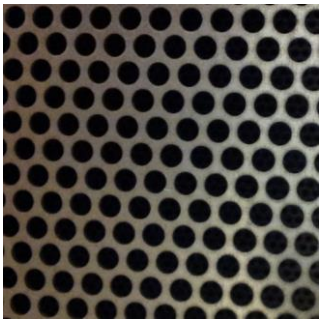 Type A	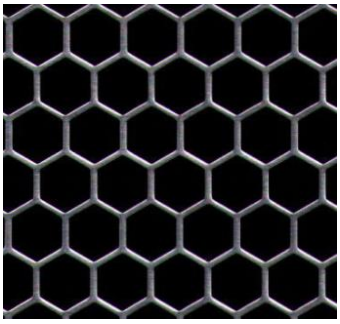 Type B	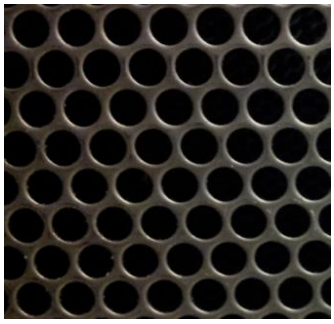 Type C
Description: 49% solidity, 1.27 mm thick perforated aluminium plate. Perforations are staggered round holes with 4.76 mm diameter and 7.94 mm distance between centres.	Description: Honeycomb, made of aluminium, 38.1 mm thick and with 6.35 mm cell size.	Description: 42% solidity, 6.35 mm thick perforated aluminium plate. Perforations are staggered round holes with 6.35 mm diameter and 7.94 mm distance between centres.

Table 4.1: Perforated plate configurations.

Test section

The following information has in part been taken from the technical report by Rind and Tavoularis [2012]. A diagram of the test section, viewed from the plenum interior, is presented in figure 4.3. The test section was a geometrically scaled up (12.9:1) model of a 60° section of the CANDU 37-rod bundle. It consisted of six rods and a one-sixth segment of a rod, which were models of CANDU fuel elements. Each rod was a piece of a Schedule 40 pipe, with a nominal outer diameter of 168.3 mm and a nominal length of 6100 mm. Consequently, the length-to-diameter ratio of the present rods was 36.2. The nominal diameter and length for a typical CANDU rod are 13.08 mm and 500 mm, respectively. Hence, the length-to-diameter ratio of a CANDU rod is

equal to 38.2, which is slightly larger than the one in the present facility. The central rod, as identified in figure 4.3, was made of Polyvinyl Chloride (PCV), whereas the other five rods were made of aluminium. PCV piping was used in preparation for future studies in which this rod will be covered by an electrically heated metallic foil to permit heat transfer measurements. An aluminium Schedule 10 pipe with an outer diameter of 101.6 mm was inserted inside the central rod to reduce sagging at its middle. Spacers were placed at various locations along the Schedule 10 pipe to maintain it in the coaxial position with the central rod. With this assembly, the sagging was reduced down to 0.8 mm from 27.9 mm. The sagging in the middle of the other five rods was estimated at about 0.2 mm when supported at their ends. In most cases, the sagging changed the size of the gap at the middle of each rods by less than 3%. The uncertainty on the diameters of rods used in this facility was 0.42 mm.

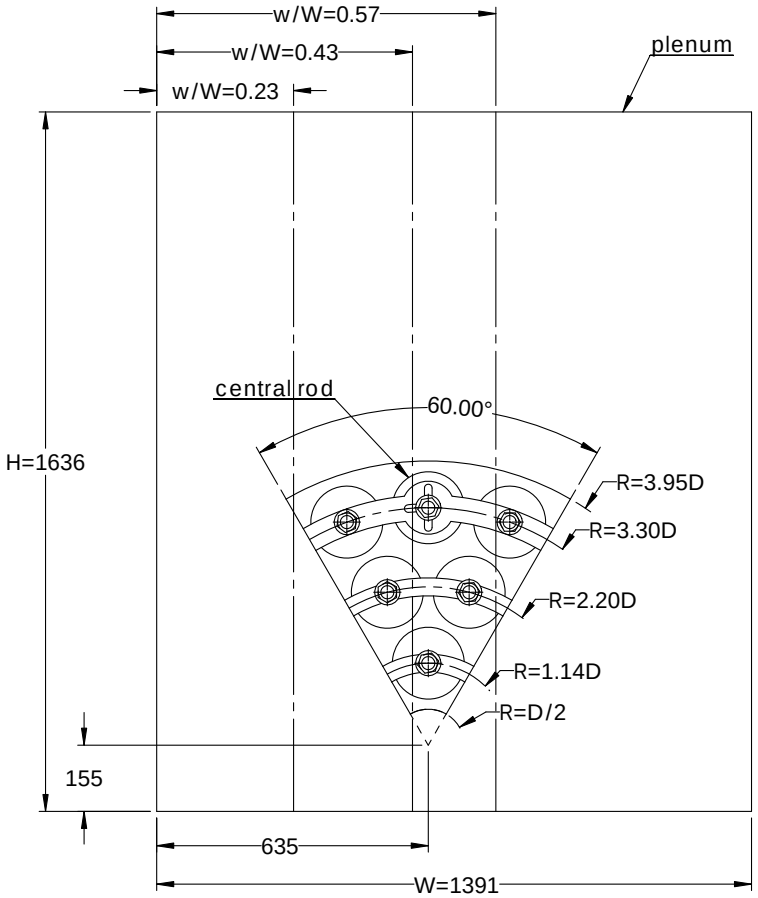

Figure 4.3: Test section inlet with endplate viewed from the plenum interior; dimensions are in mm and the rod diameter is $D = 168.3$ mm.

A model of a CANDU endplate supported the rods at the upstream end. The endplate was 13.6 mm thick and was made of aluminium. At the downstream end, the rods were supported coaxially on 38.1 mm diameter rods, which were fastened to a suspended 13.6 mm thick aluminium frame located at 700 mm from the outlet of the test section as illustrated in figure 4.1.

The top cover of the test section consisted of five sections of 1 mm thick stainless steel sheets. The sheets were curved at identical radii and carefully placed along the test section to model the CANDU pressure tube. The top cover had five ports, which allowed vertical insertion and traversing of probes across the narrow gap between the central rod and the inner wall of the top cover. The distances of the port centres from the inlet are listed in table 4.2.

Port number	1	2	3	4	5
Distance from the inlet (mm)	406	2032	3251	4470	5690

Table 4.2: Positions of port centres on the top cover of the test section.

Each side wall of the test section was made of 10 mm thick glass with matching Plexiglas sections located at four locations along the test section. The walls were adjusted and kept fixed with the use of horizontal clamps, so that the facility dimensions were kept as closely as possible to the design values and were insensitive to deformations due to pressure.

The gap size between an outer rod and the inner wall of the top cover was approximately $0.15D$. The gaps between adjacent rods positioned at equal distances from the bundle axis were approximately $0.14D$. With the exception of the narrow gaps around the central rod, all other narrow gaps were maintained fixed with the use of short spacers inserted at the downstream end of the test. In addition, spacers were inserted half way along the test section in the gaps between the rods and the side walls.

Traversing system

A traverse system was mounted on the support of the central rod at the exit of the test section as shown in figure 4.4. It consisted of a single axis linear slide (Velmex Inc,

model MA1505-25K1) and a rotary table (Velmex Inc, model B4836TS-ZRS). They were controlled by two high performance, programmable, 2 phase, unipolar stepper motor encoders (Velmex Inc, model VXM-1).

The linear slide allowed for radial indexing of the hot-wire probe. Its 1 mm pitch lead screw was driven by a stepper motor, which had a 1.8°/step resolution. Hence, the linear slide, when operated in half-step mode, had a positioning resolution of 0.0025 mm/step and a 0.18 mm positioning uncertainty.

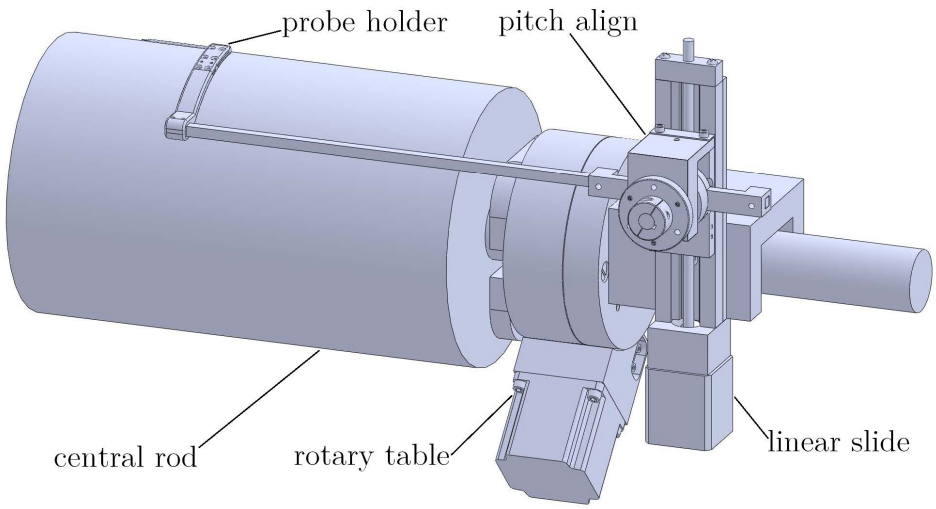

Figure 4.4: Rod bundle traversing system

The rotary table was used to position the probe at various angular locations around the central rod and had a resolution of 0.025°/step with a positioning uncertainty of 0.11° due to internal backlash. The pitch align mounted on the linear slide was adjusted to ensure that the axis of the probe was parallel to the incoming flow.

4.2 Calibration jet

All hot-wire velocity calibrations were undertaken on the calibration jet facility presented in figure 4.5. It featured a nozzle unit (Dantec Dynamics, model 55DH5) and two rotary tables (Velmex Inc, model B5990TS) controlled by two controllers (Velmex Inc, model VXM-1) for directional and velocity calibration of hot-wire probes. More details on the calibration facility are provided by Bailey [2006].

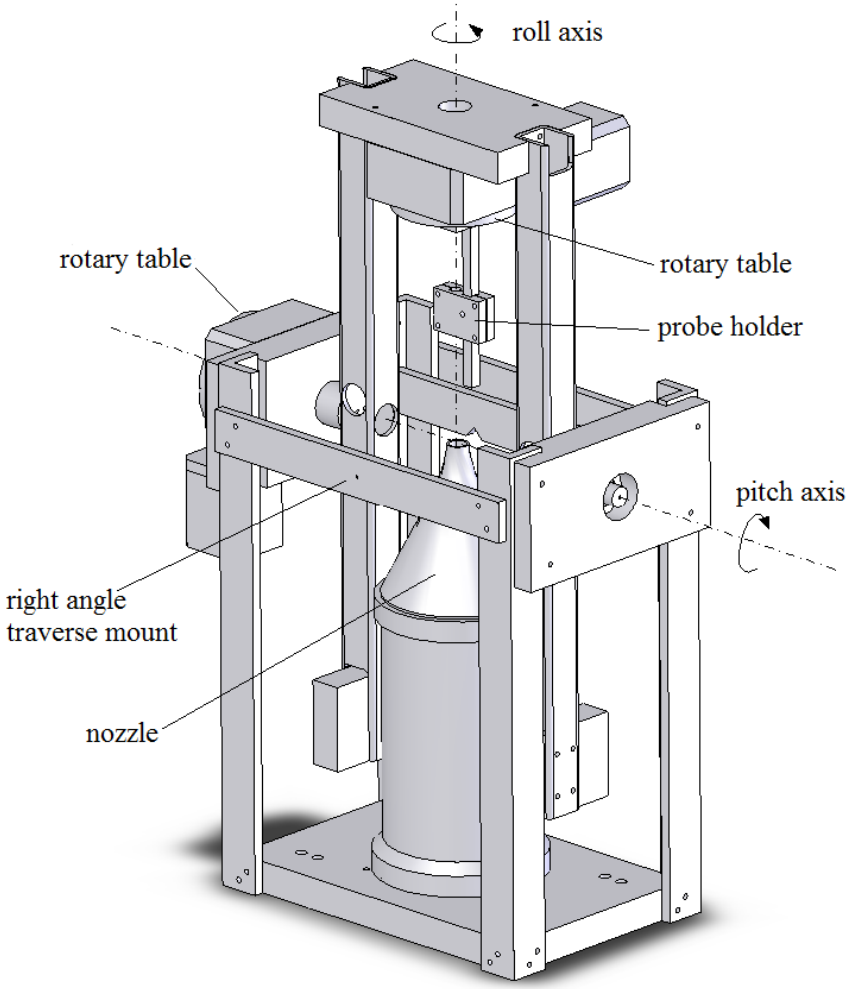

Figure 4.5: Calibration jet. Picture from Bailey's thesis.

Two additional degrees of freedom were added to the original calibration facility to facilitate right-angle probe calibration. The set up, as shown in figure 4.6, consisted of a single-axis linear slide similar to the one used in the traversing system, a high resolution stepper motor (Oriental Motor, model PKP244MU12A-L) and a 50:1 ratio worm-drive gearbox. The right-angle probe was mounted onto the worm wheel, which enabled the probe to rotate about its axis for directional and yaw calibration. The angular positioning resolution of the combined worm-drive/stepper motor was nominally 0.01°/step and its uncertainty was 0.09°. The linear slide was used to correct the deviation of the probe tip from the jet's axis caused by the rotation of the probe about its axis. The right-angle hot-wire calibration rig was mounted onto the

calibration jet as specified in figure 4.5.

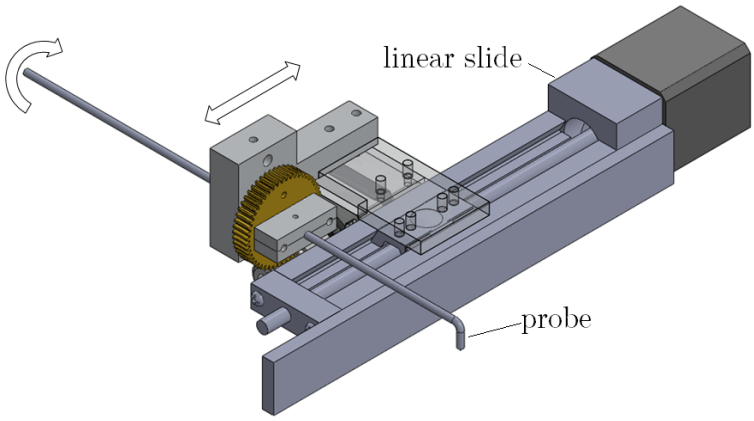

Figure 4.6: Right angle probe calibration traverse.

4.3 Instrumentation

This section describes the instrumentation used in this experiment and consists of the following subsections:

- Hot-wire anemometry
- Pitot-static tube and Preston tube
- Resistance thermometers
- Weather forecast board

4.3.1 Hot-wire anemometry

Constant temperature hot-wire anemometry was the main technique used in this experiment. Full details on this technique can be found in Bruun [1995] and Tavoularis [2005]. Two hot-wire probes used in this study were a straight cross-wire probe and a right-angle cross-wire probe.

Straight cross-wire probe

The straight cross-wire probe (Auspex Scientific, model AHWX-100) was made of Platinum-coated Tungsten wires arranged in a X-array. The sensor dimensions were

1 mm in length and 5 μm diameter. The separation distance between the sensors was 0.5 mm. The inclination angle $\overline{\alpha}$ of each sensor with respect to the probe axis was found by yaw angle calibration. The probe was mounted on the traverse system at the exit of the test section for the velocity measurements.

Right-angle cross-wire probe

The right-angle cross-wire probe was custom built by Auspex Scientific and is shown in figure 4.7.

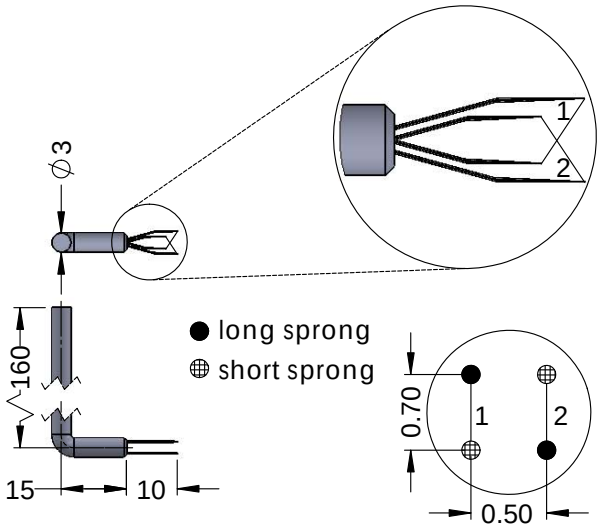

Figure 4.7: Sketch of the right angle cross-wire probe. Dimensions are in mm.

It was equipped with two 5 μm diameter, 1 mm long Platinum-coated Tungsten wires arranged in a X-array. The distance between the sensors was 0.5 mm. The probe was primarily used for one-point and two-point velocity correlation measurements.

Anemometer

Two A.A. Labs AN-1002 anemometers were used in this experiment. Each had two identical removable channels that could be operated at 1:1 and 1:10 bridge ratios, which allowed a sensor resistance range from $0.5 - 99.9\ \Omega$ and $1 - 9.99\ \Omega$, respectively. Each channel had a signal conditioning unit capable of amplifying, offsetting and filtering the hot-wire signal. The low-pass filter in the signal conditioner was a cascade

of double-pole low-pass filters with twelve selectable cut-off frequencies ranging from 1.5 KHz to 21 KHz. The frequency response of the anemometer depended on the hot-wire probe used. Each hot-wire probe was connected to the anemometer via two 5 m, 21-gauge, Alpha Wire-J coaxial RG-58 cables.

4.3.2 Pitot-static tube and Preston tube

To estimate the flow rate through the contraction, an ellipsoïdal nose Pitot-static tube (Kimo Instruments, model TPL-06-500) was mounted at the centre of the cross-section of the contraction throat. The outer body of the Pitot-static tube was 6 mm in diameter. It had one total pressure intake hole at its tip, which had a diameter of 0.6 mm and six intake static pressure holes, which were radially and evenly spaced and had a diameter of 0.6 mm. The intake static pressure holes were 48 mm from the tip of the Pitot-static tube. The flow velocity was calculated from the pressure difference measured by the tube as

$$U = \sqrt{\frac{2\Delta P}{\rho}}. \tag{4.1}$$

The Preston tube was custom built and was used to measure the average local wall shear stress around the periphery of the central rod. It consisted of three joined sections of precision steel tubing, as shown on Figure 4.8 and a support tube, which covered most of the Preston tube body.

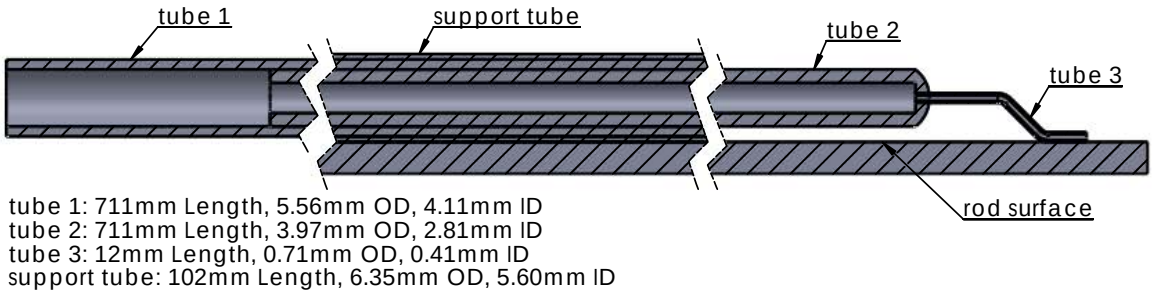

Figure 4.8: Sketch of the Preston tube. Not to scale.

The small tube (tube 3) had an inner to outer diameter ratio of 0.58 and was bent to allow contact with the surface of the rod. The overall length of the Preston tube assembly was 0.8 m.

4.3.3 Resistance thermometers

A resistance temperature detector (RTD) (Rdf Corporation, model 29348-T01) was mounted next to the hot-wire probe at the exit of the test section to measure the mean flow temperature. The RTD dimensions were 1.67 mm in diameter and 15.25 mm in length. The relationship between the resistance of the RTD and the temperature is given as

$$R = R_o \left[1 + AT + BT^2 + C(T - 100)T^3\right] \ , \tag{4.2}$$

where A,B and C are the calibration coefficients. Calibration was performed by the manufacturer in an oil bath for a temperature range from 0-100 ^{o}C at 1 ^{o}C increments and a best-fit line was fitted into the data to obtain the calibration coefficients $A = 3.9162328 \cdot 10^{-3}$, $B = -5.9977432 \cdot 10^{-7}$ and $C = -2.454044 \cdot 10^{-2}$. R and R_o are the resistance of the RTD at T and the resistance of the RTD at 0 ^{o}C in Ω, respectively. T is the fluid temperature in ^{o}C. The resistance of the RTD at 0 ^{o}C was provided by the manufacturer and was 99.983 Ω. The RTD measurement was used for hot-wire temperature compensation because of the difference between the jet temperature (usually slightly below room temperature) during hot-wire calibration and the fluid temperature in the test section during measurement. Within the first hour of operation, the temperature of the air from the blower rose to about 2 to 3 ^{o}C above the room temperature and remained fairly constant during the entire experiment. The measurement uncertainty of the RTD was 0.1 ^{o}C.

4.3.4 Weather forecast board and estimation of air density

A USB weather board (Sparkfun Electronics, model V3) and a mercury barometer were used to estimate the air density. The air density was calculated as

$$\rho = \frac{P_d}{R_d T_a} + \frac{P_v}{R_v T_a} \ , \tag{4.3}$$

where T_a is the ambient room temperature in K estimated from the board, $R_d = 286.9$ J kg^{-1} K^{-1} and $R_v = 461.5$ J kg^{-1} K^{-1}.

The partial pressure of water vapour P_v and the partial pressure of dry air P_d were calculated as

$$P_v = 610.78H \cdot 10^{(7.5T_a/(T_a+237.3))} \tag{4.4}$$

and

$$P_d = P_a - P_v \tag{4.5}$$

where P_a is the ambient room pressure read from the barometer and H is the humidity of the room estimated from the board.

4.4 Calibration techniques

This section describes the calibration techniques as well as the signal analysis methods used in this experiment.

4.4.1 Pressure transducer calibration

The pressure transducer (Furness Control, model FC0332) used in this study had a range from 0 to 2.5 KPa and an uncertainty of 0.25% of the full range.

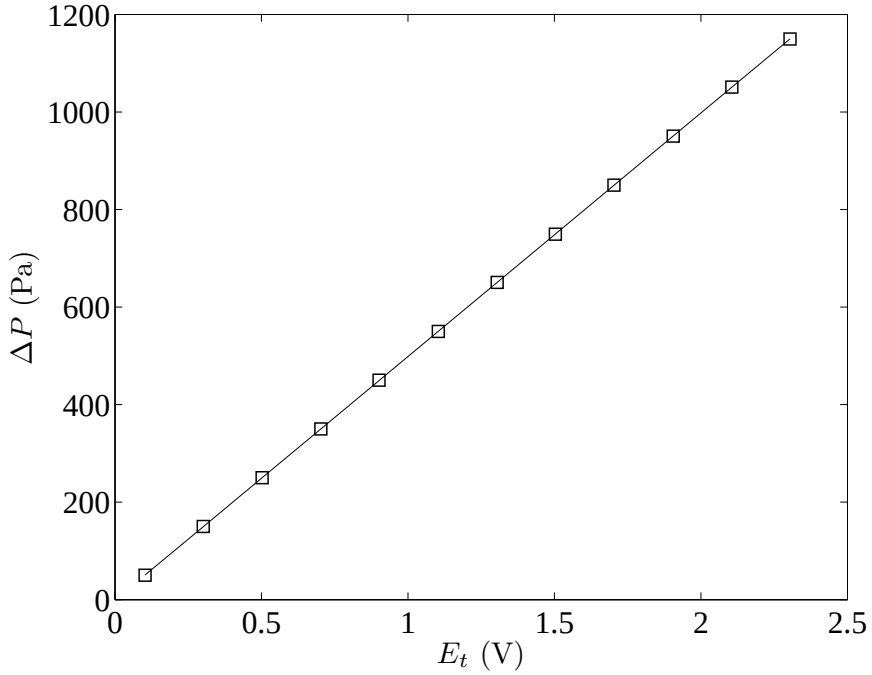

Figure 4.9: Example of pressure transducer calibration results. Solid line indicates linear curve fit.

The transducer had a four-digit LCD screen, which displayed the pressure difference ΔP being measured.

The relationship between the pressure difference and the output voltage is given as

$$\Delta P = AE_t + B. \tag{4.6}$$

where E_t is the transducer output voltage and the calibration coefficients are A and B. Calibration was performed on the calibration jet over the range of Reynolds number of interest. A line was fitted to the calibration data to determine A and B. A typical calibration curve is shown on Figure 4.9.

Wall shear stress measurement

Details on wall shear stress measurement using a Preston tube are given by Patel [1965] and Tavoularis [2005] and will be described here only briefly. The wall shear stress was determined from the parameters described in Tavoularis [2005] as

$$x^* = log\frac{\Delta P}{4\rho\nu^2/d^2} \qquad \text{and} \qquad y^* = log\frac{\tau_w}{4\rho\nu^2/d^2}. \tag{4.7}$$

This technique assumes that the inner boundary-layer scaling law is universal. The pressure difference in the parameter x^* is the difference between the total pressure measured by the Preston tube and the local static pressure. In this experiment, the static pressure was measured from a 0.5 mm diameter tap drilled on the top cover. The tap was located near the exit of the test section and its centre was on the plane perpendicular to the tip of the Preston tube. The static pressure was assumed to be uniform around the periphery of the central rod due to the proximity of the measuring point to the exit of the test section. Moreover, it is common practice in CFD analysis to assume uniform static pressure distribution around the rod [Carajilescov and Todreas, 1976].

4.4.2 Cross-wire probe calibration and signal analysis method

Directional calibration

The directional calibration was carried out on the calibration jet described in section 4.2. It consisted of finding the yaw coefficients $\overline{\alpha}$ and k^2. The yaw coefficients

resulting from the directional calibration were used in the final velocity calibration. The directional calibration was performed in the following sequence.

- Step 1: sensor inclination

In this step, the cross-wire probe was placed at the centre of the jet, which was operated at constant velocity and temperature. The probe was rotated about its axis until its sensors were parallel to the plane containing the roll axis and which is normal to the pitch axis. Using the rotary table along the pitch axis, the probe was first tilted in one direction from 35° to 55° at 0.2° increments to find the sensor's inclination angle $\overline{\alpha}$ with respect to the probe axis. $\overline{\alpha}$ was found at the pitch angle θ_{max} at which the voltage reading from the anemometer was maximum. The inclination angle was then calculated as

$$\overline{\alpha} = 90 - \theta_{max}. \tag{4.8}$$

The probe was subsequently tilted in the other direction to determine the inclination angle of the other sensor. A typical plot of the anemometer output voltage (E_{out}) versus pitch angle at constant velocity is shown in Figure 4.10.

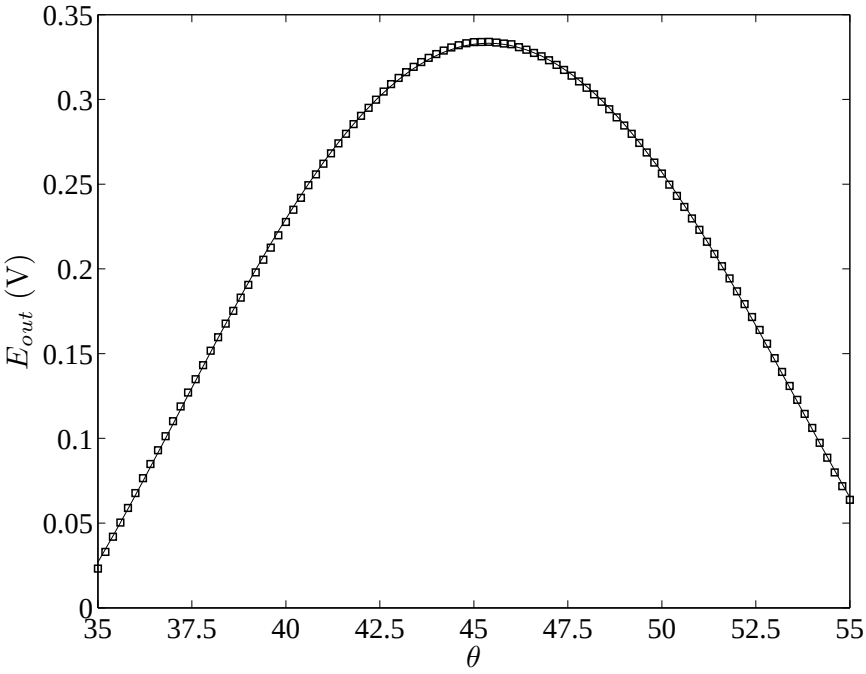

Figure 4.10: Example of sensor inclination angle result. Solid line indicates 5^{th} order polynomial curve fit.

- Step 2: preliminary velocity calibration

This step consisted of finding the calibration coefficients A_0, B_0, and n_0 for each sensor in the modified King's law

$$\frac{E^2}{T_w - T_f} = A_0 + B_0 U_{jet}^{n_0}. \tag{4.9}$$

The sensor temperature T_w was estimated as $T_w = (OHR - 1)/\alpha_r + T_r$, where $\alpha_r = 0.0048\ ^\circ\mathrm{C}^{-1}$ is the sensor's coefficient of resistivity at a reference temperature $T_r = 21^\circ C$. An overheat ratio (OHR) of 1.5 was used in this study. The probe axis was aligned with the jet axis and the signal E of each sensor, the jet velocity U_{jet} and the flow temperature T_f were recorded for 20 s at each jet velocity. The flow temperature was measured using an RTD and the calibration was performed for the full range of Reynolds number of interest. Least-squares curve fitting was performed to find the coefficients A_0, B_0, and n_0.

- step 3: yaw calibration

Yaw calibration consisted of measuring the tangential cooling coefficient k^2 of each sensor at a constant jet velocity. The probe was inclined at various pitch angles θ ranging from -15° to 15° at 3° increments. At each angular position, the sensors signal E, the jet velocity U_{jet} and the flow temperature T_f were recorded for 20 s. The parameters X and Y at each position were calculated as

$$X = E_\theta^2 sin^2\overline{\alpha} - sin^2\alpha \qquad \text{and} \qquad Y = E_\theta^2 - 1 \tag{4.10}$$

and linear curve fitting was performed to find k^2 from the expression

$$Y = (1 - k^2)X. \tag{4.11}$$

The parameter E_θ was estimated as

$$E_\theta = \frac{\left(\frac{\left(E^2/\left(T_w - T_f\right)\right) - A_0}{B_0}\right)^{1/n_0}}{U_{jet}} \tag{4.12}$$

and the yaw angle α in expression of the X parameter expression was calculated as

$$\alpha = \theta + \overline{\alpha}. \tag{4.13}$$

A typical yaw calibration curve is shown in figure 4.11. The tangential cooling coefficient k^2 of the cross-wire used in this experiment was approximately 0.025 for both sensors.

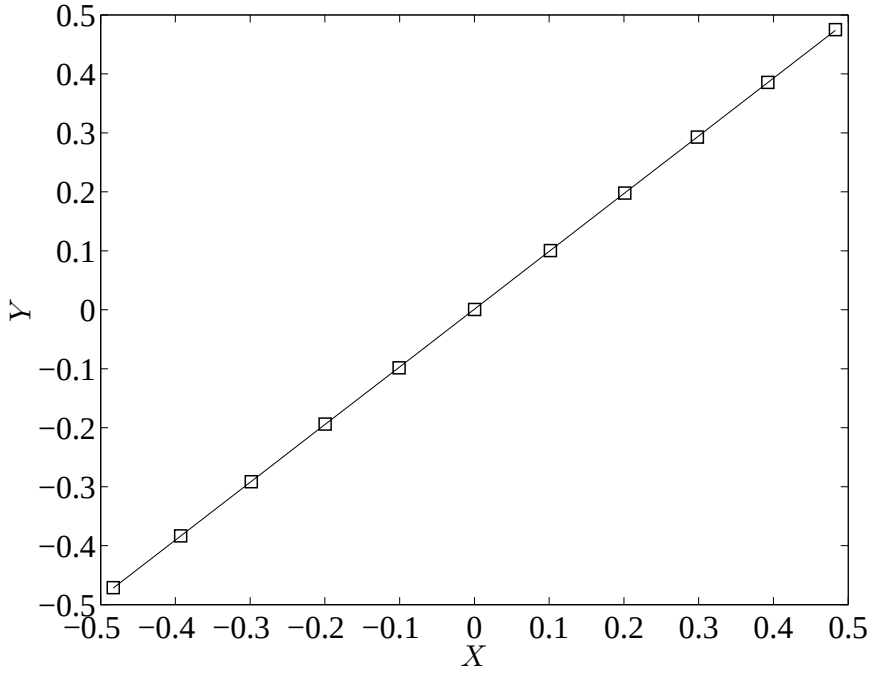

Figure 4.11: Example of yaw calibration result. Solid line indicates linear curve fit.

Velocity calibration

A similar procedure as the one described in step 2 was used to determine the calibration coefficients A, B and n for each sensor in

$$\frac{E^2}{T_w - T_f} = A + B\left(\left(cos^2\overline{\alpha} + k^2 sin^2\overline{\alpha}\right)^{1/2} U_{jet}\right)^n \tag{4.14}$$

It could be noted that the modified King's law was slightly adjusted to account for cooling due to tangential velocity as discussed in Bruun [1995]. An example of hot-wire calibration curves is shown in figure 4.12

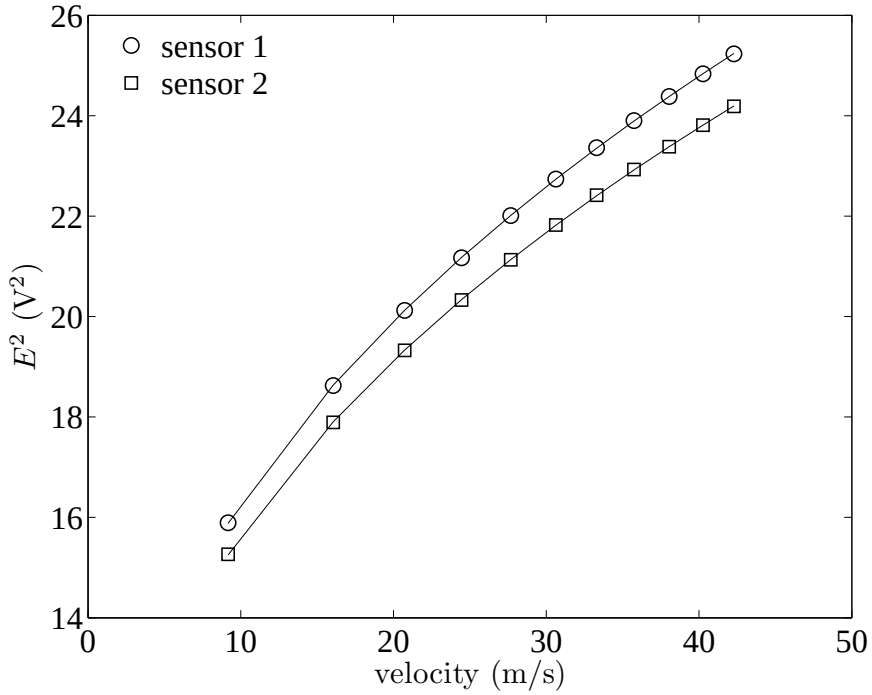

Figure 4.12: Example of velocity calibration results. Solid lines indicate King's Law curve fits.

Signal analysis method

The hot-wire signal conditioning was carried out in terms of the effective cooling velocities V_{e1} and V_{e2} for the two sensors. The general expression of the effective cooling velocity was

$$V_{ei} = \left(\frac{\left(E_i^2 / \left(T_w - T_f\right)\right) - A_i}{B_i} \right)^{1/n_i} , \tag{4.15}$$

where $i = 1$ and $i = 2$ correspond to sensor 1 and sensor 2, respectively. The streamwise and transverse velocities were expressed as

$$U = \frac{\left[V_{e1}/f_1\left(\overline{\alpha}_1\right)\right] g_2\left(\overline{\alpha}_2\right) + \left[V_{e2}/f_2\left(\overline{\alpha}_2\right)\right] g_1\left(\overline{\alpha}_1\right)}{g_1\left(\overline{\alpha}_1\right) + g_2\left(\overline{\alpha}_2\right)} \tag{4.16}$$

$$V = \frac{\left[V_{e2}/f_2\left(\overline{\alpha}_2\right)\right] - \left[V_{e1}/f_1\left(\overline{\alpha}_1\right)\right]}{g_1\left(\overline{\alpha}_1\right) + g_2\left(\overline{\alpha}_2\right)}. \tag{4.17}$$

From the sensor inclination angle $\overline{\alpha}_i$, the functions $f_i\left(\overline{\alpha}_i\right)$ and $g_i\left(\overline{\alpha}_i\right)$ were defined as

$$f_i\left(\overline{\alpha}_i\right) = \left(cos^2\overline{\alpha}_i + k_i^2 sin^2\overline{\alpha}_i\right)^{1/2} \tag{4.18}$$

$$g_i\left(\overline{\alpha}_i\right) = \frac{\left(1-k_i^2\right)cos^2\overline{\alpha}_i}{cos^2\overline{\alpha}_i + k_i^2 sin^2\overline{\alpha}_i} \times tan\overline{\alpha}_i. \tag{4.19}$$

After each calibration, velocity tests were conducted on the calibration jet at random velocities within the range of calibration. An example of velocity tests is shown in Figure 4.13.

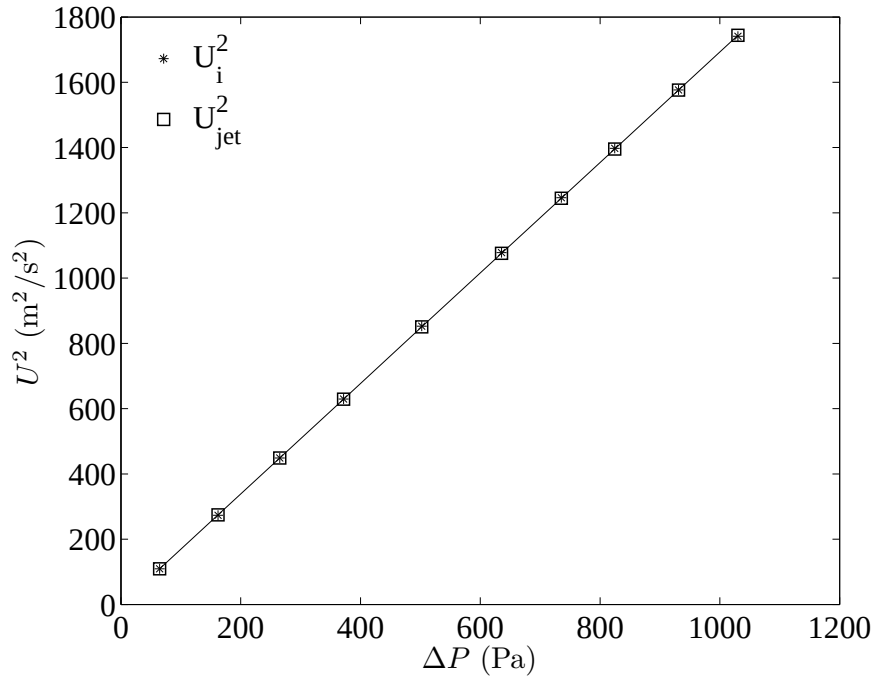

Figure 4.13: Example of velocity tests after calibration. Solid line indicates linear curve fit.

Each calibration was repeated if the relative difference b between the hot-wire streamwise velocity U_i and the velocity of the calibration jet U_{jet} exceeded 0.5%. b was calculated as

$$b = 100 \times \sqrt{\frac{1}{N}\sum_{i=1}^{N}\left(\frac{U_i - U_{jet}}{U_{jet}}\right)^2}. \tag{4.20}$$

U_{jet} was calculated as

$$U_{jet}^2 = \frac{2}{\rho\left[1-\left(A_o/A_i\right)^2\right]}\Delta P\ , \tag{4.21}$$

where A_o and A_i are the jet outlet and inlet cross areas, respectively.

It should be noted that in this study, the angle of the sensors, $\overline{\alpha}$ differed by about

1 to 2 degrees from the original inclination (45°) at the time of probe purchase from the manufacturer. This difference may be due to deformations caused by heating the sensors at high temperatures and required that the probe be operated for a certain amount of time prior its use for measurements. The anemometer was readjusted to account for any changes in the sensors resistance and the probe was recalibrated.

4.5 Signal conditioning and data acquisition systems

4.5.1 Signal conditioning

The hot-wire signal was amplified, offset and filtered prior to be digitized and recorded. This signal conditioning procedure was necessary to produce useful measurements. The anemometer output voltage after conditioning was

$$E_{out} = g\left(E - E_{offset}\right) \ , \tag{4.22}$$

where E is the hot-wire signal and E_{offset} is the DC offset voltage. The hot-wire signal was offset and multiplied by a gain of 2 to bring it into the working range of the data acquisition system.

4.5.2 Data acquisition systems

Three data acquisition systems were used in this study. An NI PCI-6143 data acquisition card was used to conduct all hot-wire, Pitot-static tube and Preston tube measurements. An NI cDAQ-9217 data acquisition module was used for RTD analog input and a second NI cDAQ-9263 module was used to set the blower fan speed. Both NI cDAQ-9217 and NI cDAQ-9263 modules were installed on a NI cDAQ 9174 4-slot chassis. All three data acquisition systems were manufactured by National Instruments.

NI PCI-6143 data acquisition system

The NI PCI-6143 had eight dedicated ADC 16-bit analog input channels and was capable of simultaneous sampling at 250 kHz per channel. It had a analog input signal range of ±5 V. A shielded BNC adapter block (National Instruments, model BNC-2110) was used to transfer the analog input signals to the data acquisition card.

NI cDAQ-9217 data acquisition module

The NI cDAQ-9217 was used to digitize the analog input signal of the RTD. It had four 24-bit analog input channels and a sampling rate of 100 Hz per channel. The RTD readings were converted to temperature using the calibration information provided by the manufacturer.

NI cDAQ-9263 data acquisition module

A NI cDAQ-9263 module was used to set the blower fan to the desired speed. The module had four channels, which could update their analog outputs at a rate of 100 kHz per channel simultaneously. Each channel had an AO terminal and a common terminal, which was internally connected to the ground reference of the module.

4.6 Measurement procedures

4.6.1 Estimation of the correction factor and the bulk velocity

The bulk velocity was estimated from the measured flow rate through the contraction assuming that leakage was negligible. For symmetrical contractions, two pressure taps, one at the inlet and another at the throat area of the contraction, suffice to estimate the flow rate. For a partially symmetrical contraction, such as the one used in this study, this method may introduce some errors because the pressure distribution across the throat may not be uniform. In that case, a correction factor should be determined to compute the actual flow rate measurement from the measured pressure difference.

To determine the correction factor c used in the bulk velocity equation (Eq 3.8), the throat of the main contraction was divided into 45 identical rectangular quadrants as illustrated in figure 4.14. The velocity at the centre of each quadrant was measured using a Pitot-static tube for a wide range of fan speeds and was assumed to be uniform in the quadrant. A velocity map was constructed and the true flow rate at each fan speed was calculated by integrating the velocity map over the throat area. The correction factor at each fan speed was calculated by dividing the corresponding true flow rate by the flow rate obtained by multiplying the velocity at the throat centre

by the throat area. The Pitot-static tube was kept permanently at the center of the throat area and the average value ($c = 0.976$) of all the correction factors was used throughout this study.

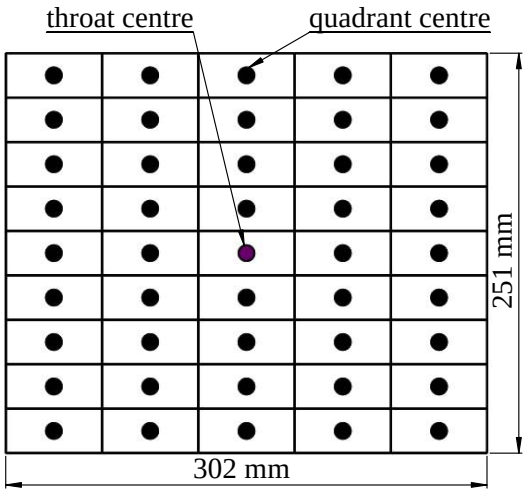

Figure 4.14: Throat area of the contraction.

4.6.2 Cross-wire velocity measurements

A cross-wire probe was mounted on the traversing system and inserted with its tip located at $33.8D$ from the inlet of the test section. Measurements were taken radially at 1 mm increments for 30 angular locations ϕ around the central rod. Details on coordinate system used is shown in figure 3.2. The hot-wire signals were corrected for temperature variation measured by an RTD installed next to the probe (see section 4.4.2). The experiment was conducted at Reynolds numbers 50,000, 100,000, and 130,000. At each Reynolds number, the probe was carefully oriented with the use of a cathetometer to acquire the streamwise and radial velocities then its body was rotated 90 degree to measure the azimuthal velocity component. Hence, two sets of measurements were taken for each Reynolds number.

The hot-wire signals at Reynolds number 50,000 were low pass filtered at 14.3 kHz and sampled at a rate of 30 kHz. For the two other Reynolds numbers (namely, 100,000 and 130,000), the low pass filters on the anemometer were set at their maximum values (21.8 kHz) and the signals were sampled at a rate of 70 kHz. The RTD was sampled at 5 Hz. The filtered hot-wire signals and the RTD signals were digitized

using a 16-bit PCI-6143 and a 24-bit cDAQ-9217 National Instrument data acquisition, respectively. The hot-wire time series consisted of 9×10^6 and 21×10^6 samples for the lowest Reynolds number and the two other Reynolds numbers, respectively. The data were collected in 100 blocks with each block long enough to ensure convergence; the block time was at least 200 times the corresponding integral time scale. Table 4.3 summarises the measurement settings.

Reynolds number	50,000	100,000	130,000
Cut-off frequency (kHz)	14.3	21.8	21.8
Sampling rate (kHz)	30	70	70
Number of blocks	100	100	100
Samples per block	90,000	210,000	210,000
Total number of samples	9,000,000	21,000,000	21,000,000

Table 4.3: Cross-wire velocity measurements settings.

4.6.3 Wall shear stress measurements

The Preston tube technique described in section 4.4 was validated against pressure drop in a fully developed pipe flow of air. The wall shear stress was estimated as

$$\tau_w = \frac{\Delta P D}{4L} \ , \tag{4.23}$$

where D is the inner diameter of the pipe and ΔP is the pressure drop across two pressure taps separated by a distance L along the fully developed region of the flow. The set-up used to conduct the validation consisted of a pipe with $D = 0.032$ m and a total length of 6.10 m, supplied with air by a blower. Tests were conducted for three distinct blower speeds, which could not be estimated in this case but are expected to be within the range of interest. Figure 4.15 shows that the Preston tube measurements agreed with the wall shear stress estimated from equation 4.23 within approximately 6%. The difference was not systematic and may be attributed to precision uncertainty.

For measurements in the rod bundle, the pressure difference ΔP near the surface of the central rod was estimated with a Preston tube and a pressure tap on the upper

cover of the test section. The static pressure was assumed to be uniform around the rod. Measurements were conducted at 21 angular locations around the periphery of the central rod at Reynolds numbers 50,000, 100,000 and 130,000. A total of 3,000,000 samples were recorded at a rate of 10 kHz for each Reynolds number.

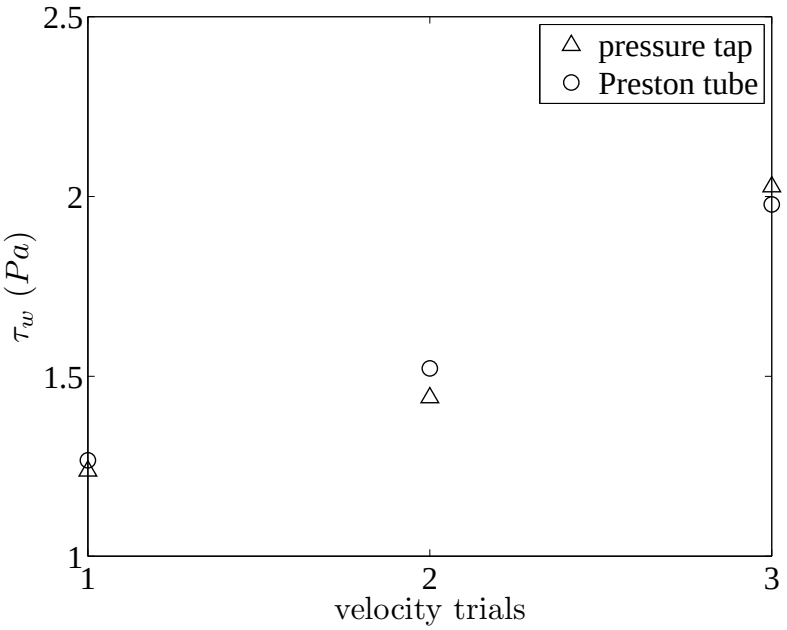

Figure 4.15: Validation of Preston tube technique.

4.6.4 Detection of Coherent structures

A right-angle hot-wire probe was inserted at each of the five ports along the top cover of the test section and measurements were taken at three Reynolds numbers 50,000, 100,000 and 130,000. The anemometer signals were low-pass filtered at 4.11 kHz and sampled at 10 kHz for 300 s, which resulted in 3,000,000 samples. In addition to the analog filtering, the hot-wire signals were digitally filtered using a double-pass seventh-order Butterworth filter to separate the non-coherent structures from the coherent structures during post-processing. The cut-off frequency on the digital filter was set at 30 Hz, 45 Hz and 50 Hz, for the Reynolds numbers 50,000, 100,000 and 130,000, respectively. Hot-wire velocity calibration was not required during this study. Instead, the DC offset on each of the anemometer module was adjusted until the mean difference between the output voltages of the probe sensors was no longer

sensitive to the streamwise velocity. This operation was performed on the calibration jet and allowed the hot-wire to only be sensitive to the cross-flow velocity fluctuations.

The convection speed of the coherent structures responsible for strong flow in the rod-wall gap was studied at Reynolds numbers ranging from 50,000 to 130,000. The convection speed of the coherent structures was determined using two hot-wire probes mounted at the center of the gap and separated by a distance of one rod diameter. The probes were operated simultaneously and similar measurements and post-processing techniques used in the detection of the coherent vortices were utilized for both probes. The convection speed of the coherent structures was calculated as

$$U_c = \frac{d}{\tau_d} \ , \tag{4.24}$$

where d is the distance between the tips of the probes and τ_d is the time delay obtained from the cross-correlation as illustrated in figure 4.16.

The average distance between two consecutive structures, λ_c was determined as

$$\lambda_c = \frac{U_c}{f_p} \ , \tag{4.25}$$

where f_p is the peak frequency of the cross velocity power spectrum.

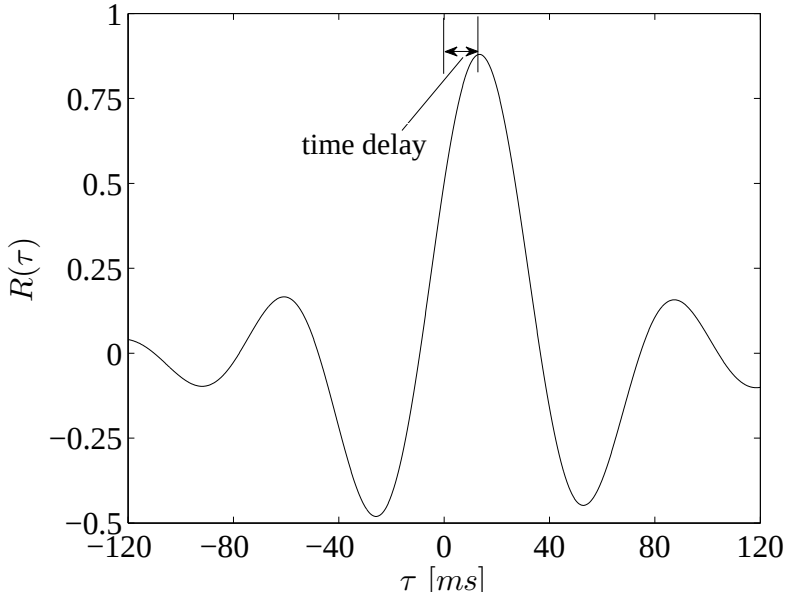

Figure 4.16: Representative cross-flow velocity cross-correlation coefficient.

4.7 Hot-wire resolution and velocity measurement uncertainty

4.7.1 Hot-wire resolution

Measurement of the fine-scale structure of the turbulent velocity field using hot-wire anemometry requires an adequate miniaturization of the sensor(s) dimensions to minimize spatial and temporal filtering of the hot-wire signal. Several authors have observed that these filtering effects often result in an underestimation of $\overline{(\partial u/\partial x)^2}$ and $\overline{(\partial u_r/\partial x)^2}$, which lead to an overestimation of the Taylor and Kolmogorov microscales. Wyngaard [1969] proposed a correction method for $\overline{(\partial u_r/\partial x)^2}$ measured by a cross-wire but only provided corrections for $\overline{(\partial u/\partial x)^2}$ measured by a normal hot-wire. To estimate a correction for the latter property, we shall use the isotropic expression

$$\overline{\left(\frac{\partial u}{\partial x}\right)^2} = \frac{1}{2}\overline{\left(\frac{\partial u_r}{\partial x}\right)^2}. \tag{4.26}$$

Measured and corrected values of $\overline{(\partial u/\partial x)^2}$, $\overline{(\partial u_r/\partial x)^2}$, the Taylor micrcoscale and the Kolmogorov microscale at $\phi = 0°$ and $r/D = 0.518$ are presented in table 4.4. After correction, the Taylor microscale decreased by 8.3%, 13.6% and 25%, and the Kolmogovov microscale decreased by 3.8%, 8.4% and 12.3% for Reynolds numbers 50,000, 100,000 and 130,000, respectively.

Reynolds number	50,000		100,000		130,000	
$\overline{(\partial u/\partial x)^2}$ $(1/s^2)$	$1.35 \cdot 10^5$	$\mathbf{1.56 \cdot 10^5}$	$6.53 \cdot 10^5$	$\mathbf{8.89 \cdot 10^5}$	$8.91 \cdot 10^5$	$\mathbf{1.59 \cdot 10^6}$
$\overline{(\partial u_r/\partial x)^2}$ $(1/s^2)$	$1.62 \cdot 10^5$	$\mathbf{3.13 \cdot 10^5}$	$6.78 \cdot 10^5$	$\mathbf{1.78 \cdot 10^6}$	$1.14 \cdot 10^6$	$\mathbf{3.17 \cdot 10^6}$
λ (mm)	2.4	**2.2**	2.2	**1.9**	2.4	**1.8**
η (μm)	105	**101**	71	**65**	65	**57**

Table 4.4: Measured and corrected values of $\overline{(\partial u/\partial x)^2}$, $\overline{(\partial u_r/\partial x)^2}$, the Taylor microscale and the Kolmogorov microscale. The corrected values are in bold.

4.7.2 Velocity measurement uncertainty

In this study, the measurement uncertainty of a measured parameter X (i.e. $\overline{U}$, $\overline{u^2}$, or $\overline{(\partial u/\partial x)^2}$) was defined as

$$\delta X = \sqrt{b^2 + p^2} \ , \tag{4.27}$$

where b and p are the bias and precision uncertainties, respectively.

The portion of the total bias uncertainty that was due to differences between calibration and measurement was estimated from equation 4.20 to roughly 0.5% of the measured quantity. It was assumed that this bias uncertainty accounted for drifts in all instruments used and errors in calibration. Other types of bias that were considered were those introduced by sensor vibrations and possible probe misalignment with respect to the incoming flow.

The hot-wire probe holder was aerodynamically designed and supported firmly on the traversing system; consequently, effects of mechanical vibrations on the measured turbulence may be considered as being negligible.

Cross-wire probes may be subjected to errors caused by cross-talk between the two sensors, if they are spaced sufficiently closely to each other. Jerome et al. [1970] found that such errors would be appreciable only when the ratio of the separation distance to the length of the sensors is less than 0.15. This ratio was 0.5 for the probe used in this study and so errors due to sensor spacing may be deemed to be negligible.

The effect of the hot-wire probe misalignment with respect to the incoming flow on the mean flow velocity was studied on the calibration jet for pitch angles ranging from -3° to 3°. It was determined that within this range, the measured mean flow velocity ranged between 0.1 and 0.4% of its correct value. When inserted in the test section, the axis of the probe with respect to the incoming flow was estimated to be less than 1° and so the effect probe misalignment on the mean flow velocity was no more than 0.3%. This value was within the range of bias uncertainty mentioned previously. In addition, Strohl and Comte-Bellot [1973] predicted that probe misalignment would mostly affect the Reynolds shear stress, which would have an error of 2% for a misalignment of about ±1°.

Based on the uncertainty of the diameter of the test section rods, the bias error on the total open area of the test section was estimated to be approximatively 1%. The flow rate in the intake contraction was assumed to have a precision uncertainty of about 2% and a negligible bias error. Assuming no leaks, the uncertainty of the

bulk velocity was estimated from equation 4.27 to be 2.2%.

The aluminium frames supporting the rods at the downstream end of the test section were at a considerable distance from the end of the test section and spaced out to keep flow blockage at the outlet at a low level. In addition, the hot-wire probe was inserted from the outlet fairly deeply into the test section, so that blockage by the probe support and traversing systems would also be small. The tip of the RTD probe used for temperature correction was at approximatively 20 mm downstream of the hot-wire so that thermal effects of the hot-wires on the RTD probe and aerodynamic effects of the RTD probe on the hot-wire measurements may be considered to be negligible.

The precision limit was calculated as

$$p = 2\sigma \ , \tag{4.28}$$

where σ is the root mean square of the ensemble average of X evaluated on 100 statistically independent blocks (see table 4.3).

The uncertainty on all calculated parameters, namely the Taylor microscale and the Kolmogorov microscale was estimated by propagation of error analysis. Table 4.5 summarises the uncertainty on the measured and calculated parameters.

Reynolds number	50,000	100,000	130,000
$\delta\overline{U}$	1.3	1.4	1.5
$\delta\overline{u^2}$	6.5	5.0	5.7
$\delta\overline{v^2}$	4.4	3.3	3.4
$\delta\overline{w^2}$	4.0	3.4	3.3
$\delta\overline{uv}$	6.8	5.3	5.8
$\delta\overline{(\partial u/\partial x)^2}$	7.0	5.3	5.2
$\delta\lambda$	4.4	3.6	3.9
$\delta\eta$	1.5	1.3	1.3

Table 4.5: Relative uncertainty (%) estimates of measured properties.

Chapter 5

Experimental results and Discussion

5.1 Incoming flow conditions

The information in this section has been taken mostly from the report by Rind and Tavoularis [2012].

The uniformity of the flow in the plenum was studied at maximum flow rate achievable by this facility using a single hot-wire probe. The probe was mounted at one end of a vertical rod, which could be inserted in the plenum through one of three holes on the top of the plenum and then traversed vertically. The holes were located at the spanise positions $w/W = 0.23, 0.43$ and 0.57, as illustrated in figure 4.3. The tip of the probe was on a plane that was normal to the incoming flow and 0.53 m upstream of the test section inlet.

The variation of the normalised mean axial velocity in the plenum is presented in figure 5.1. The mean velocity was normalised by the bulk plenum velocity U_p, which was estimated from the flow rate and the cross-sectional area of the plenum. It was determined that the maximum mean velocity non-uniformity was about $\pm 13\%$ within the measuring range.

The variation of the normalised r.m.s fluctuating velocity u' is presented in figure 5.2. u' was also normalised by the bulk plenum velocity. It was found that the turbulence intensity varied in the range 1.5 to 2% within the measurement range, which is fairly low for a facility of this type. Flow straightening and turbulence reduction in the plenum are attributed to the actions of the honeycomb and perforated plates described in section 4.1.

The variation of the normalised streamwise integral length scale is shown in figure 5.3. The average value of this length scale within the measurement range was about 80 mm and its maximum non-uniformity was about $\pm 25\%$.

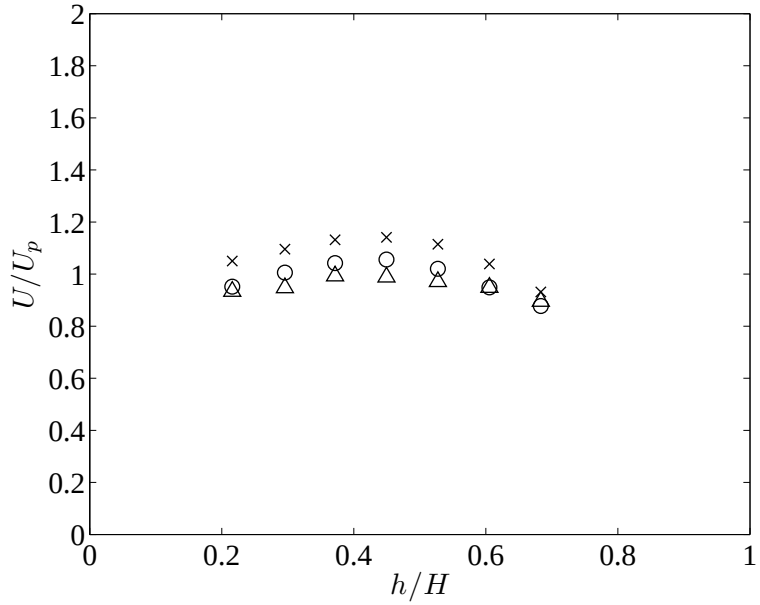

Figure 5.1: Dimensionless mean velocity profiles inside the plenum, $3.15D$ upstream of the test section inlet and at $w/W = 0.23$ (○), 0.43 (×) and 0.57 (△).

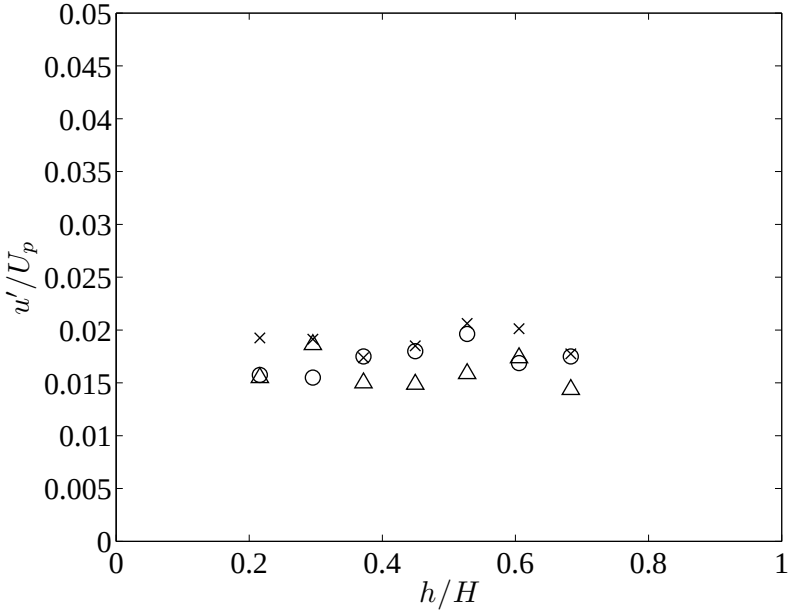

Figure 5.2: Dimensionless fluctuating velocity profiles inside the plenum, $3.15D$ upstream of the test section inlet and at $w/W = 0.23$ (○), 0.43 (×) and 0.57 (△).

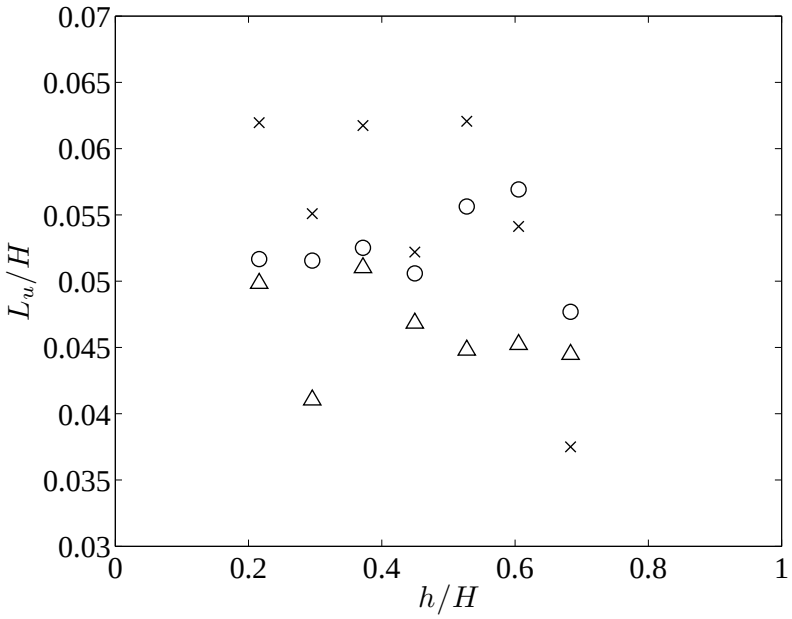

Figure 5.3: Dimensionless integral length scale profiles inside the plenum, $3.15D$ upstream of the test section inlet and at $w/W = 0.23$ (○), 0.43 (×) and 0.57 (△).

5.2 Mean flow symmetry

Early Pitot-static tube velocity measurements [Rind and Tavoularis, 2012] at the centres of all subchannels near the exit of the test section indicated that the mean velocity field was nearly symmetric about the centreplane of the test section, with measured differences between the local velocities at nominally symmetric locations being lower than 1.5%. These asymmetries were comparable to the uncertainty of local maximum velocity due to the rough positioning of the tube, which was within a radius of about 5 mm from the centre of each of the subchannels. In conclusion, these preliminary results showed no indication that there was any systematic deviation of the flow field toward one side of test section.

5.3 Mean axial velocity distribution

All velocity measurements presented below were performed using a cross-wire probe. The design of the mounting and traversing system holding the probe permitted measurements only within parts of the subchannels surrounding the central rod. The

range of radial positions for which measurements could be taken depended on the azimuthal location. The shortest possible radial distance from the rod surface was 3 mm and efforts were made to acquire data as far away from the rod surface as possible without risking damage of the probe. Measurements could not be taken at locations ranging from $-75°$ to $-165°$ because of the limited range of the rotary traverse.

Radial profiles of the normalised mean axial velocity $\overline{U}/U_b$ around the central rod are presented in figure 5.4. All profiles that extended far enough from the rod surface showed a local maximum, to be denoted as U_m; the locus of the locations of local maximum velocity in each subchannel will be referred to as the midline of the subchannel. It is also evident that the flow velocity was much higher in the open channels than in the rod-rod and rod-wall gap regions. The maximum velocity U_{max} in the part of the test section that surrounded the central rod occurred in the open subchannel below the rod, namely at $\phi = 180°$, as also illustrated in the isovelocity contour maps, shown in figure 5.5. This was to be expected as the fluid was diverted away from the vicinity of the narrow gap and toward the rest of the channel due to much higher flow resistance in the gap regions. In an operating nuclear reactor, the presence of lower velocity in the narrow gaps implies that the fluid may be subjected to higher temperatures in those regions. This is consistent with reports by Guellouz and Tavoularis [1992] that the local heat transfer coefficient would be minimum in the gap regions and maximum in the open flow regions. One should expect the mean flow velocity and the local heat transfer coefficient to decrease even further as the size of the gaps becomes smaller. Many authors, including Guellouz and Tavoularis [1992], found that the local heat transfer diminished only mildly as the gap size was decreased because of a measurable increase of the turbulent intensity in the gap, which has been attributed to large-scale coherent vortices. The bulging of the velocity contours toward the narrow gaps confirms the formation of these vortices in this present experiment as well.

The mean flow was nearly symmetric about the centreline of the test section although a small but noticeable asymmetry was detected at some azimuthal locations. This may be attributed to small errors in the positioning of the probe, the slight non-uniformity of the flow in the plenum, the small sagging of the rods at their middle

and measurement uncertainties.

The variation of the local maximum velocity U_m around the central rod is shown in figure 5.6. The ratios of the local maximum velocity and the bulk velocity in the open subchannel below the central rod and in the rod-wall and rod-rod gap regions for the three Reynolds numbers considered are shown in figure 5.7. The ratio U_m/U_b was insensitive to the Reynolds number in the open subchannel, but increased by about 5% from Re = 50,000 to 130,000 in the two gaps. The radial profiles of the normalised mean axial flow velocity also show a measurable increase of $\overline{U}/U_b$ mostly in the narrow gap regions as Reynolds number increased; the strongest effect was at $\phi = 12°$, where this ratio increased by 6.6% from Re = 50,000 to 130,000. This suggests that the wall layers in the gap regions would become thinner at higher flow rates in agreement with the literature.

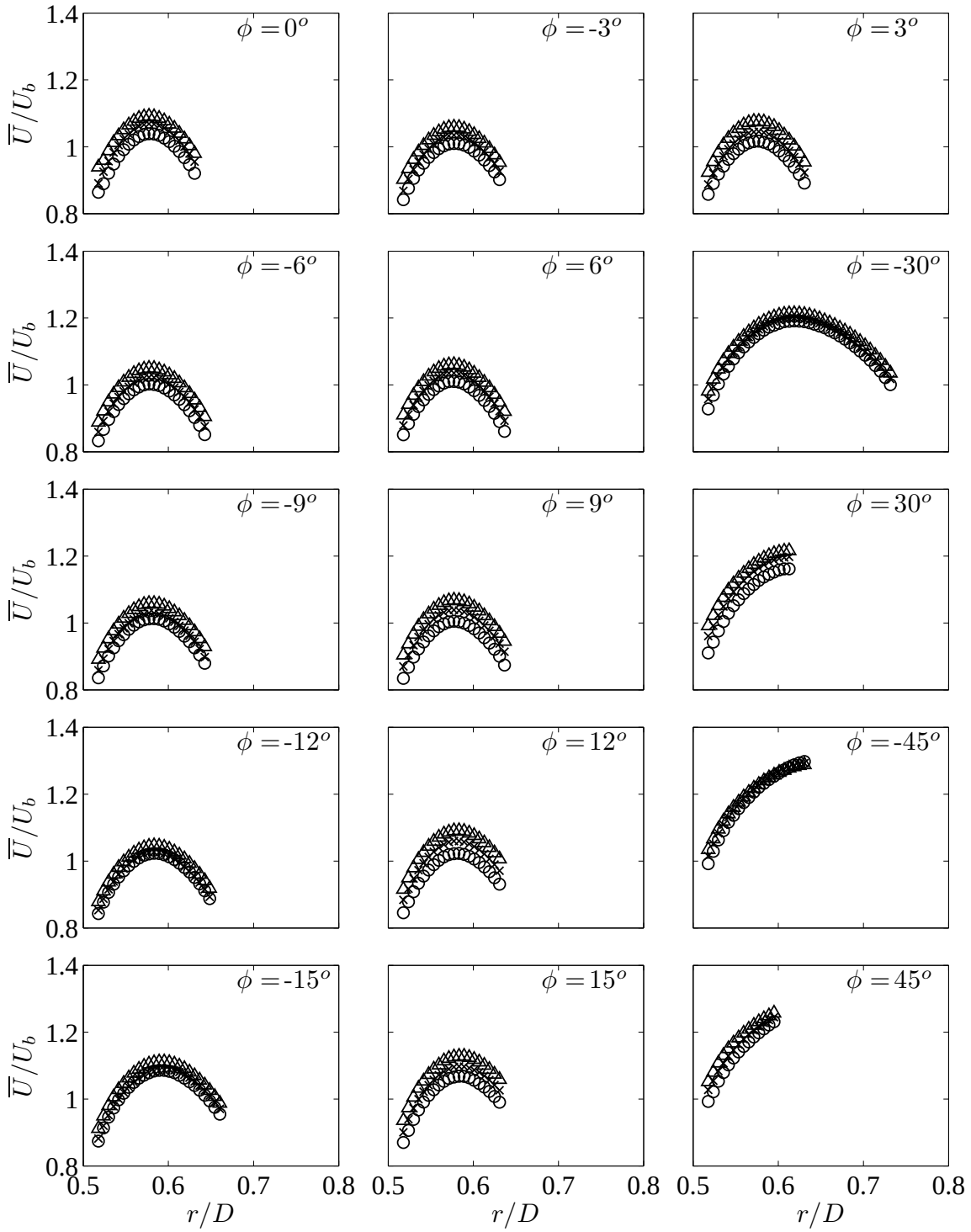

Figure 5.4: Radial profiles of the normalised mean axial velocity at various azimuthal locations and $Re = 50,000$ ($\bigcirc$), $100,000$ ($\times$) and $130,000$ ($\triangle$).

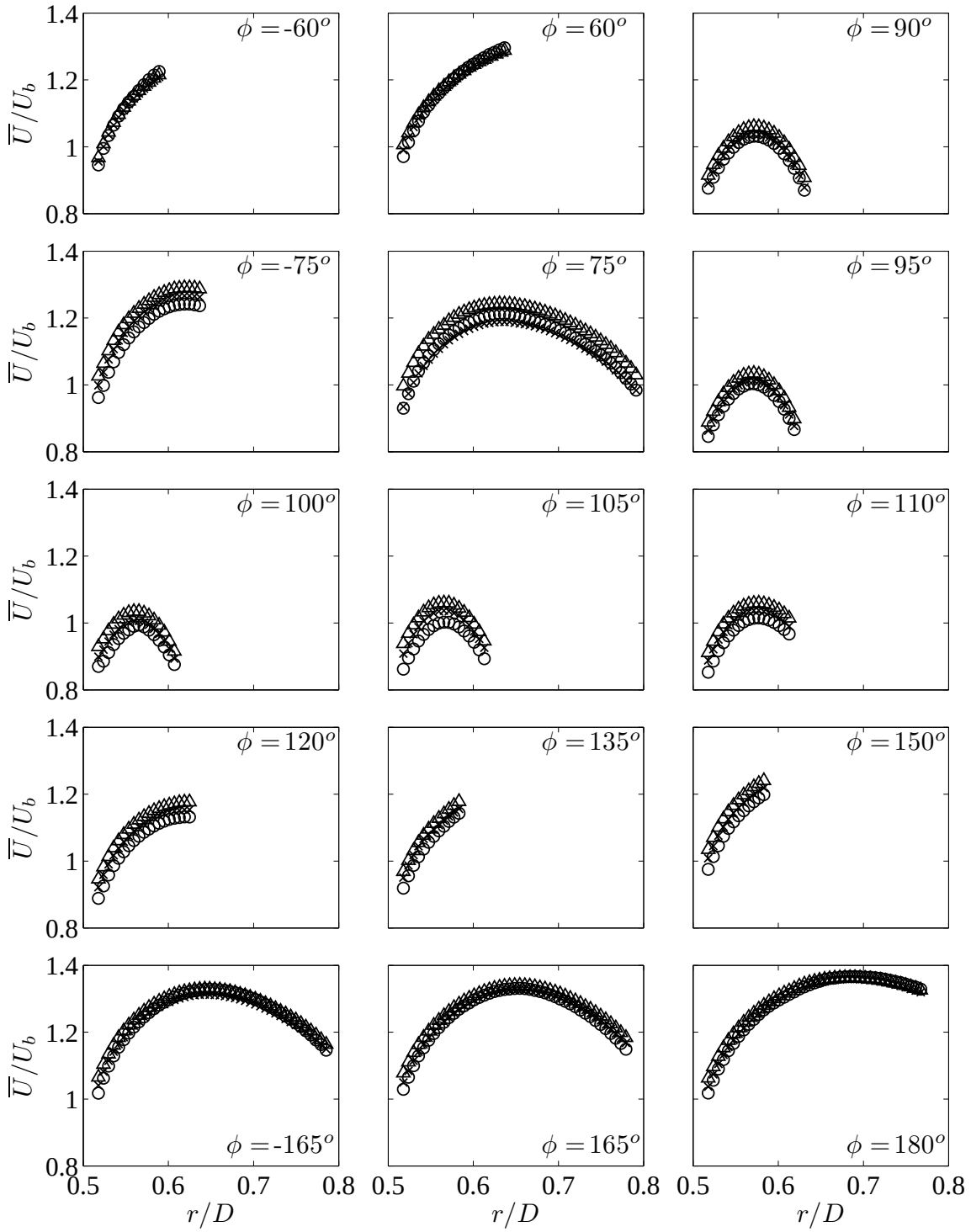

Figure 5.4 (Continued): Radial profiles of the normalised mean axial velocity at various azimuthal locations and $Re = 50,000$ (○), $100,000$ (×) and $130,000$ (△).

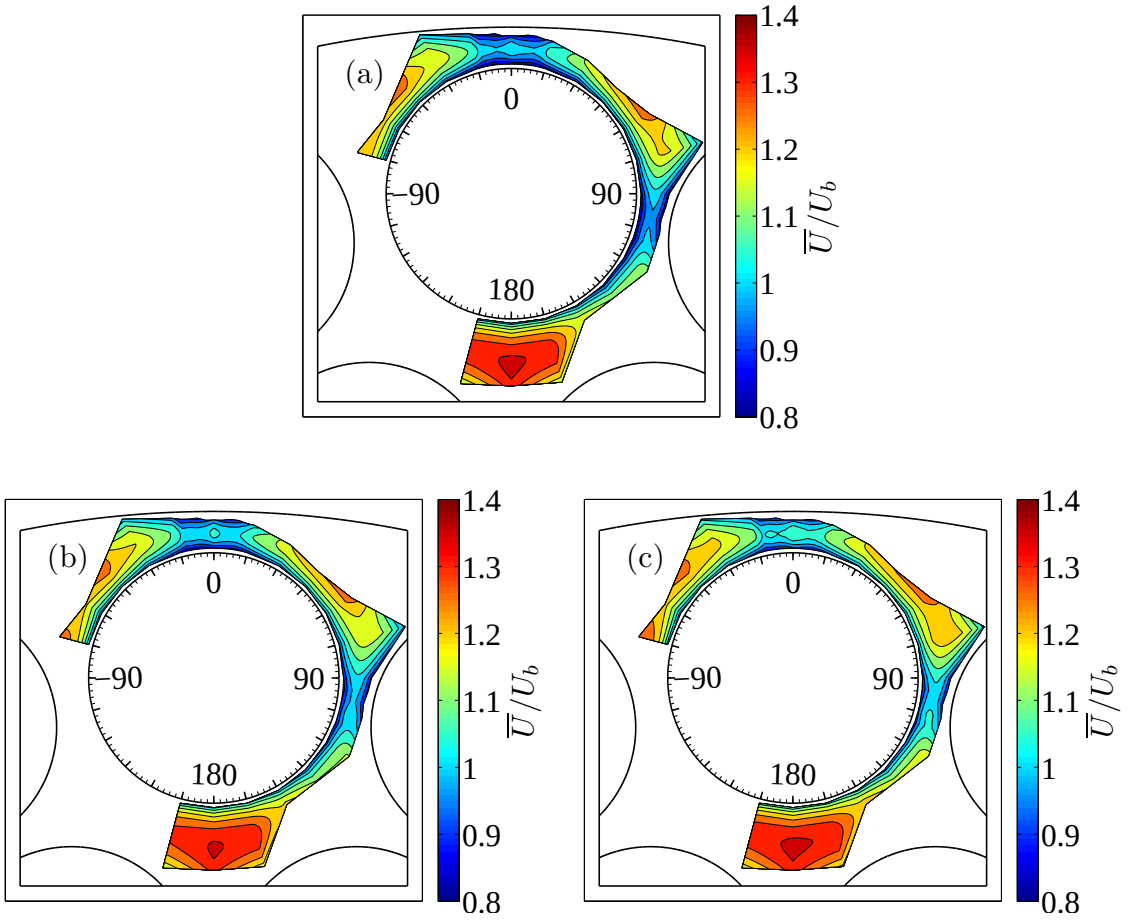

Figure 5.5: Isocontour plots of the normalised mean axial velocity for (a) $Re = 50,000$, (b) $Re = 100,000$, (c) $Re = 130,000$.

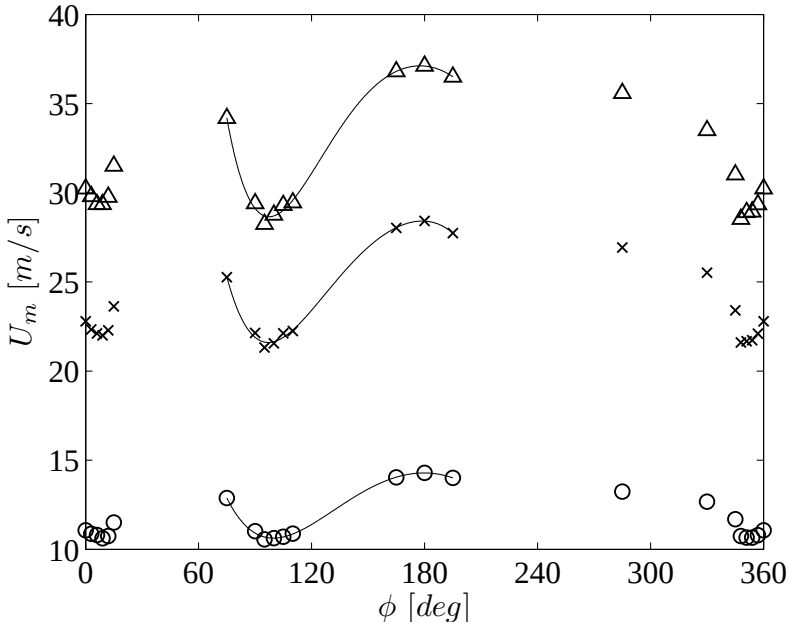

Figure 5.6: Local maximum axial velocity variation around the central rod for $Re = 50,000$ (○), $100,000$ (×) and $130,000$ (△). Solid lines indicate fourth-order polynomial curve fits.

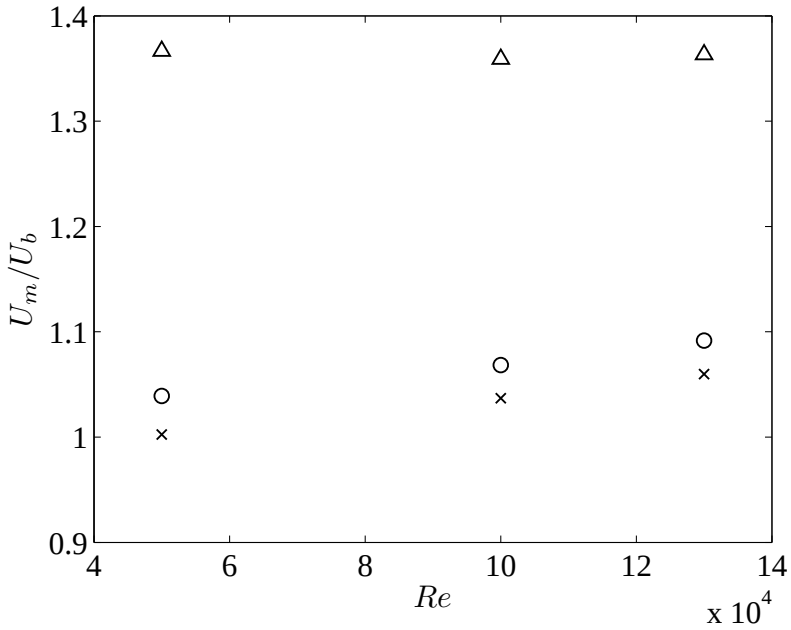

Figure 5.7: Variation of the normalised local maximum axial velocity with Reynolds number at $\phi = 0°$ (○), $105°$ (×) and $180°$ (△).

5.4 Normal Reynolds stress distribution

Figures 5.8, 5.10, and 5.12 show, respectively, radial profiles of the axial, radial and azimuthal normal Reynolds stresses at various azimuthal locations around the central rod and for the three Reynolds numbers considered. All stresses were normalised using the bulk velocity as a velocity scale. Isocontours of the normalised normal stresses are shown, respectively, in figures 5.9, 5.11 and 5.13.

All stress distributions were fairly symmetric about the geometrical plane of symmetry. Starting at the measurement locations that were closest to the rod surface, all profiles had values that decreased with increasing radial distance, reached minima, and then started increasing again, at least in the cases for which the profiles extended beyond the subchannel midline. The present spatial resolution was insufficient to resolve the wall layers and so the maxima of the stress profiles and their locations could not be determined.

On much of the measurement plane, $\overline{u^2}$ was about 70% higher than $\overline{u_r^2}$ and 50% higher than $\overline{u_\phi^2}$. This is consistent with the expectation that the stress $\overline{u^2}$ would be produced directly from the interaction between the mean shear and the shear stress as opposed to the other two stresses, which only received energy via the pressure-strain covariances. Typically for pipe flows, the radial and azimuthal stresses are nearly identical, which can be attributed to flow axisymmetry in the pipe. In this study, the uneven distribution of energy among these two stresses, especially in regions away from the narrow gaps, was in part due to the geometry of the subchannel but also to the fact that the different subchannels have free boundaries. Hence, the turbulent flow characteristics in one channel are not only dependent on the flow physics in that channel but also on those for the other channels. When viewed as a whole, the disproportionate distribution of energy among all the terms led to a significant anisotropy of the turbulent flow field in the subchannels. This makes numerical simulations of flows in rod bundle quite challenging, as one would be required to find ways to account for the anisotropy to ensure more accurate numerical predictions. The normal stresses at the measurement location closest to the wall tended to increase from the narrow gaps toward the larger channels, as a consequence of a higher velocity gradient in the larger channels. In the rod-rod gap, the values of the axial and azimuthal

stresses appeared to be higher than their corresponding values in the rod-wall gap region. Since the rod-rod gap was narrower than the rod-wall gap, this contradicts the expectation that these stresses would typically increase as the subchannel width increases. Hence, the energy of the axial and azimuthal stresses in the gap regions cannot be attributed to the local mean gradient alone. The mechanism that enhances the turbulence in gap regions of tightly packed rod bundles is large-scale transport by gap vortex streets. Ouma and Tavoularis [1991] investigated the effect of varying rod proximity on the turbulent flow characteristics in the narrow gap regions and observed that axial and azimuthal turbulence intensity increased as the gap became narrower. In a more recent study in an eccentric annular flow, Choueiri [2014] reported that the effect of these vortices on the flow characteristics became stronger as the gap size diminished in conformity with the fact that these vortices tend to be more stable for narrower gaps but start to deteriorate and become weaker as the gap size increases [Meyer, 2010]. The present results are in agreement with previous observations that the coherent vortices affect more strongly the axial and azimuthal normal Reynolds stresses than the radial one.

For the most part, as the Reynolds number increased, the normalised normal stresses decreased by measurable amounts, which is also the case for most pipe flows. The effect of Reynolds number was more noticeable on the radial and azimuthal stresses than the axial one. In the rod-wall gap, the normalised $\overline{u^2}$ showed a nearly undetectable effect of Reynolds number, but in other locations this effect was more evident.

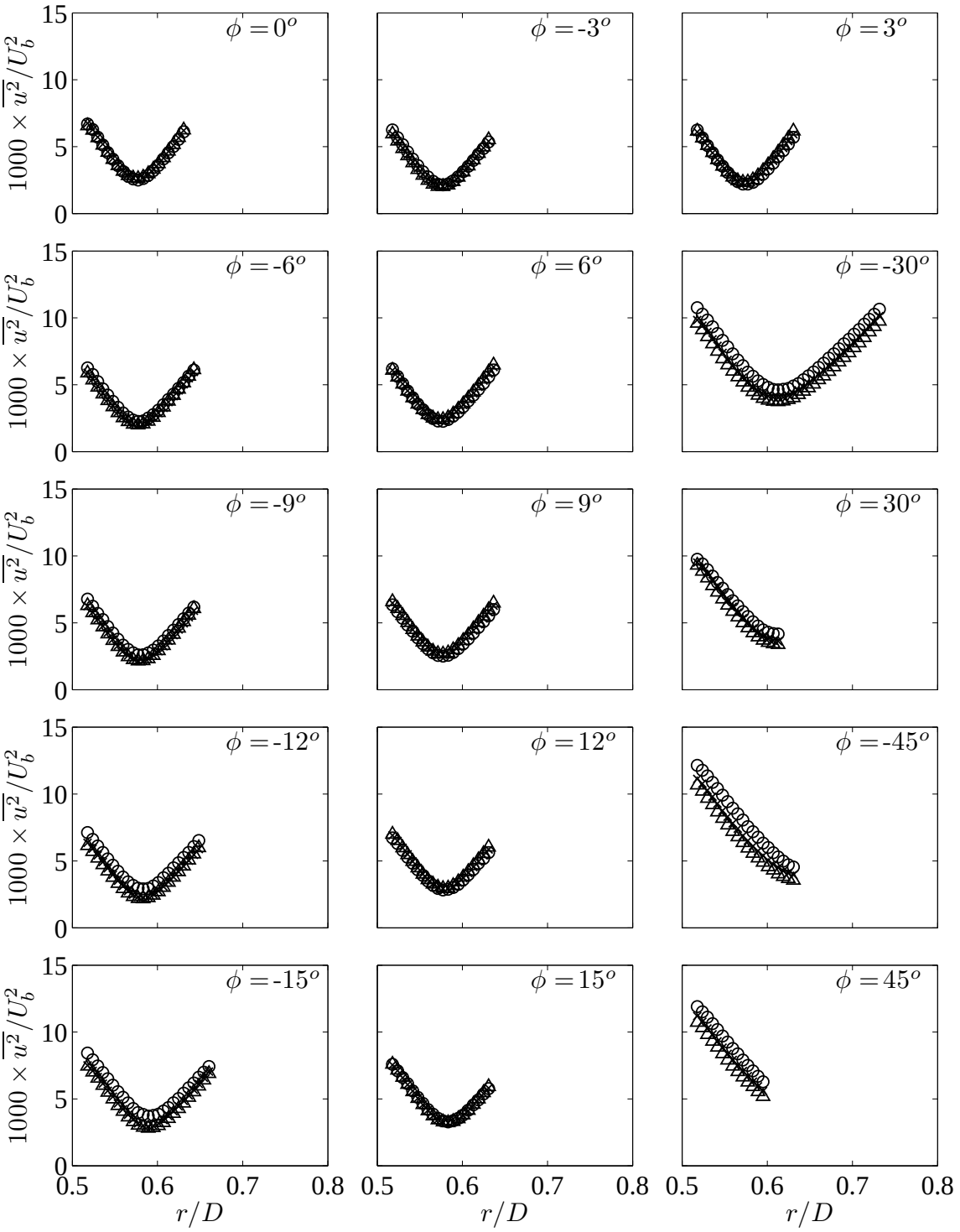

Figure 5.8: Radial profiles of the normalised axial Reynolds stress at various azimuthal locations and for $Re = 50,000$ ($\bigcirc$), $100,000$ ($\times$) and $130,000$ ($\triangle$).

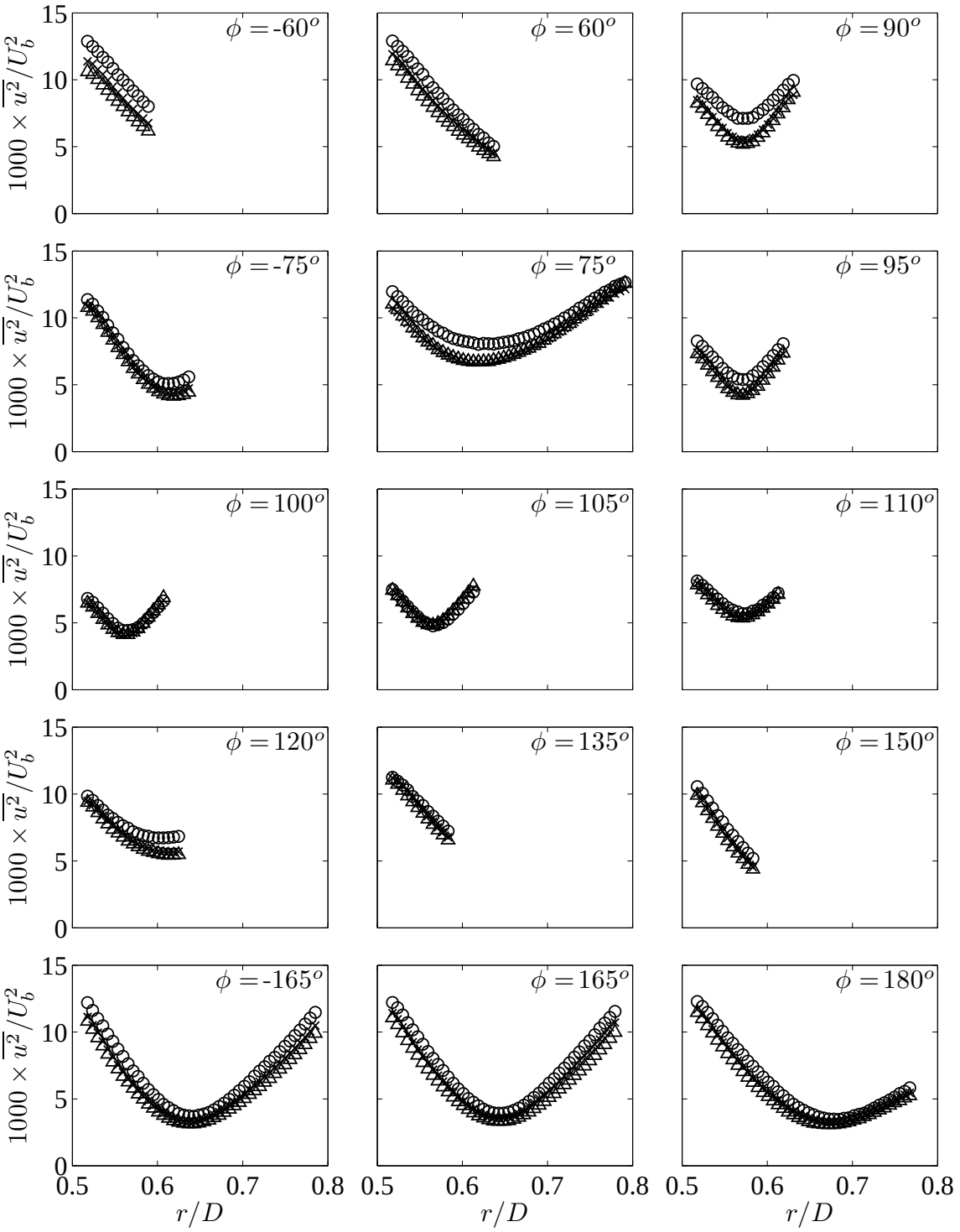

Figure 5.8 (Continued): Radial profiles of the normalised axial Reynolds stress at various azimuthal locations and for $Re = 50,000$ (○), $100,000$ (×) and $130,000$ (△).

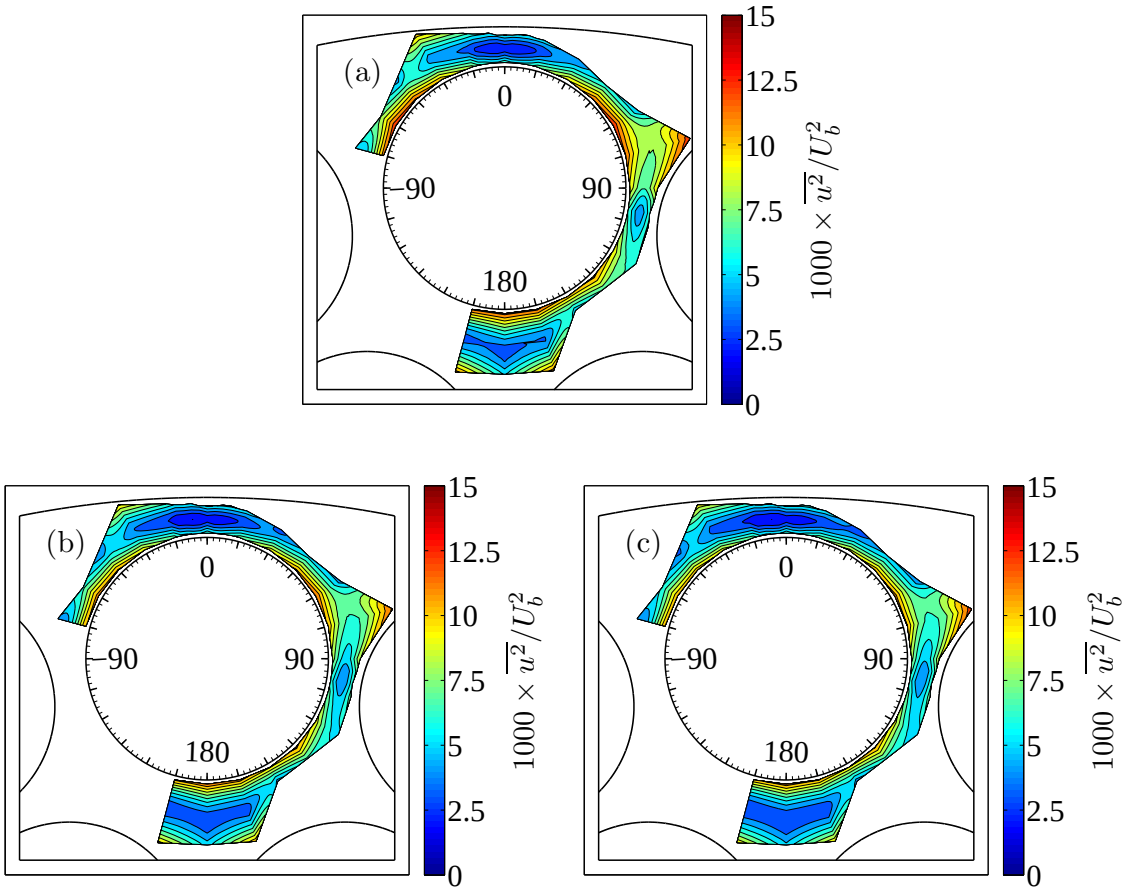

Figure 5.9: Isocontour plots of the normalised axial Reynolds stress for (a) $Re = 50,000$, (b) $Re = 100,000$, (c) $Re = 130,000$.

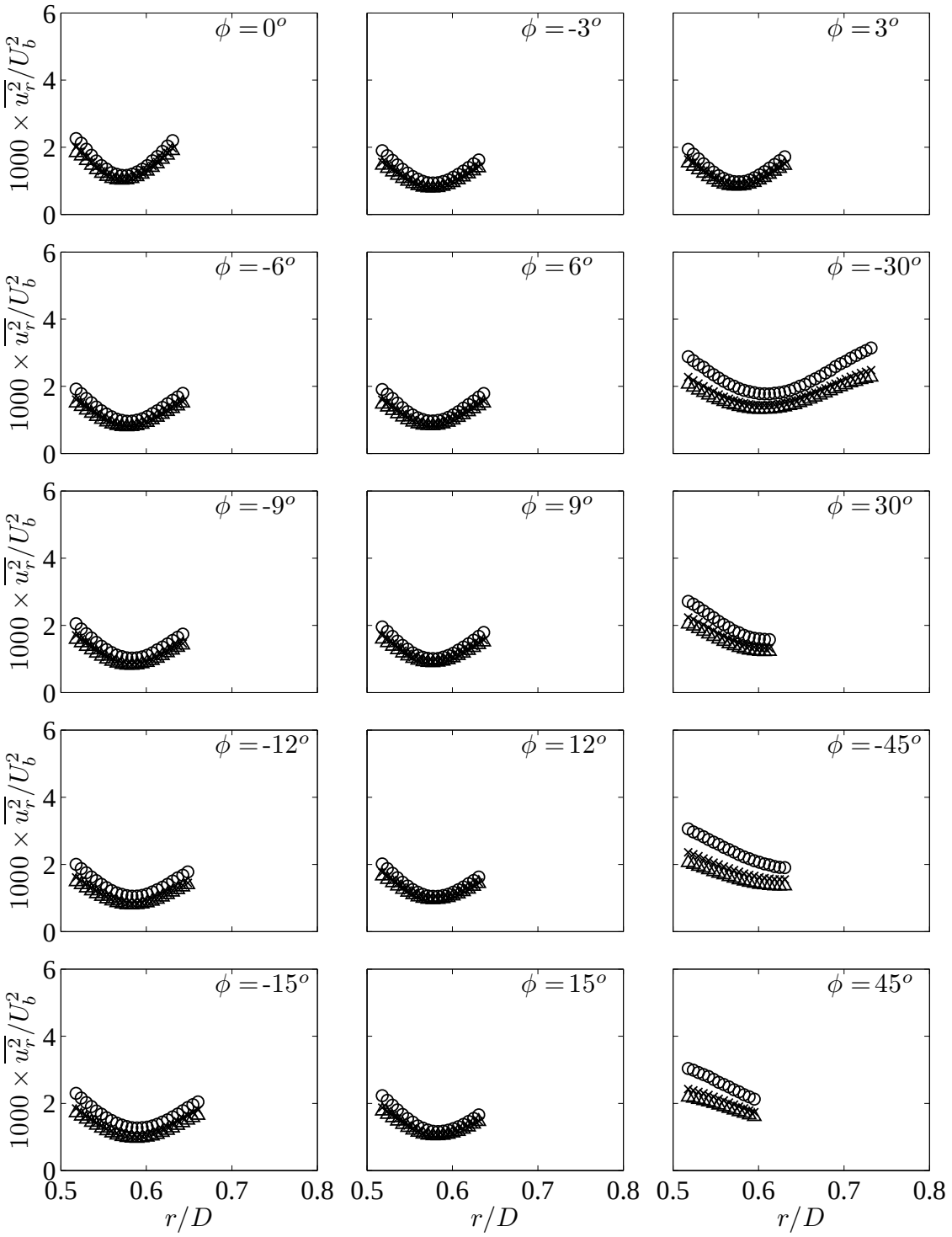

Figure 5.10: Radial profiles of the normalised radial Reynolds stress at various azimuthal locations and for $Re = 50,000$ ($\bigcirc$), $100,000$ ($\times$) and $130,000$ ($\triangle$).

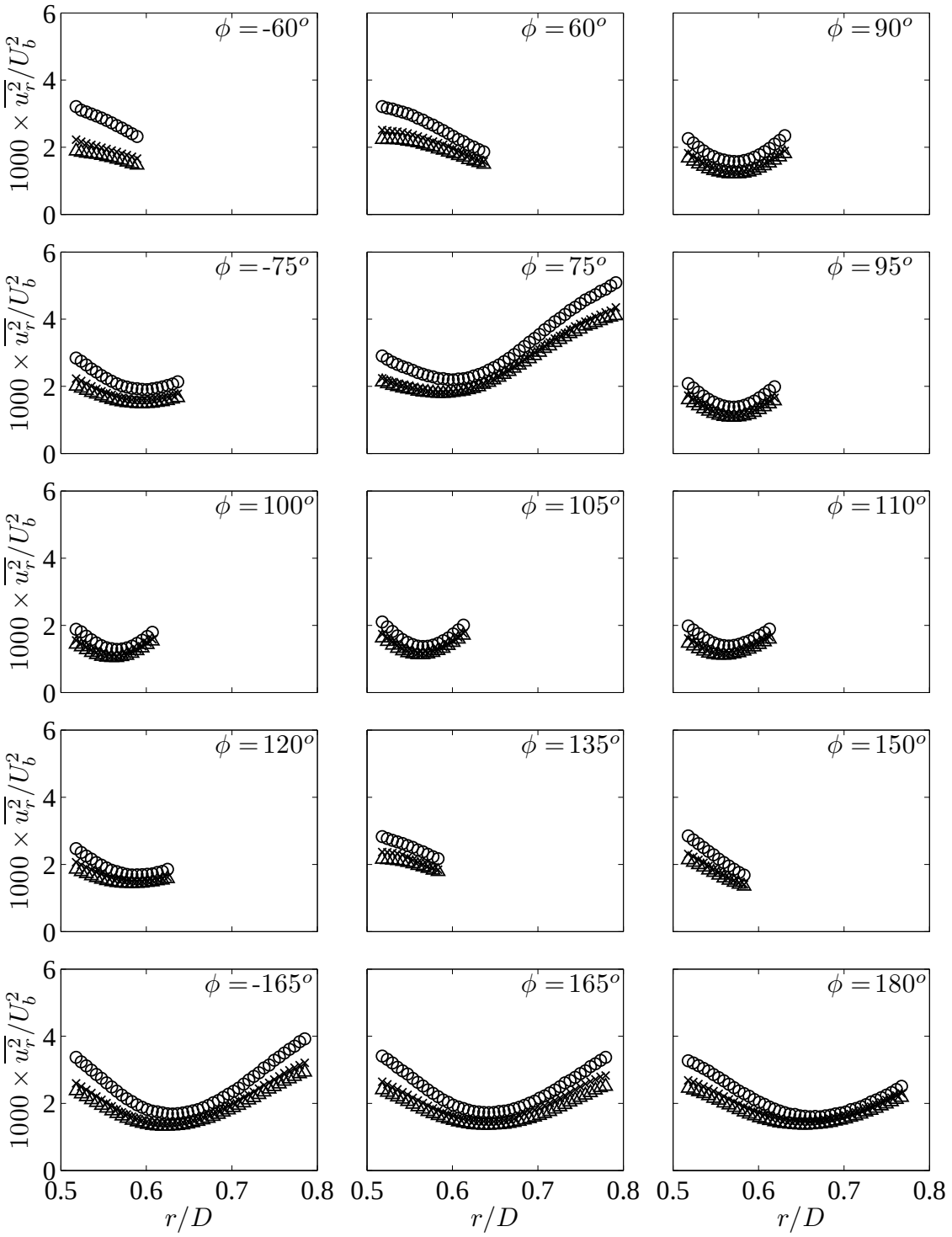

Figure 5.10 (Continued): Radial profiles of the normalised radial Reynolds stress at various azimuthal locations and for $Re = 50,000$ (○), $100,000$ (×) and $130,000$ (△).

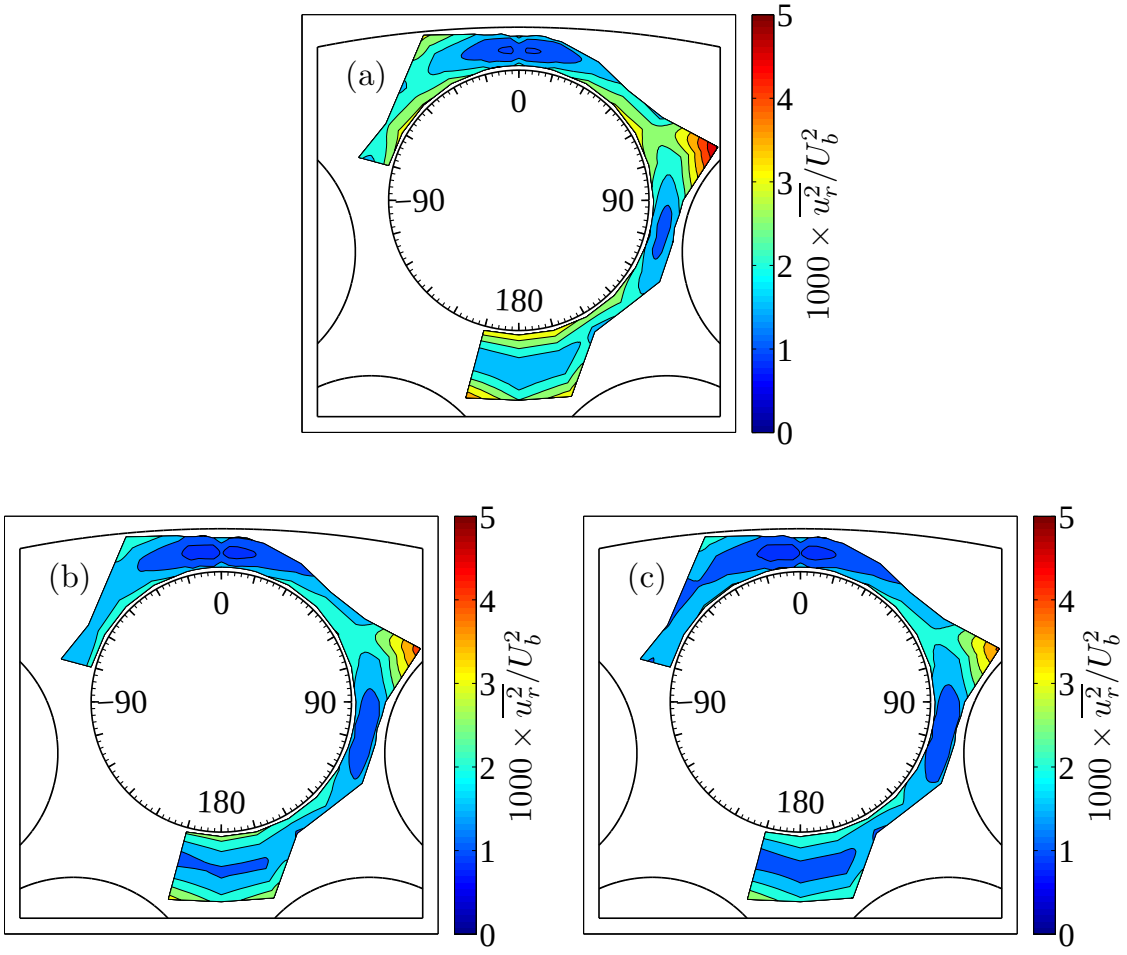

Figure 5.11: Isocontour plots of the normalised radial Reynolds stress for (a) $Re = 50,000$, (b) $Re = 100,000$, (c) $Re = 130,000$.

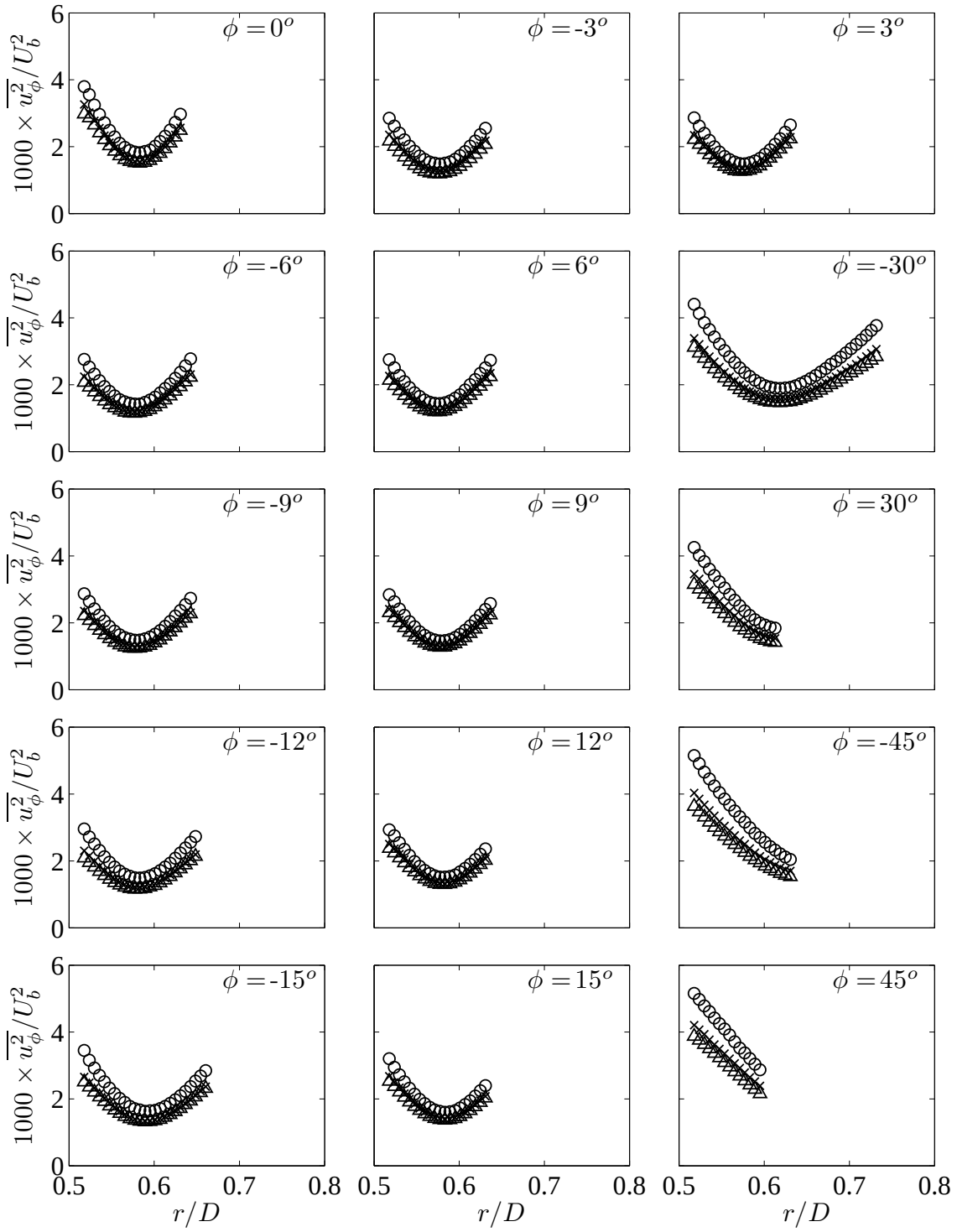

Figure 5.12: Radial profiles of the normalised azimuthal Reynolds stress at various azimuthal locations and for $Re = 50,000$ (○), $100,000$ (×) and $130,000$ (△).

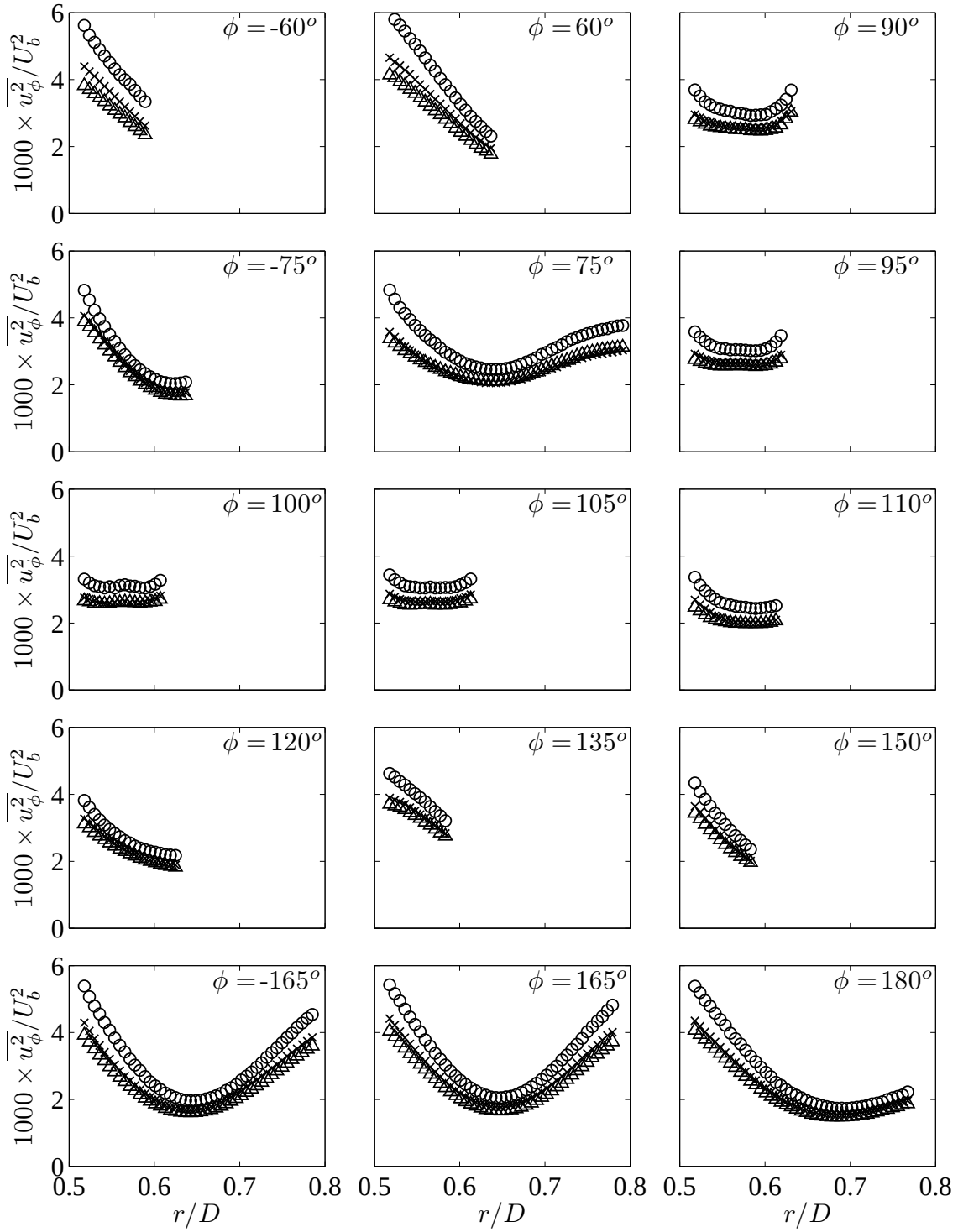

Figure 5.12 (Continued): Radial profiles of the normalised azimuthal Reynolds stress at various azimuthal locations and for $Re = 50,000$ ($\bigcirc$), $100,000$ ($\times$) and $130,000$ ($\triangle$).

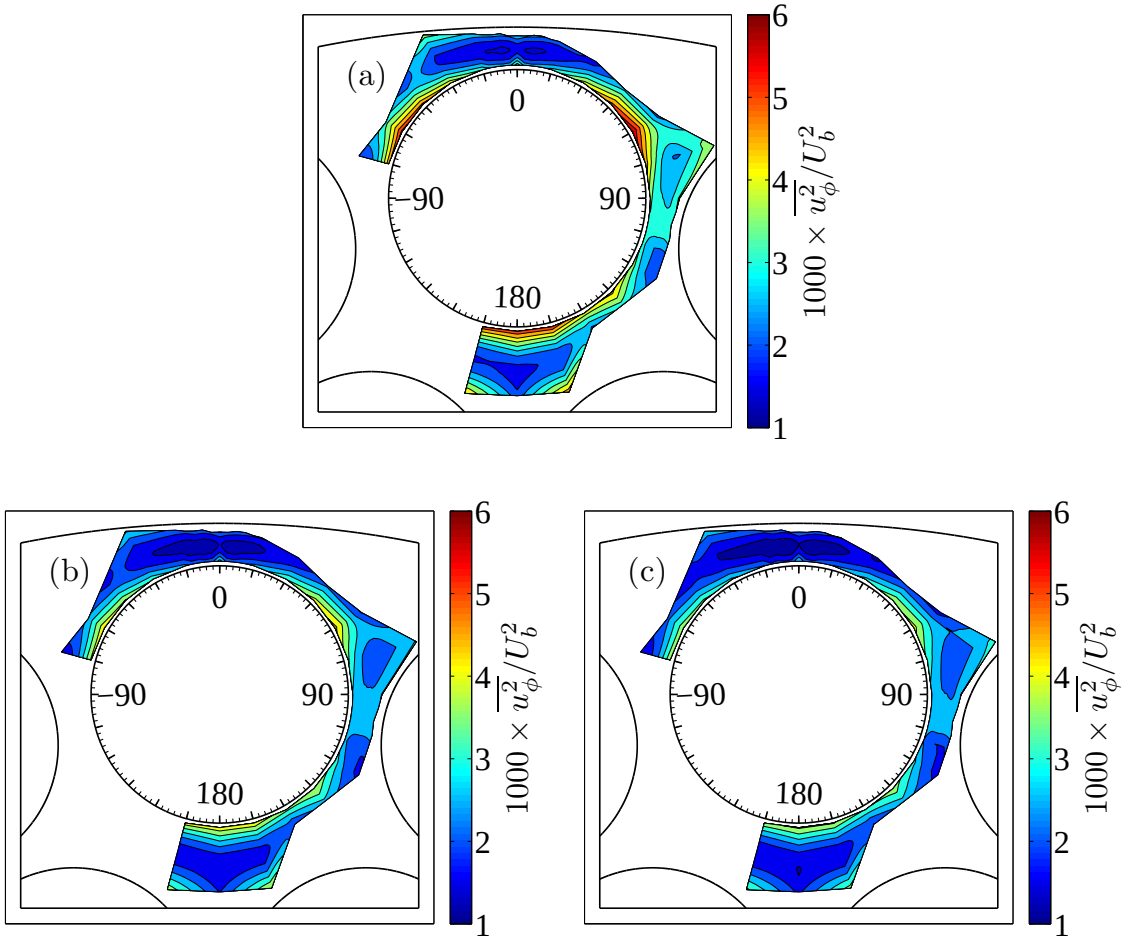

Figure 5.13: Isocontour plots of the normalised azimuthal Reynolds stress for (a) $Re = 50,000$, (b) $Re = 100,000$, (c) $Re = 130,000$.

5.5 Reynolds shear stress distribution

Reynolds shear stresses represent turbulent momentum flux per unit area. The radial distributions of the Reynolds shear stresses $\overline{uu_r}$ and $\overline{uu_\phi}$ are presented in figures 5.14 and 5.16, receptively. The shear stresses were normalised by the bulk velocity squared. The third shear stress $\overline{u_r u_\phi}$ could not be measured.

The radial Reynolds shear stress $\overline{uu_r}$ was positive near the surface of the rod and decreased to zero at the location where the magnitude of the mean axial velocity was highest (subchannel midline) and then became negative if measurements extended beyond the midlines. This is consistent with the expectation that $\overline{uu_r}$ is proportional to the opposite of the mean velocity gradient $\partial\overline{U}/\partial r$ and that $\partial\overline{U}/\partial r$ must change sign near the midline of the subchannel, where the magnitude of the mean axial velocity is highest, in conformity with the gradient transport hypothesis.

The effect of Reynolds number on the radial shear stresses could not be detected, although it appeared that the magnitude of the dimensionless $\overline{uu_r}$ decreased very slightly with increasing Reynolds number. The radial profiles of $\overline{uu_r}$ were nearly linear in the gap regions, but visibly non-linear in the open channel regions. Shown in figure 5.15 are contours of the dimensionless $\overline{uu_r}$. The contour maps showed that, for all three Reynolds numbers studied, the magnitude of $\overline{uu_r}$ measured at the closest radial distance from the rod increased from the narrow gap regions toward the open channels. This is consistent with the presence of a higher mean flow gradient near the rod in the open channel regions than in the narrow gaps. In addition, the contour maps showed that the distribution of $\overline{uu_r}$ was nearly symmetric about the test section centreplane.

Similar to $\overline{uu_r}$, the magnitude of $\overline{uu_\phi}$ was lower in the narrow gap regions than in the open channels. In all cases, the magnitude of $\overline{uu_\phi}$ was much lower than that of $\overline{uu_r}$ possibly due to higher momentum fluxes in the radial direction caused by a larger magnitude of $\partial\overline{U}/\partial r$ compared to $\partial\overline{U}/\partial\phi$. Contour maps of the dimensionless $\overline{uu_\phi}$ are presented in figure 5.17 for the three Reynolds numbers considered. Unlike $\overline{uu_r}$, $\overline{uu_\phi}$ was anti-symmetric.

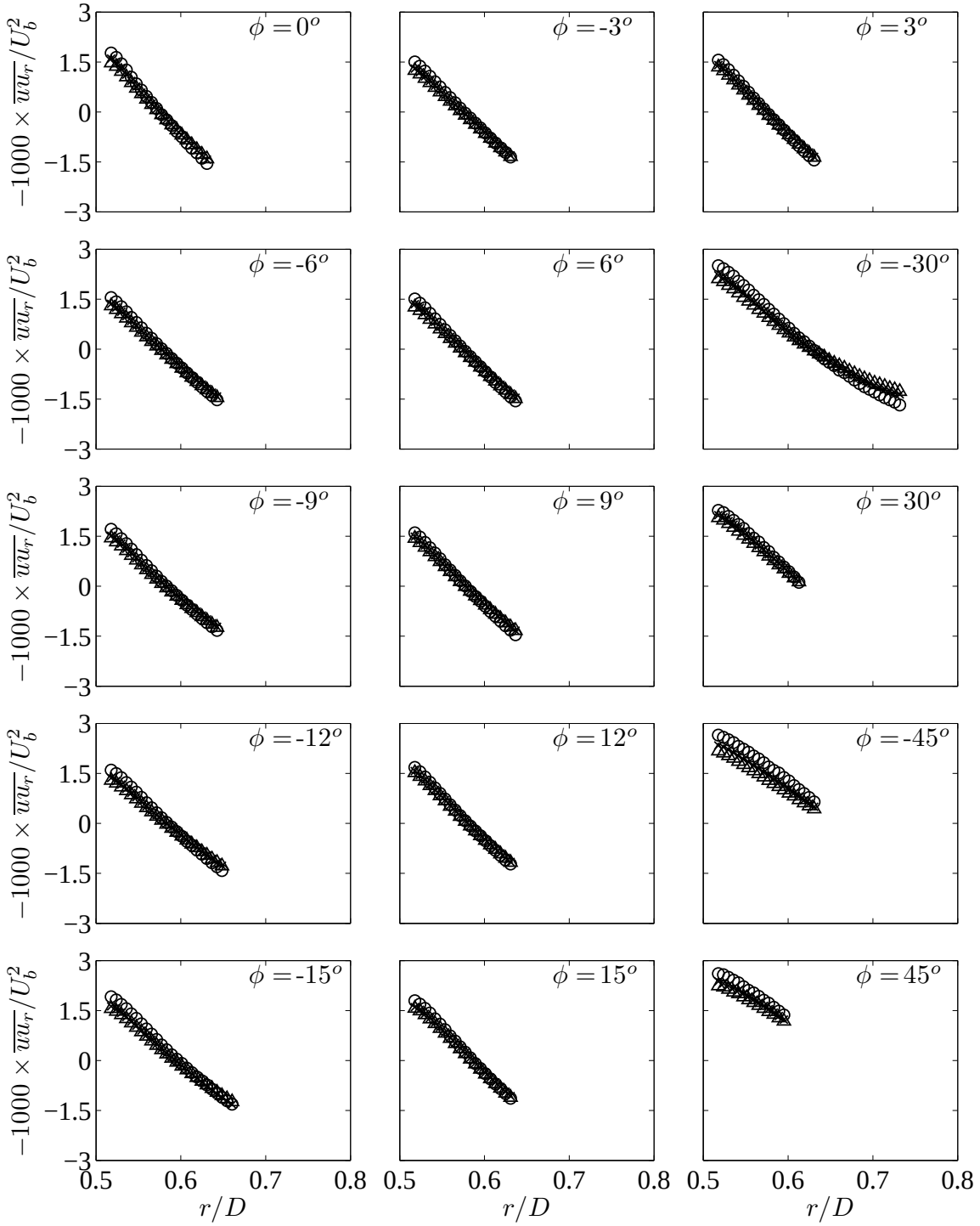

Figure 5.14: Radial profiles of the normalised radial Reynolds shear stress at various azimuthal locations and for $Re = 50,000$ (○), $100,000$ (×) and $130,000$ (△).

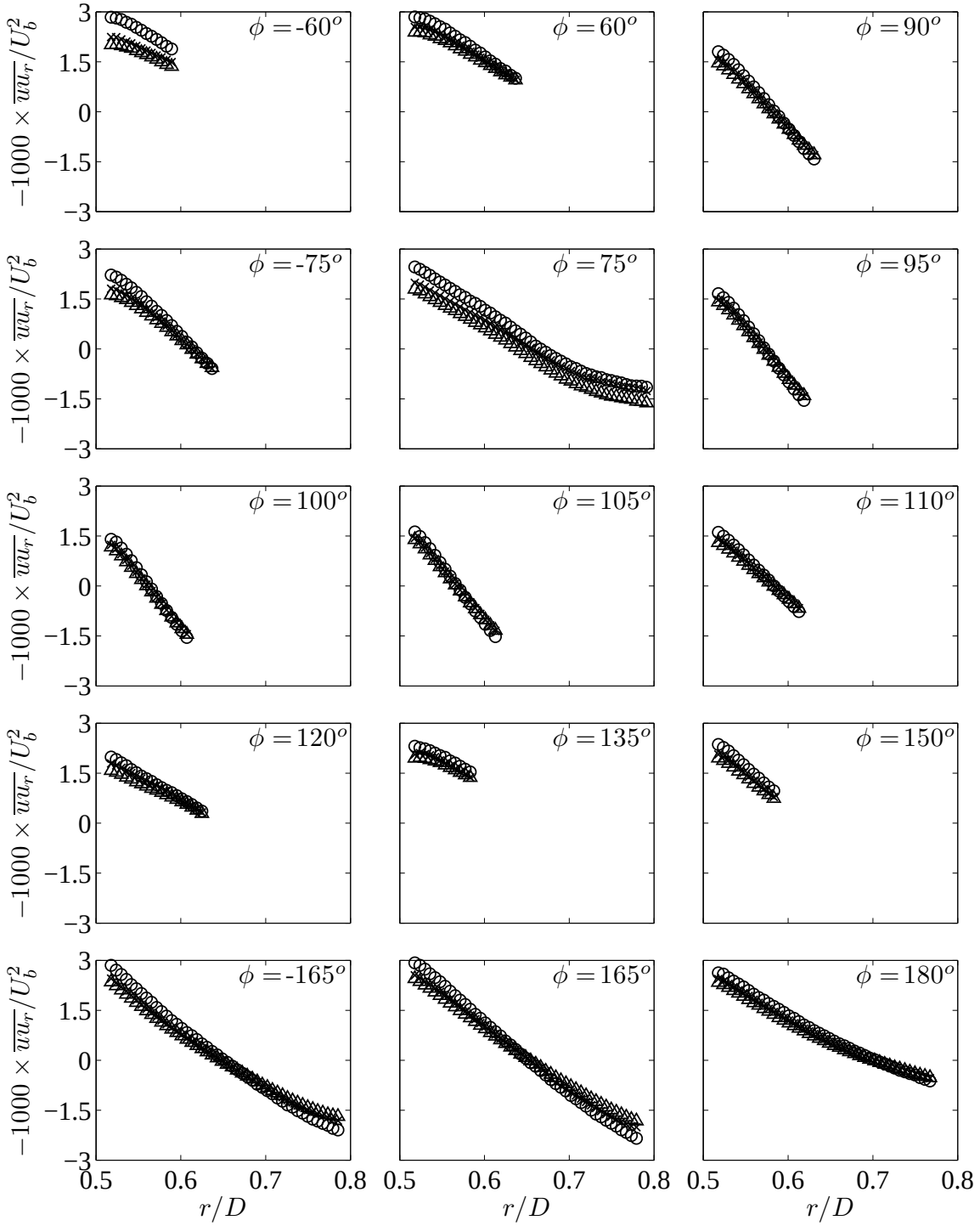

Figure 5.14 (Continued): Radial profiles of the normalised radial Reynolds shear stress at various azimuthal locations and for $Re = 50,000$ ($\bigcirc$), $100,000$ ($\times$) and $130,000$ ($\triangle$).

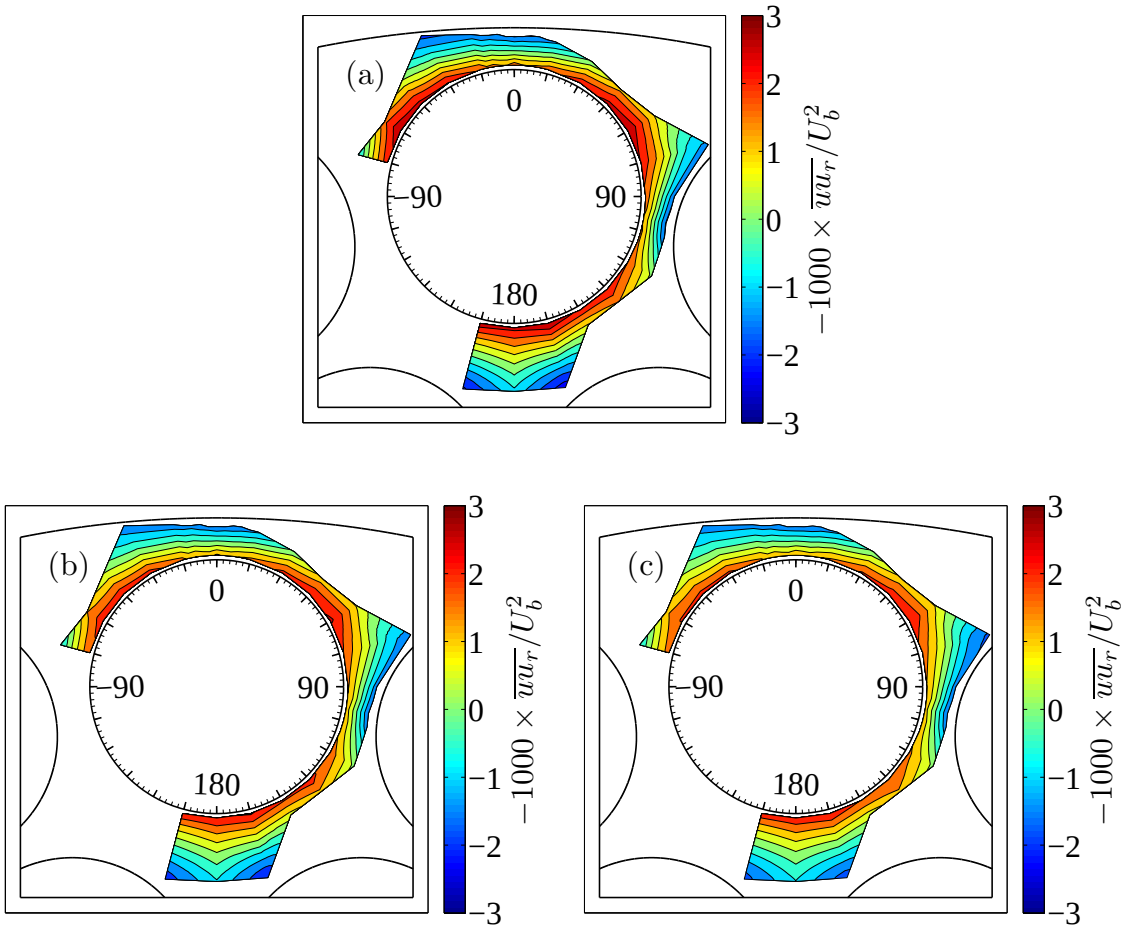

Figure 5.15: Isocontour plots of the radial Reynolds shear stresses $\overline{uu_r}$ for (a) $Re = 50,000$, (b) $Re = 100,000$, (c) $Re = 130,000$.

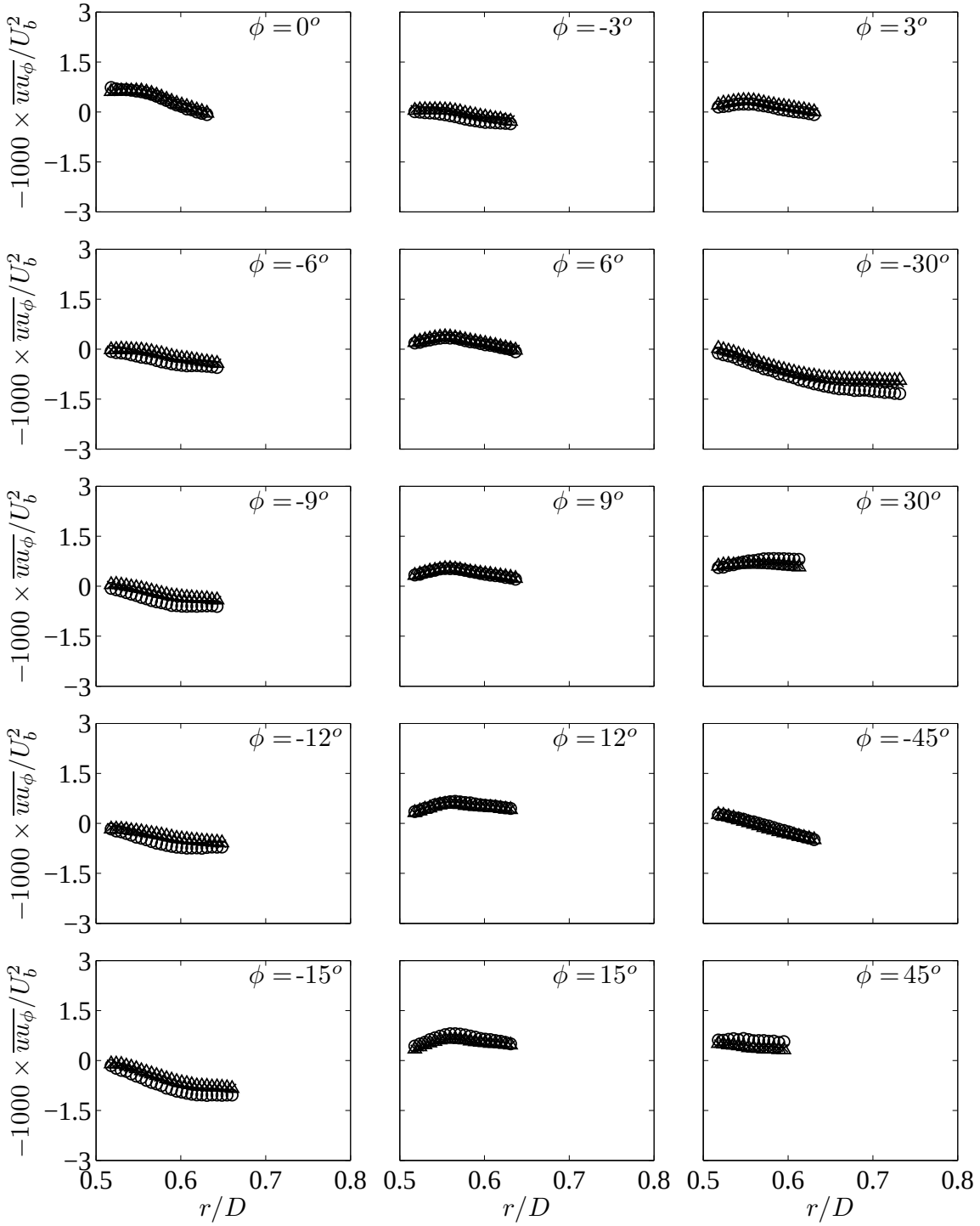

Figure 5.16: Radial profiles of the normalised azimuthal Reynolds shear stress at various azimuthal locations and for $Re = 50,000$ (○), $100,000$ (×) and $130,000$ (△).

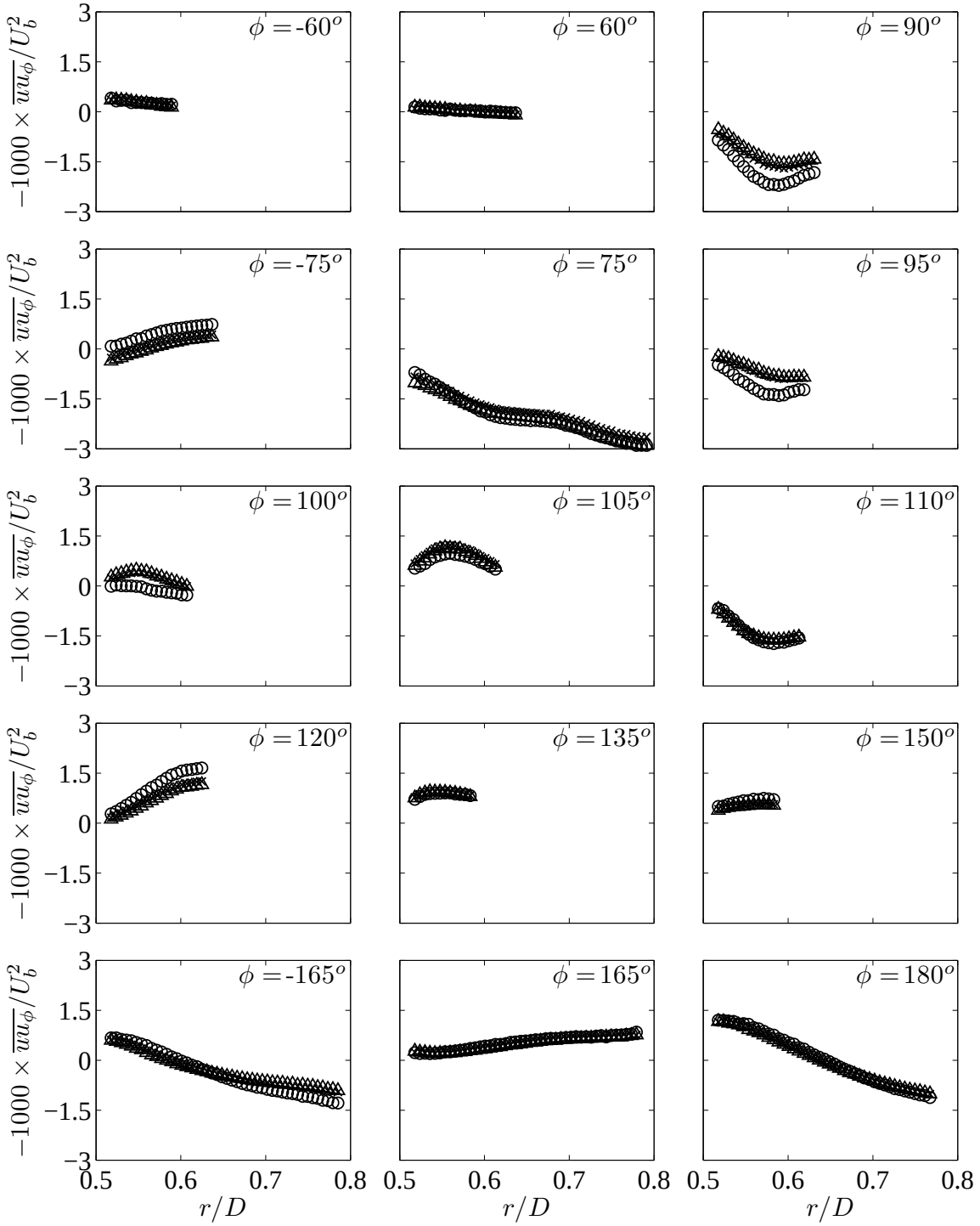

Figure 5.16 (Continued): Radial profiles of the normalised azimuthal Reynolds shear stress at various azimuthal locations and for $Re = 50,000$ (○), $100,000$ (×) and $130,000$ (△).

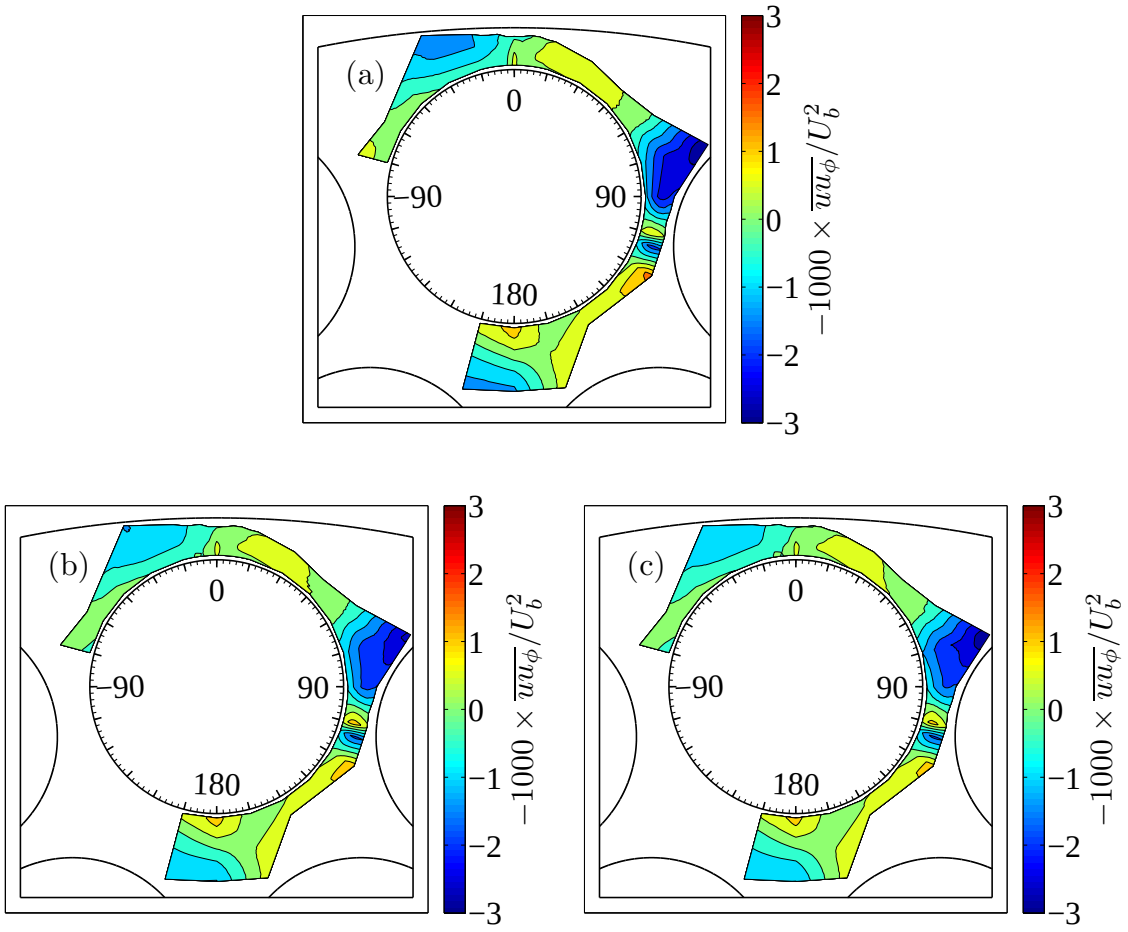

Figure 5.17: Isocontour plots of the normalised azimuthal Reynolds shear stress for (a) $Re = 50,000$, (b) $Re = 100,000$, (c) $Re = 130,000$.

5.6 Turbulent kinetic energy distribution

Figure 5.18 illustrates the radial variations of the normalised turbulent kinetic per unit mass at various azimuthal locations around the central rod. The turbulent kinetic energy was normalised with the bulk velocity squared. In all cases, the turbulent kinetic energy was highest at the measuring position that was closest to the rod surface and lowest near the subchannel midline. Similar trends were reported by Trupp and Azad [1975], who studied the structure of turbulence in a triangular array rod bundle. The normalised turbulent kinetic energy decreased measurably with increasing Reynolds number. This was true in all cases although there were few cases, mostly in the rod-wall gap regions, where the effect of Reynolds number was less noticeable. For all three Reynolds numbers, the highest turbulent kinetic energy was achieved close to the rod in the triangular open channel regions. The magnitude of the turbulent kinetic energy measured at the centre of the rod-wall gap ($\phi = 0°$) were lower than those measured at the centre of the rod-rod gap ($\phi = 105°$).

The contour maps, shown in figure 5.19, demonstrated that the turbulent kinetic energy was higher in the open flow regions and lower in the gap regions. This is consistent with the fact that turbulence production by mean shear near the rod surface was higher at locations exposed to the open flow regions than in the gap regions. The available contours indicate that the turbulent kinetic energy variation was nearly symmetric about the test section centreplane.

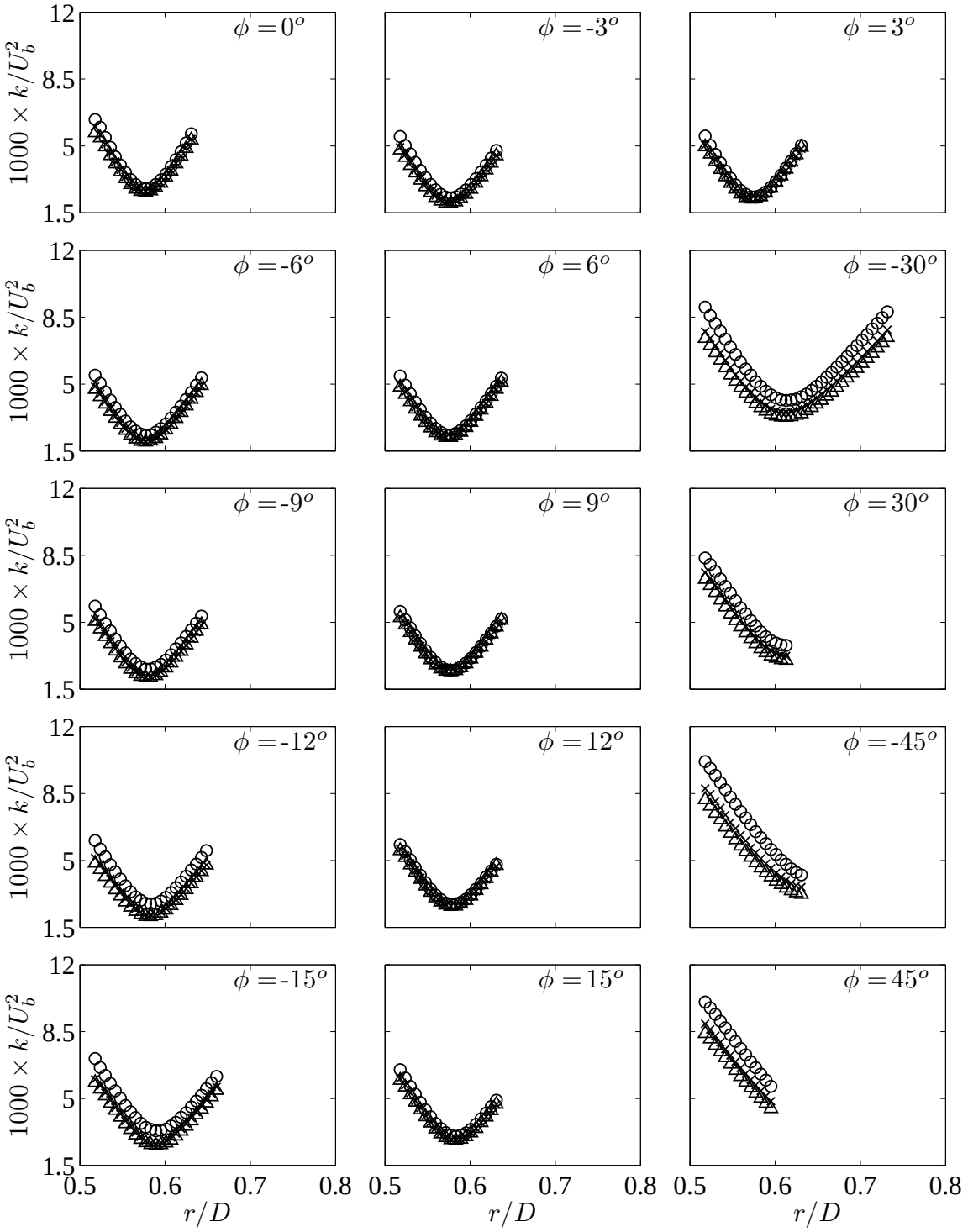

Figure 5.18: Radial profiles of the normalised turbulent kinetic energy at various azimuthal locations and for $Re = 50,000$ (○), $100,000$ (×) and $130,000$ (△).

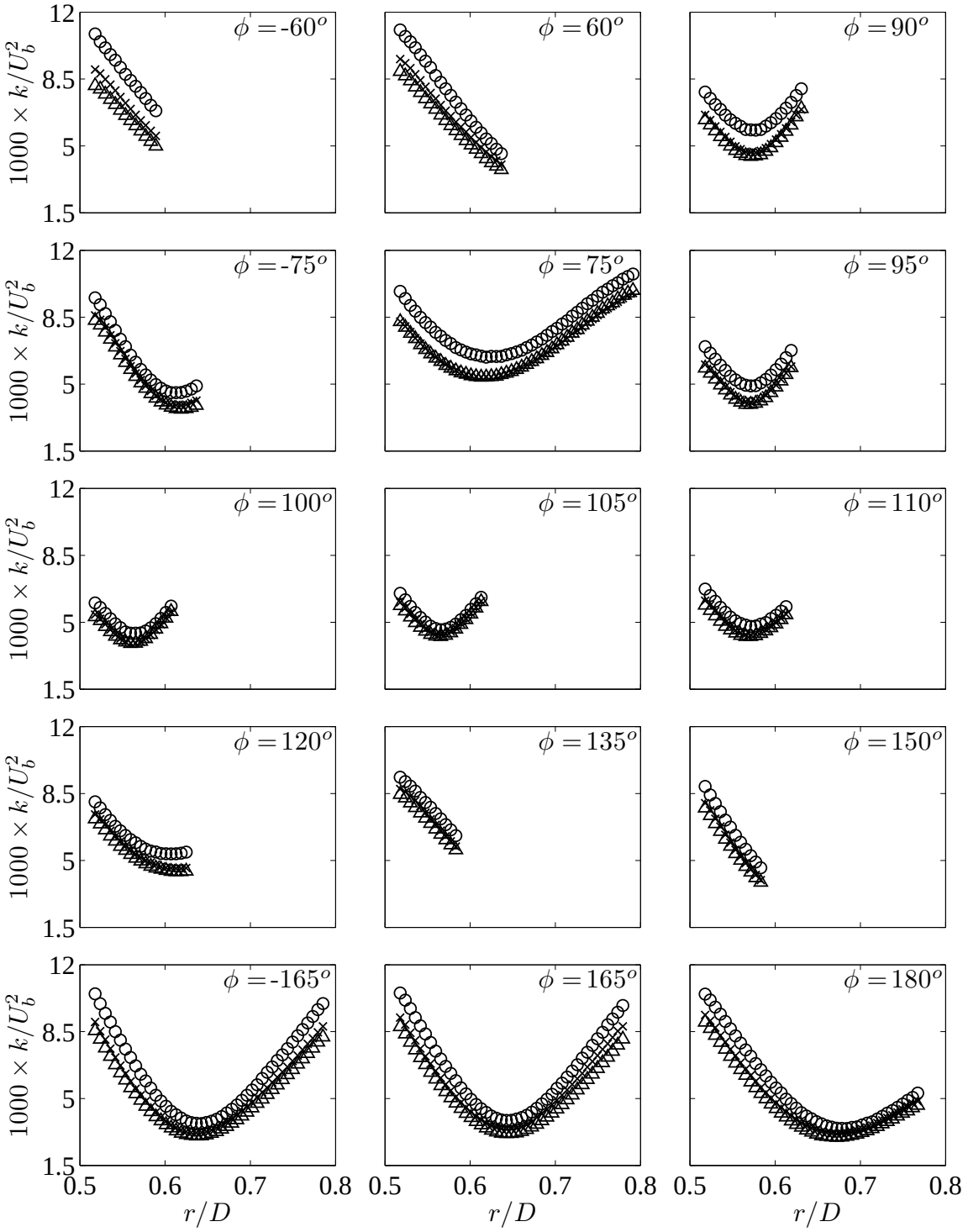

Figure 5.18 (Continued): Radial profiles of the normalised turbulent kinetic energy at various azimuthal locations and for $Re = 50,000$ (○), $100,000$ (×) and $130,000$ (△).

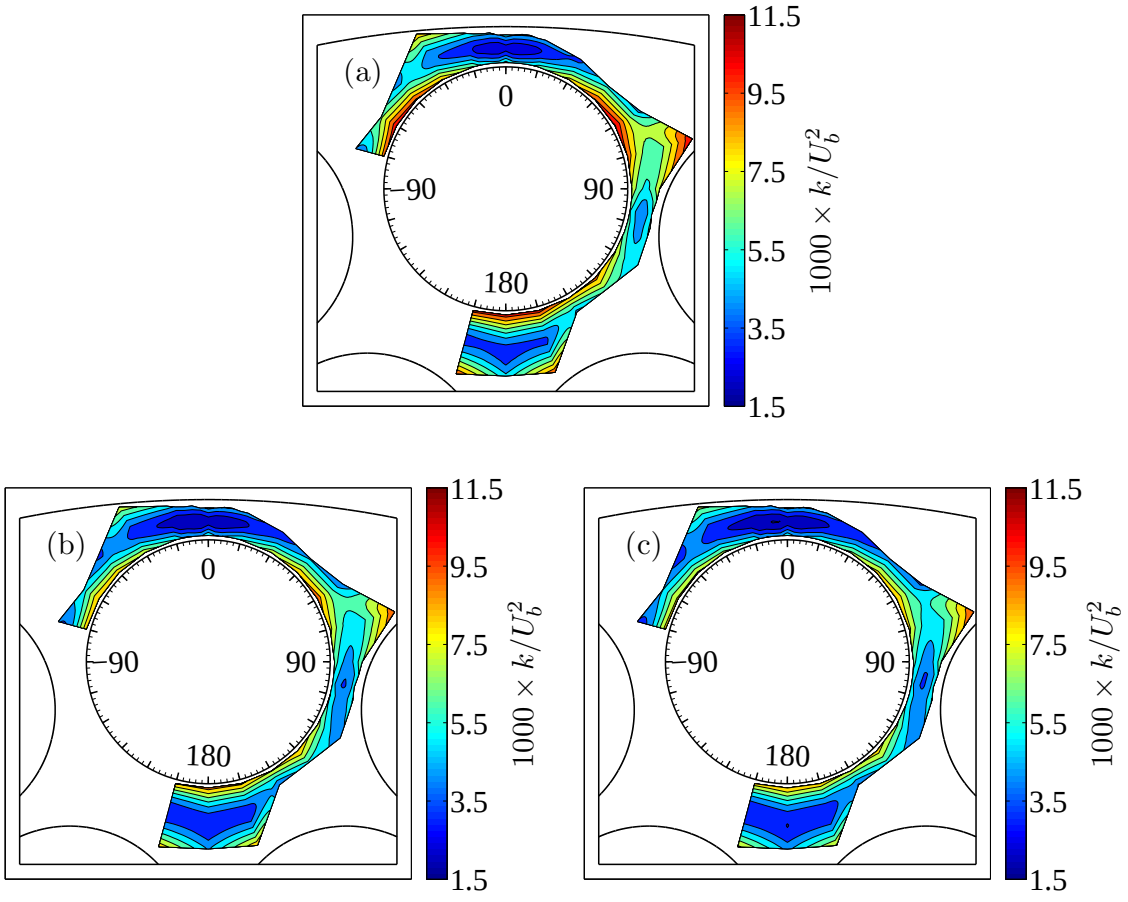

Figure 5.19: Isocontour plots of the normalised turbulent kinetic energy for (a) $Re = 50,000$, (b) $Re = 100,000$, (c) $Re = 130,000$.

5.7 Reynolds stress tensor anisotropy

The main Reynolds stress anisotropies of interest were defined as

$$m_u = \frac{\overline{u^2}}{2k} - \frac{1}{3} \tag{5.1}$$

$$m_r = \frac{\overline{u_r^2}}{2k} - \frac{1}{3} \tag{5.2}$$

$$m_\phi = \frac{\overline{u_\phi^2}}{2k} - \frac{1}{3} \tag{5.3}$$

$$m_{ur} = \frac{\overline{uu_r}}{2k} \tag{5.4}$$

In isotropic flow, all anisotropies would vanish. A few representative radial profiles of these anisotropies are presented in figures 5.20, 5.21, 5.22 and 5.23. The general trends of the anisotropies at other azimuthal locations were qualitatively similar to those shown in the figures.

In all cases, m_u remained positive, while decreasing with increasing distance from the wall to reached local minima near the midlines of the subchannels. In general, the values of m_u in the open channels were comparable to those in the rod-rod gap regions and slightly larger than those in the rod-wall gap region. Furthermore, m_u seemed to increase with increasing Reynolds number at rates that depended on the radial and azimuthal positions. Both m_r and m_ϕ were negative in the entire range of measurements, with m_r being, in general, the most anisotropic of the two. Like m_u, the magnitudes of m_r and m_ϕ decreased from the rod surface toward the subchannel midline. As the Reynolds number increased, the magnitudes of m_r and m_ϕ generally decreased towards zero. When compared to their corresponding profiles in the rod-wall gap, the distributions of m_r in the rod-rod gap could not be entirely explained as they appeared to be flatter across the radial distance. Coherent vortices alone could not have been responsible for this because the profiles of m_r in the open channel show similar trends as those for the rod-wall gap. Generally the magnitudes of m_r and m_ϕ were larger than the magnitude of m_u, which was to be expected, as $\overline{u^2}$ received most

of the energy of the turbulent flow as opposed to $\overline{u_r^2}$ and $\overline{u_\phi^2}$. Radial profiles of m_{ur} were nearly anti-symmetric about the subchannel midline, maintaining a sign that was opposite to the sign of the radial derivative of the mean axial velocity, in conformity with gradient transport. The magnitude of m_{ur} was not affected by Reynolds number. When all results are viewed as a whole, one may observe that the Reynolds stress tensor anisotropy was considerable in the entire range of measurements. It decreased from the wall towards the midline and increased with increasing Reynolds number. The radial distributions of the anisotropy tensor highlight the complex structure of turbulence in rod bundles and its difference from flows in circular pipes.

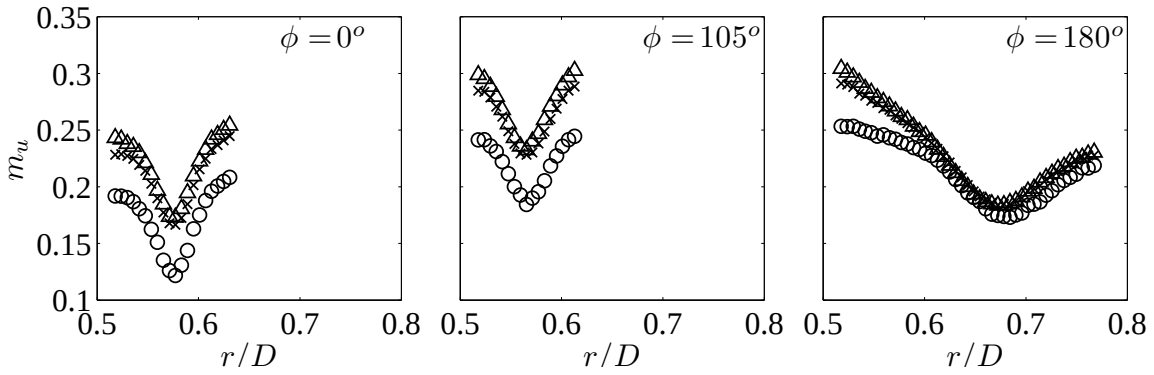

Figure 5.20: Representative radial profiles of the axial Reynolds stress anisotropy for $Re = 50,000$ (○), $100,000$ (×) and $130,000$ (△).

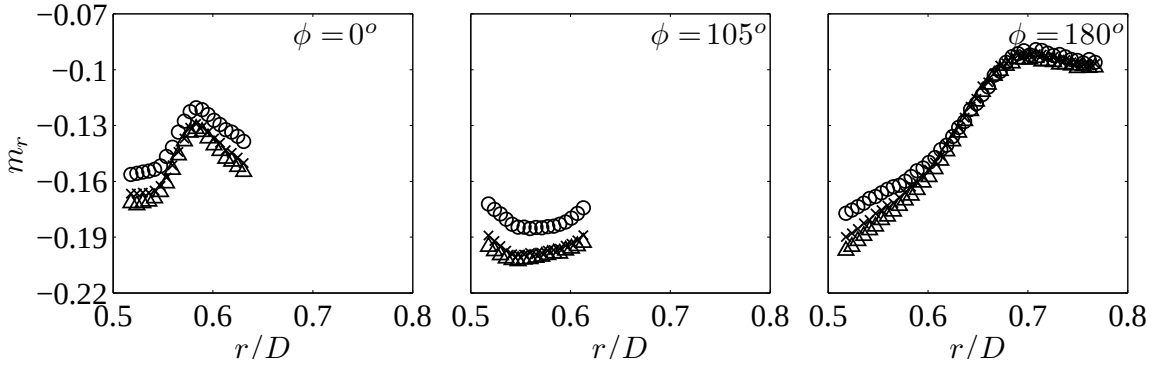

Figure 5.21: Representative radial profiles of the radial Reynolds stress anisotropy for $Re = 50,000$ (○), $100,000$ (×) and $130,000$ (△).

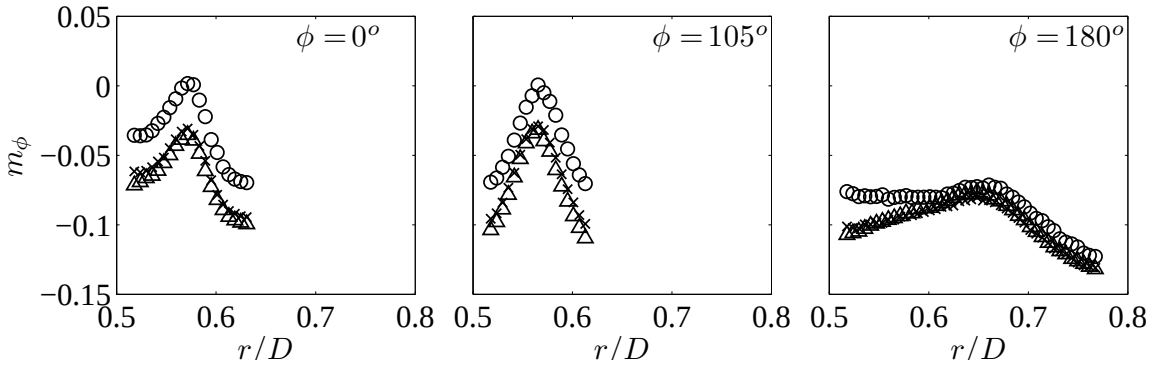

Figure 5.22: Representative radial profiles of the azimuthal Reynolds stress anisotropy for $Re = 50,000$ (○), $100,000$ (×) and $130,000$ (△).

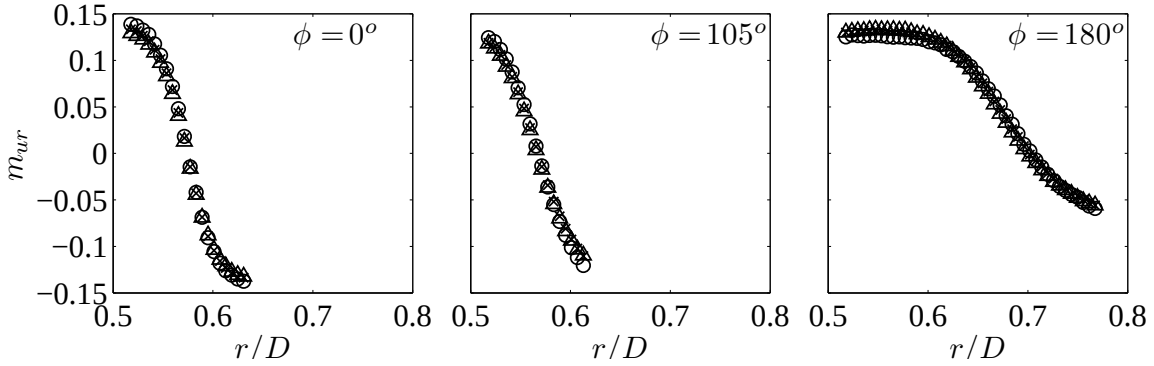

Figure 5.23: Representative radial profiles of the axial Reynolds stress anisotropy for $Re = 50,000$ (○), $100,000$ (×) and $130,000$ (△).

5.8 Turbulent length scales

5.8.1 Integral length scale

Presented in figures 5.24, 5.26 and 5.28 are the radial variations of the streamwise Eulerian integral length scales of the axial, radial and azimuthal velocity fluctuations, respectively. All integral length scales were normalised by the rod diameter. Isocontours of these scales in the parts of the subchannels around the central rod that could be accessed by our probe are shown in figures 5.25, 5.27 and 5.29.

In all cases, the streamwise integral length scale of the axial velocity fluctuations L_u was largest and increased with increasing radial distance from the rod, in conformity with relevant literature. L_u was higher in the open flow regions and lower in the

small gaps. Nevertheless, L_u at the extremities of the narrow gaps were comparable to those measured in the open channels, as illustrated by the contour maps. For the most part, the Reynolds number effect on L_u/D was weak but it appeared that L_u/D increased slightly with increasing Reynolds number.

In the open channels, the radial fluctuation scale L_r increased away from the rod surface. This was not the case, however, in the narrow gap regions, where L_r was lowest near the subchannel midline. At all three Reynolds numbers studied, L_r increased from the narrow gaps toward the open channels as shown in the contour maps. The effect of Reynolds number on L_r/D was more noticeable in the open flow regions than in the gap regions and, generally, L_r/D was higher at larger Reynolds number.

The radial distributions of L_ϕ showed that this scale increased away from the rod, reached maxima, then decreased, at least in the cases for which profiles extended beyond the subchannel midline. L_ϕ was largest in the narrow gaps as illustrated in the contour maps, which is attributed to the gap vortex street. The effect of Reynolds number on L_ϕ in those regions was not measurable. On the other hand, a weak but noticeable increase of L_ϕ as the Reynolds number became larger was observed in the open parts of the subchannels.

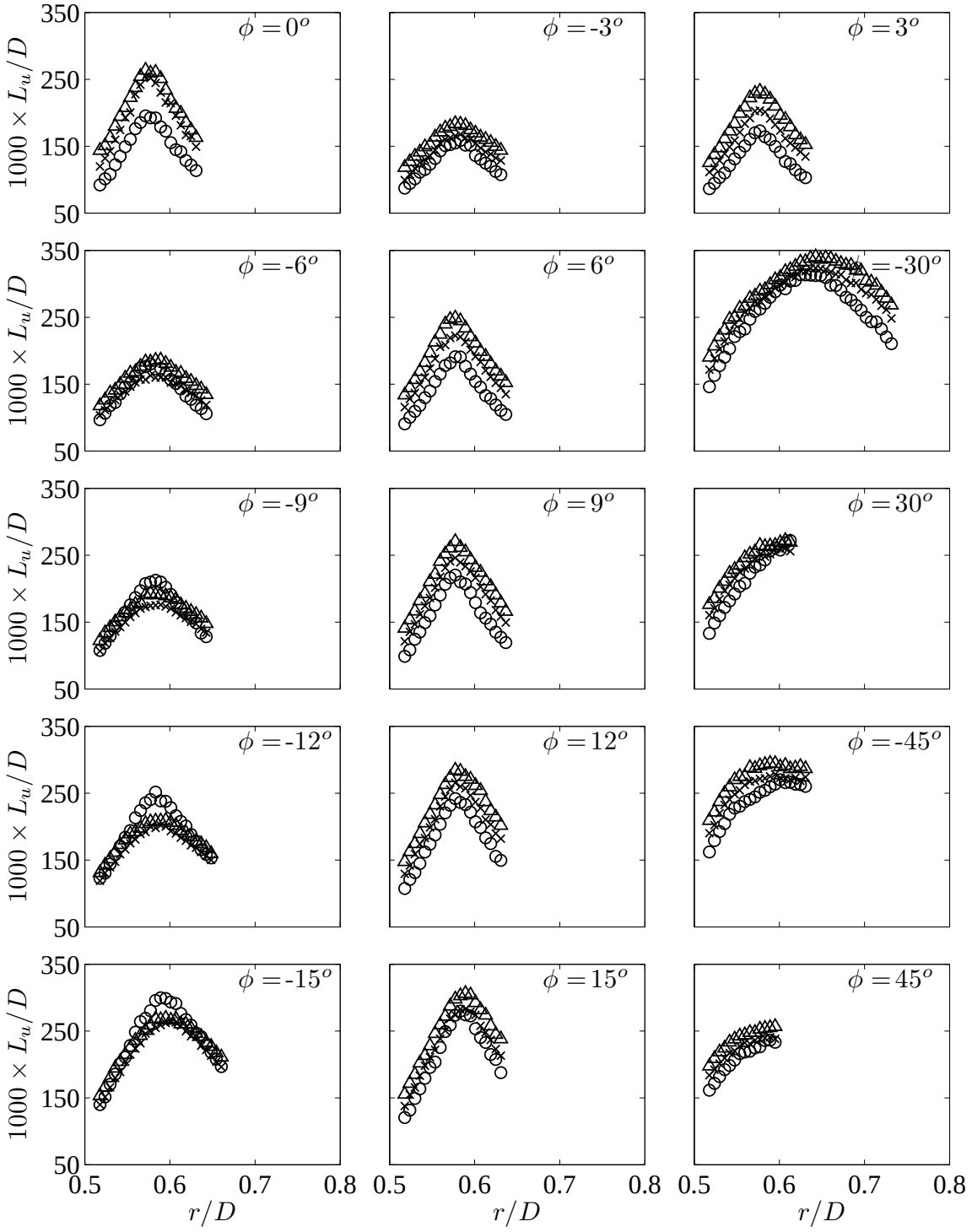

Figure 5.24: Radial profiles of the streamwise Eulerian integral length scale of the axial velocity fluctuations at various azimuthal locations and for $Re = 50,000$ ($\bigcirc$), $100,000$ ($\times$) and $130,000$ ($\triangle$).

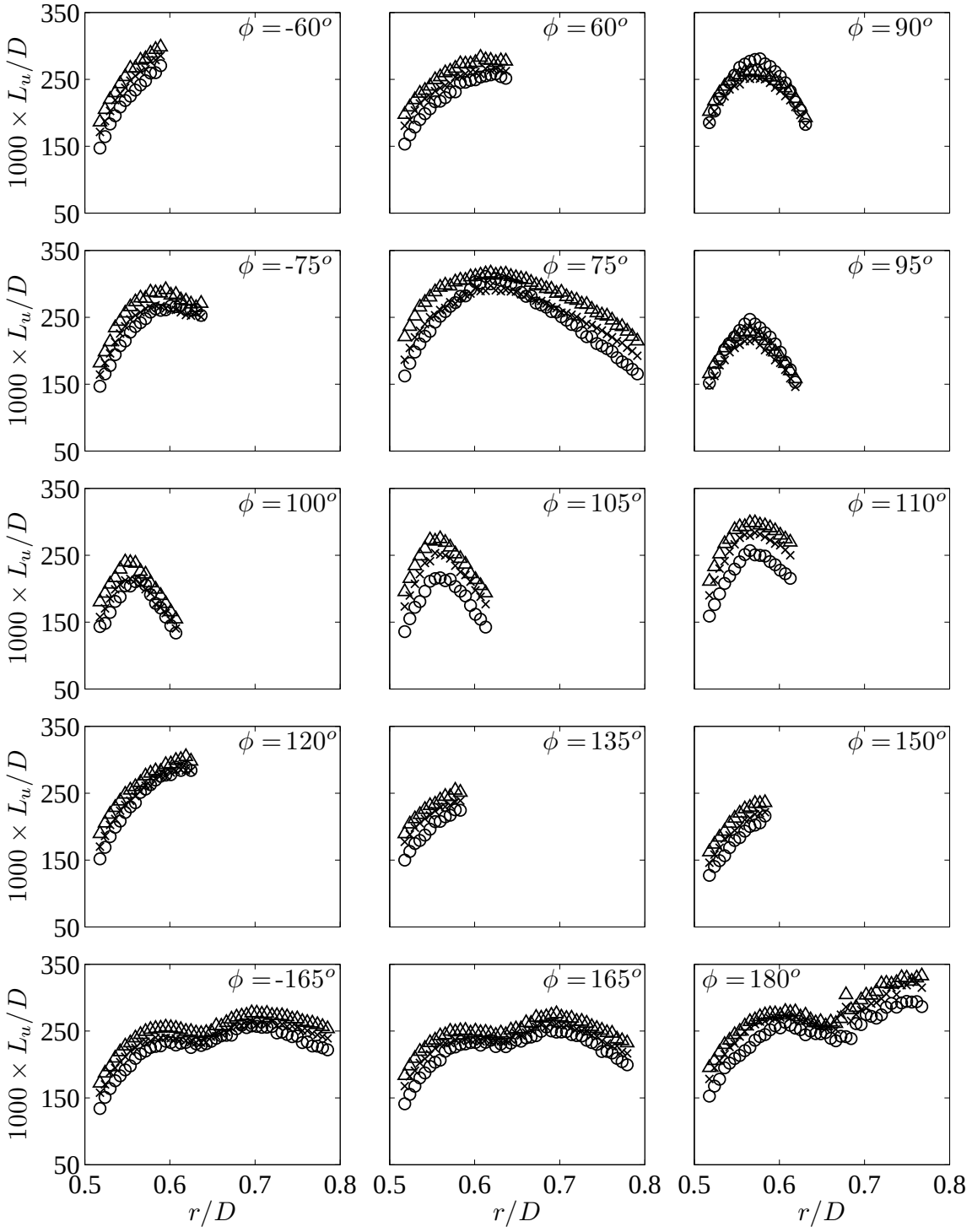

Figure 5.24 (Continued): Radial profiles of the streamwise Eulerian integral length scale of the axial velocity fluctuations at various azimuthal locations and for $Re = 50,000$ ($\bigcirc$), $100,000$ ($\times$) and $130,000$ ($\triangle$).

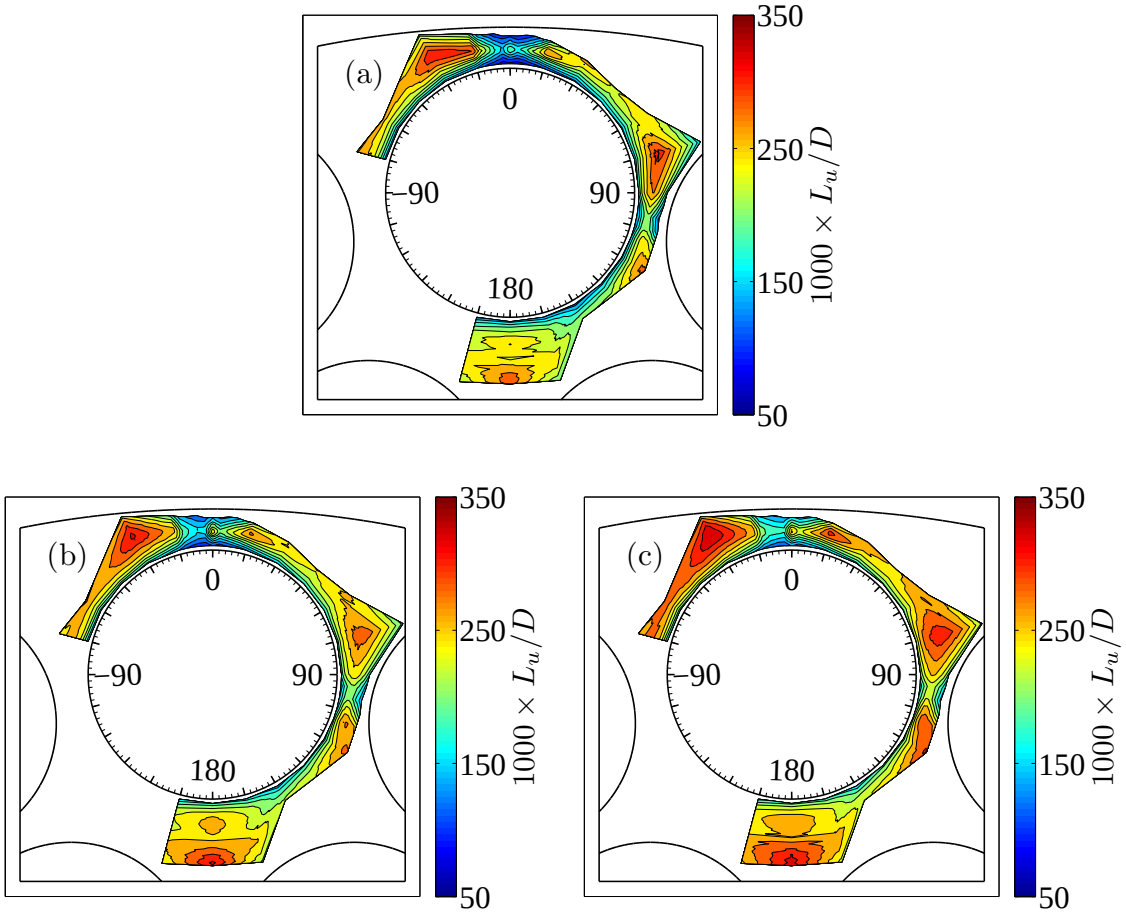

Figure 5.25: Isocontour plots of the normalised streamwise Eulerian integral length scale of the axial velocity fluctuations for (a) $Re = 50,000$, (b) $Re = 100,000$, (c) $Re = 130,000$.

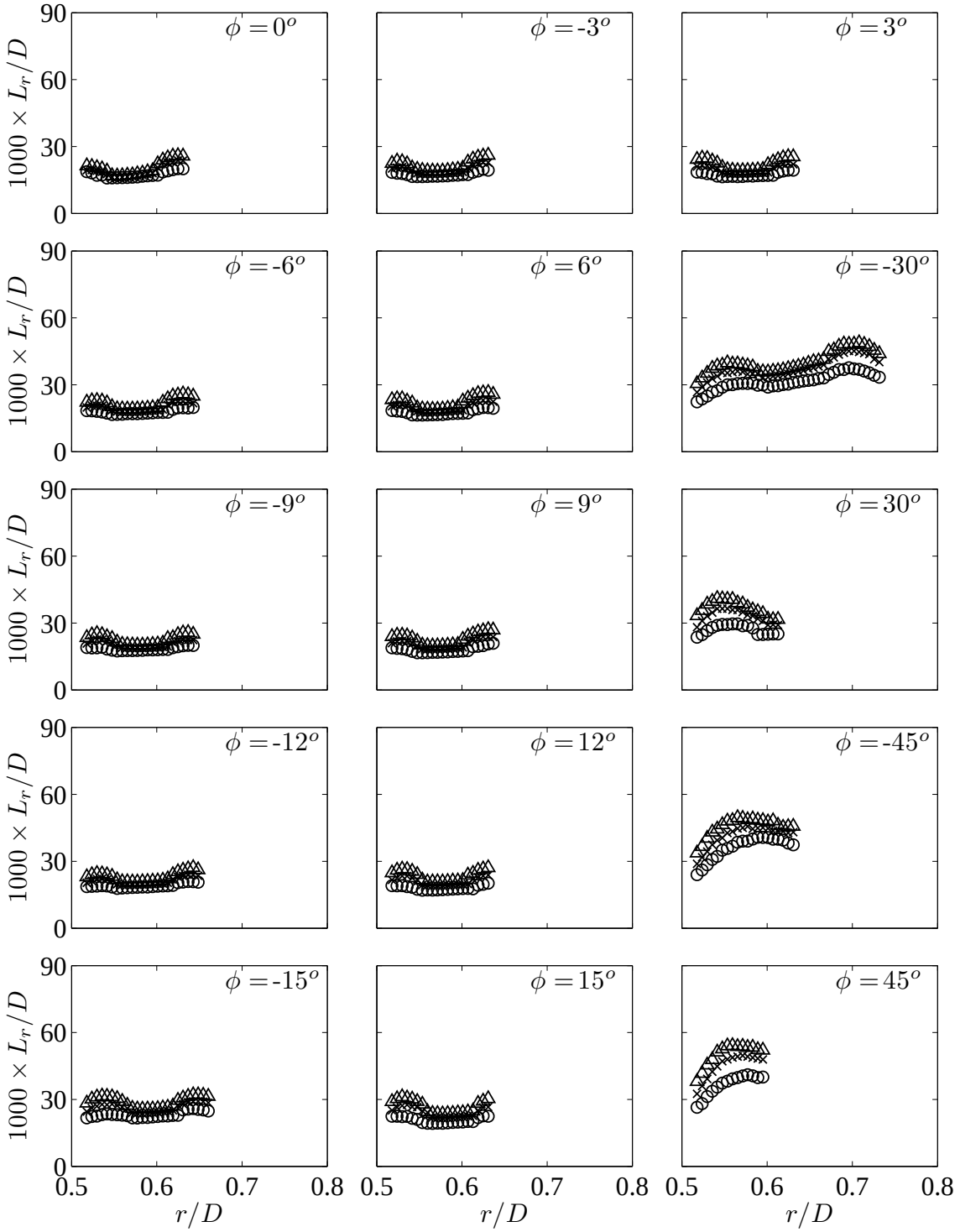

Figure 5.26: Radial profiles of the streamwise Eulerian integral length scale of the radial velocity fluctuations at various azimuthal locations and for $Re = 50,000$ ($\bigcirc$), $100,000$ ($\times$) and $130,000$ ($\triangle$).

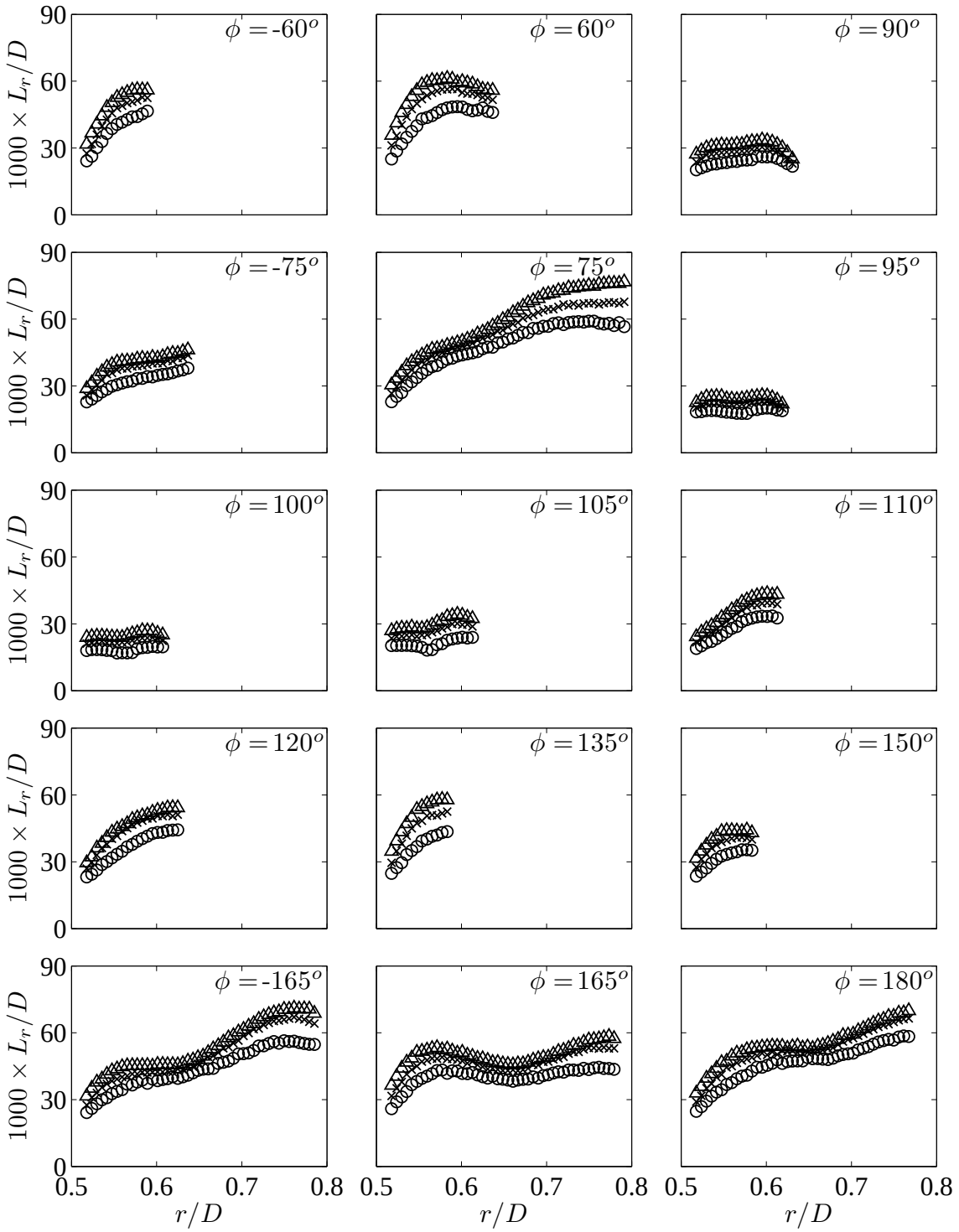

Figure 5.26 (Continued): Radial profiles of the streamwise Eulerian integral length scale of the radial velocity fluctuations at various azimuthal locations and for $Re = 50,000$ ($\bigcirc$), $100,000$ ($\times$) and $130,000$ ($\triangle$).

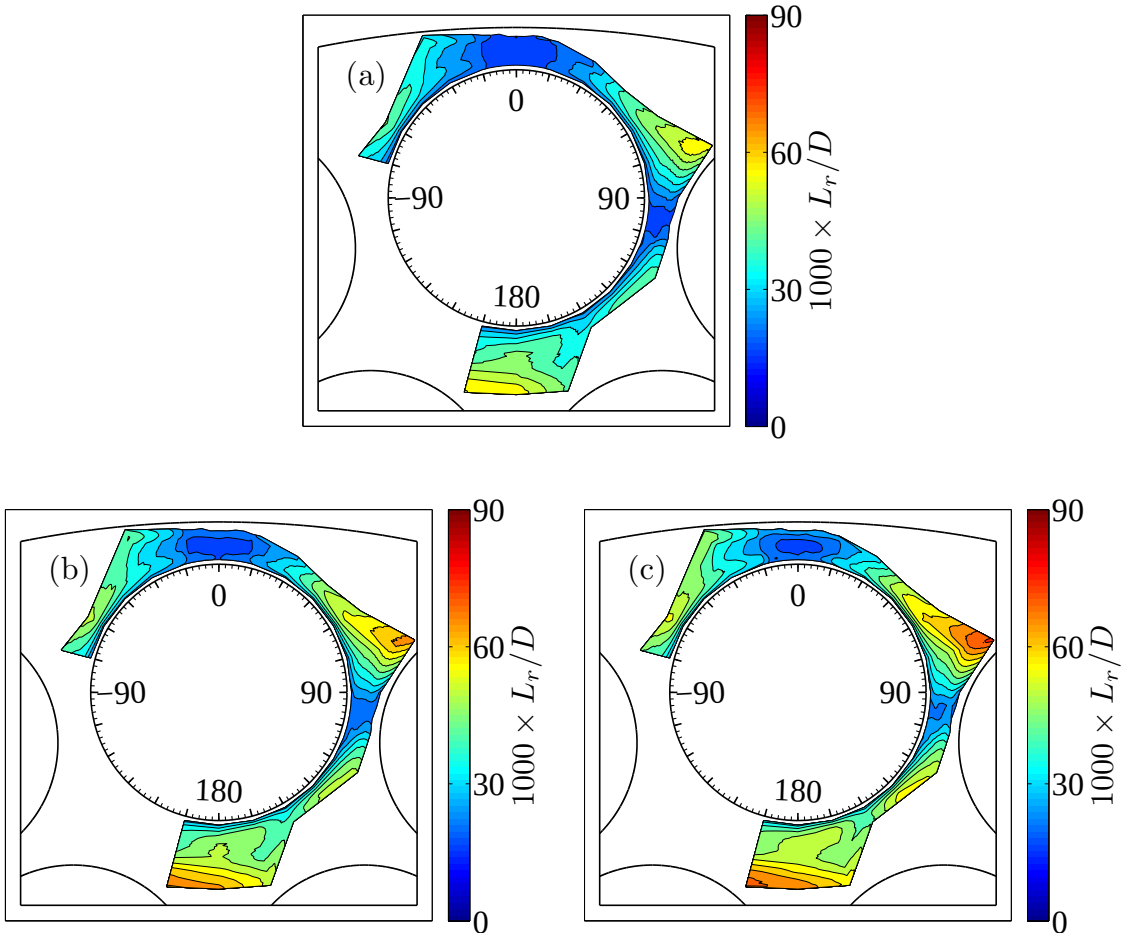

Figure 5.27: Isocontour plots of the normalised streamwise Eulerian integral length scale of the radial velocity fluctuations for (a) $Re = 50,000$, (b) $Re = 100,000$, (c) $Re = 130,000$.

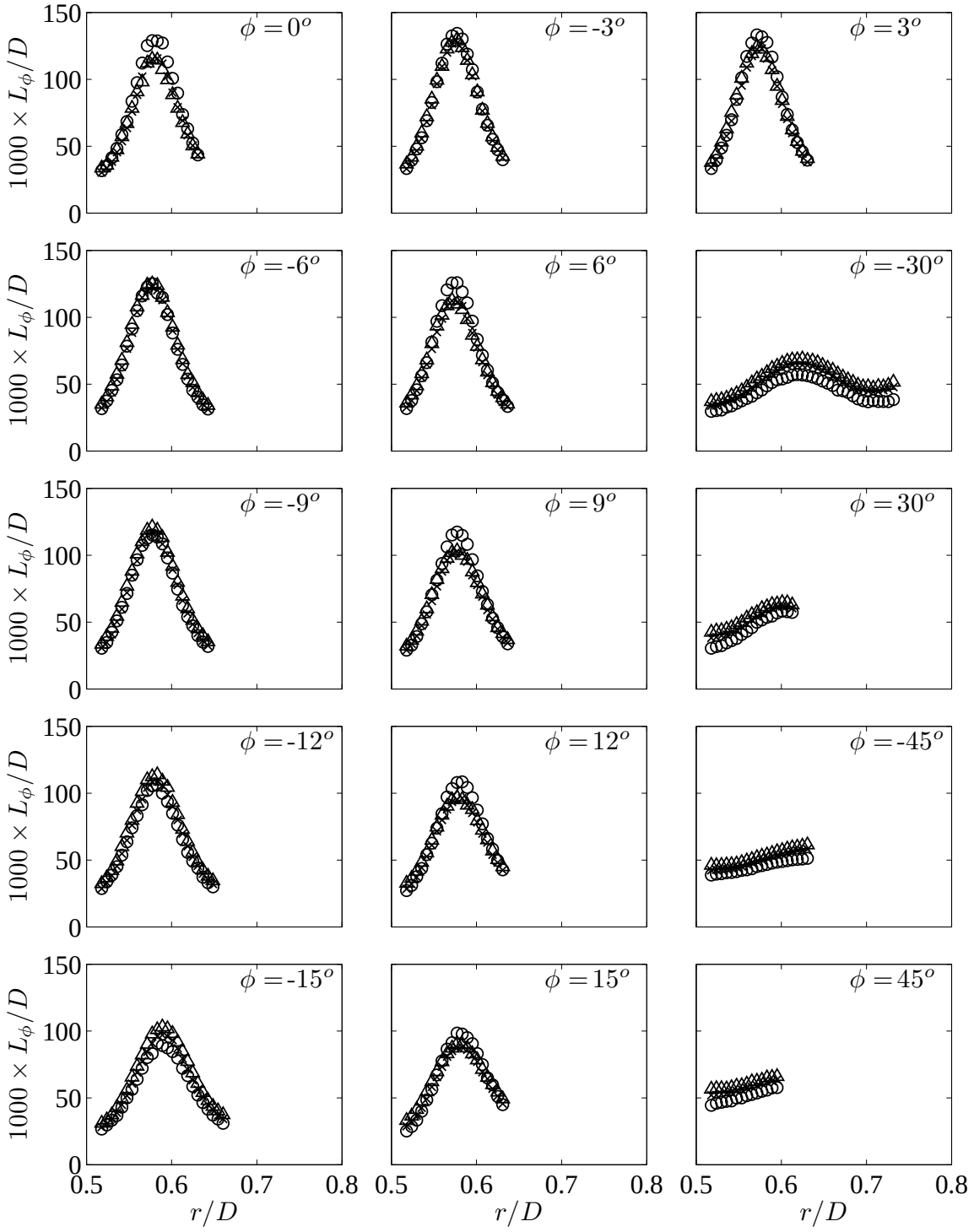

Figure 5.28: Radial profiles of the streamwise Eulerian integral length scale of the azimuthal velocity fluctuations at various azimuthal locations and for $Re = 50,000$ ($\bigcirc$), $100,000$ ($\times$) and $130,000$ ($\triangle$).

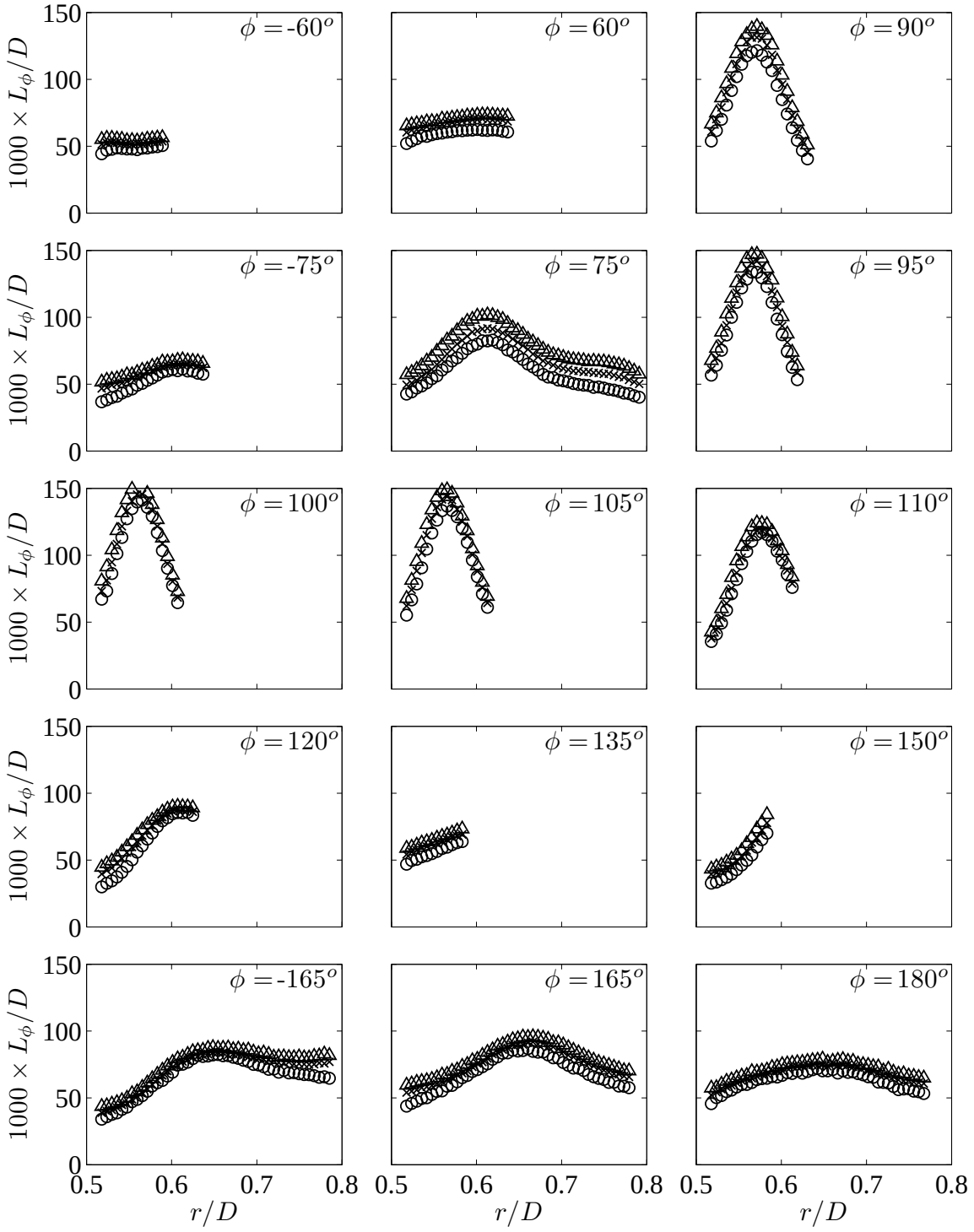

Figure 5.28 (Continued): Radial profiles of the streamwise Eulerian integral length scale of the azimuthal velocity fluctuations at various azimuthal locations and for $Re = 50,000$ (○), $100,000$ (×) and $130,000$ (△).

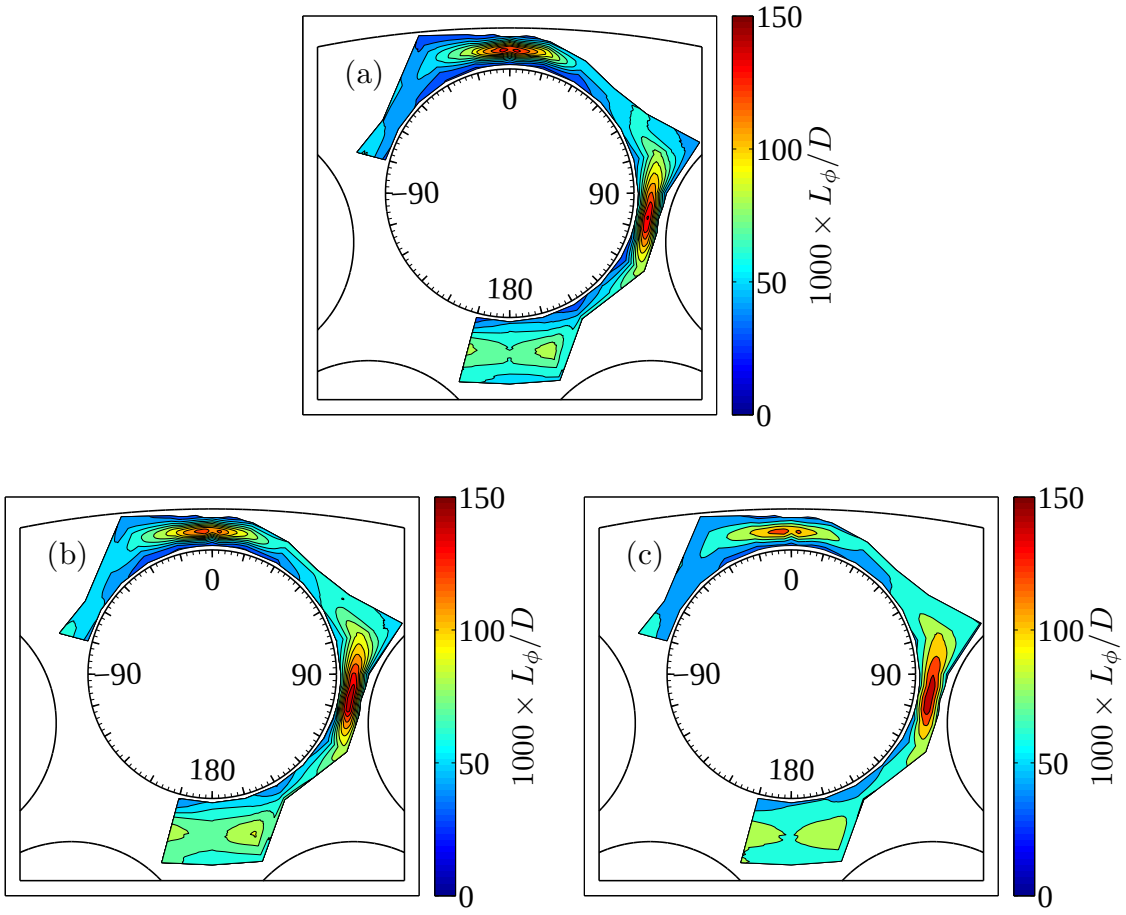

Figure 5.29: Isocontour plots of the normalised streamwise Eulerian integral length scale of the azimuthal velocity fluctuations for (a) $Re = 50,000$, (b) $Re = 100,000$, (c) $Re = 130,000$.

5.8.2 Taylor microscale

Radial profiles of the normalized streamwise Taylor microscale λ/D are presented in figure 5.31. Generally, the magnitude of the streamwise Taylor microscale λ was larger in the open channels than in the narrow gaps and increased away from the rod as a result of a lower velocity gradient near the midlines of the subchannels. The values of λ in the rod-wall gap were comparable to values found in the rod-rod gap. When all the results are considered, the range of λ was from 2.2 mm to 4.8 mm, 1.9 mm to 4.4 mm and 1.8 mm to 4.2 mm at Re = 50,000, 100,000 and 130,000, respectively. These are in conformity with the expectation that λ would be lower at larger Reynolds number. In most cases λ decreased more significantly for Re changing from 50,000 to 100,000 than from 100,000 to 130,000. Figure 5.32 shows that the contours of λ bulged toward the narrow gaps, in a manner similar to the contours of the streamwise integral length scales of the axial and radial velocity fluctuations.

A few representative radial profiles of the turbulent Reynolds number R_λ are presented in figure 5.30. The general trends of R_λ at azimuthal locations not presented in this figure were qualitatively similar to those shown in the figure. As expected, R_λ became larger with increasing bulk Reynolds number. Generally, R_λ was largest in the open flow region and increased away from the wall, reached local maxima, decreased to local minima near the midlines of the subchannels, increased again to reach second local maxima, and then decreased. This trend was mostly true for symmetrical profiles such as those found in the narrow gaps.

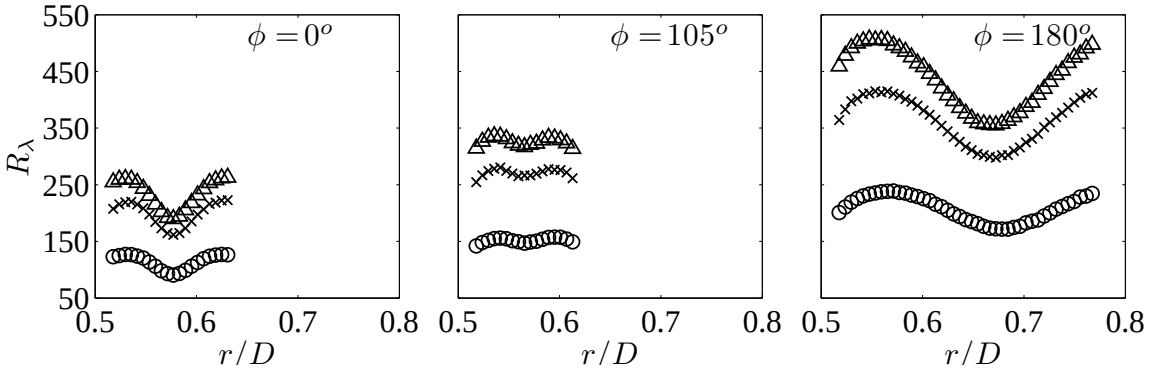

Figure 5.30: Radial profiles of the turbulent Reynolds number for $Re = 50,000$ (○), $100,000$ (×) and $130,000$ (△).

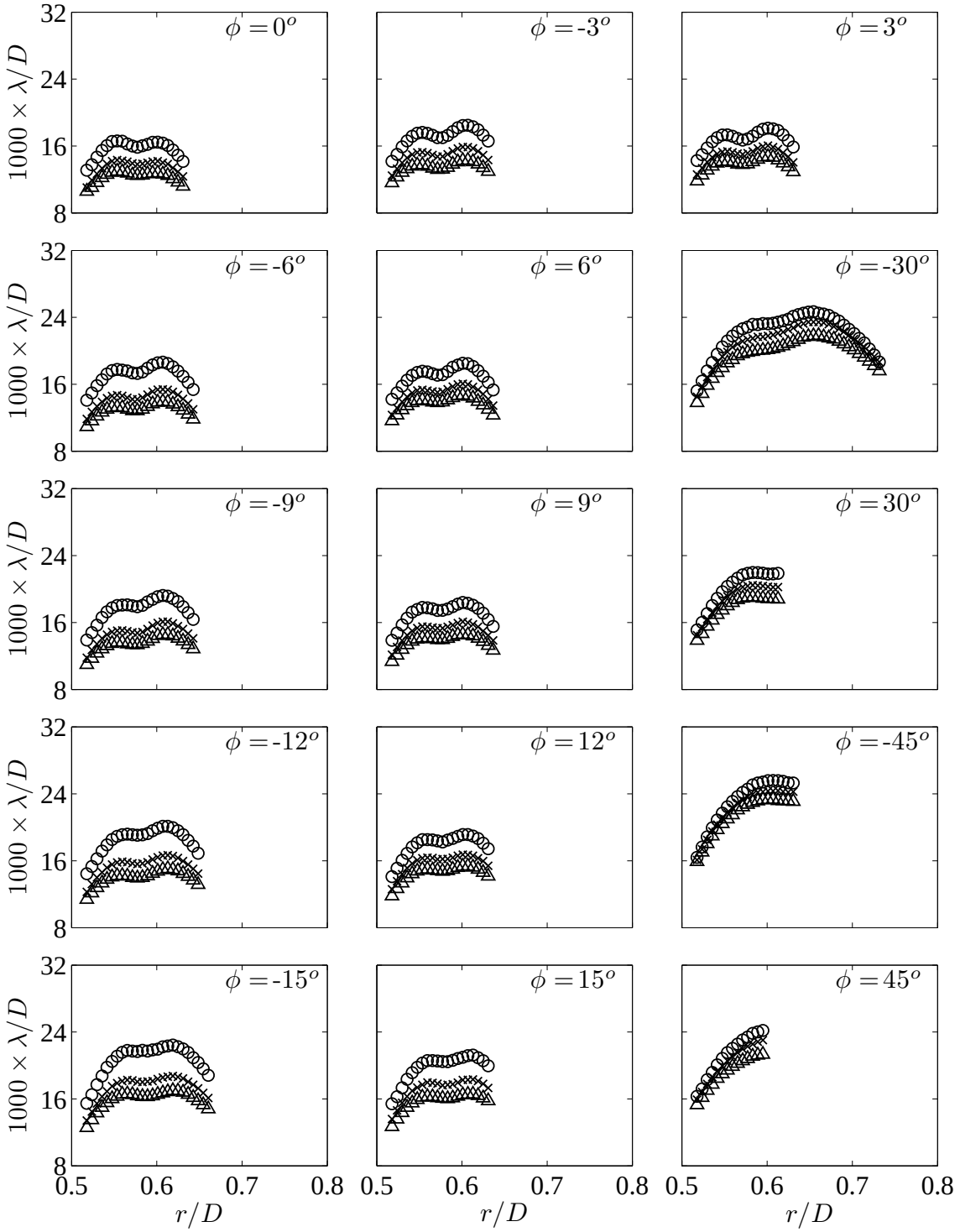

Figure 5.31: Radial profiles of the streamwise Taylor microscale at various azimuthal locations and for $Re = 50,000$ ($\bigcirc$), $100,000$ ($\times$) and $130,000$ ($\triangle$).

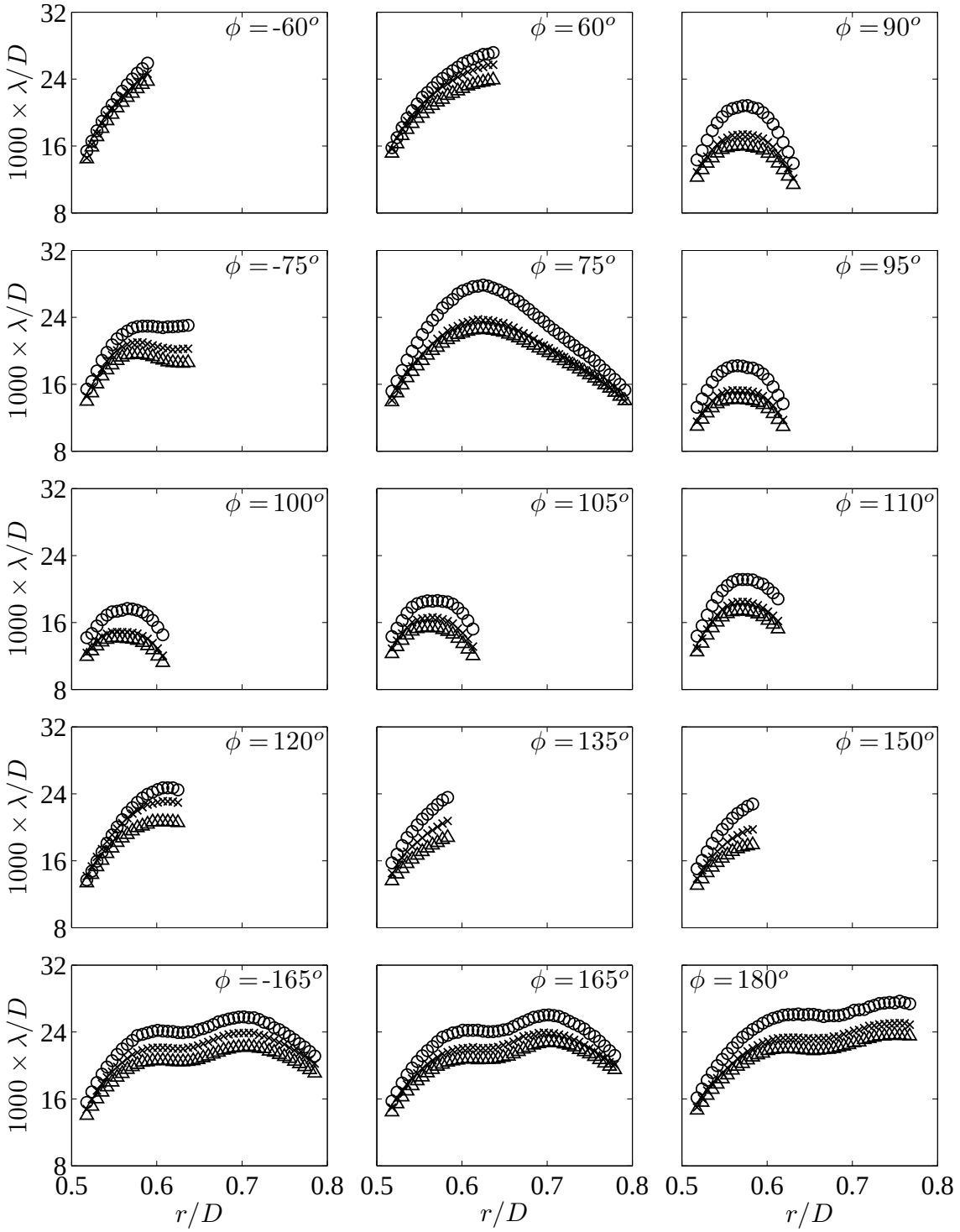

Figure 5.31 (Continued): Radial profiles of the streamwise Taylor microscale at various azimuthal locations and for $Re = 50,000$ (○), $100,000$ (×) and $130,000$ (△).

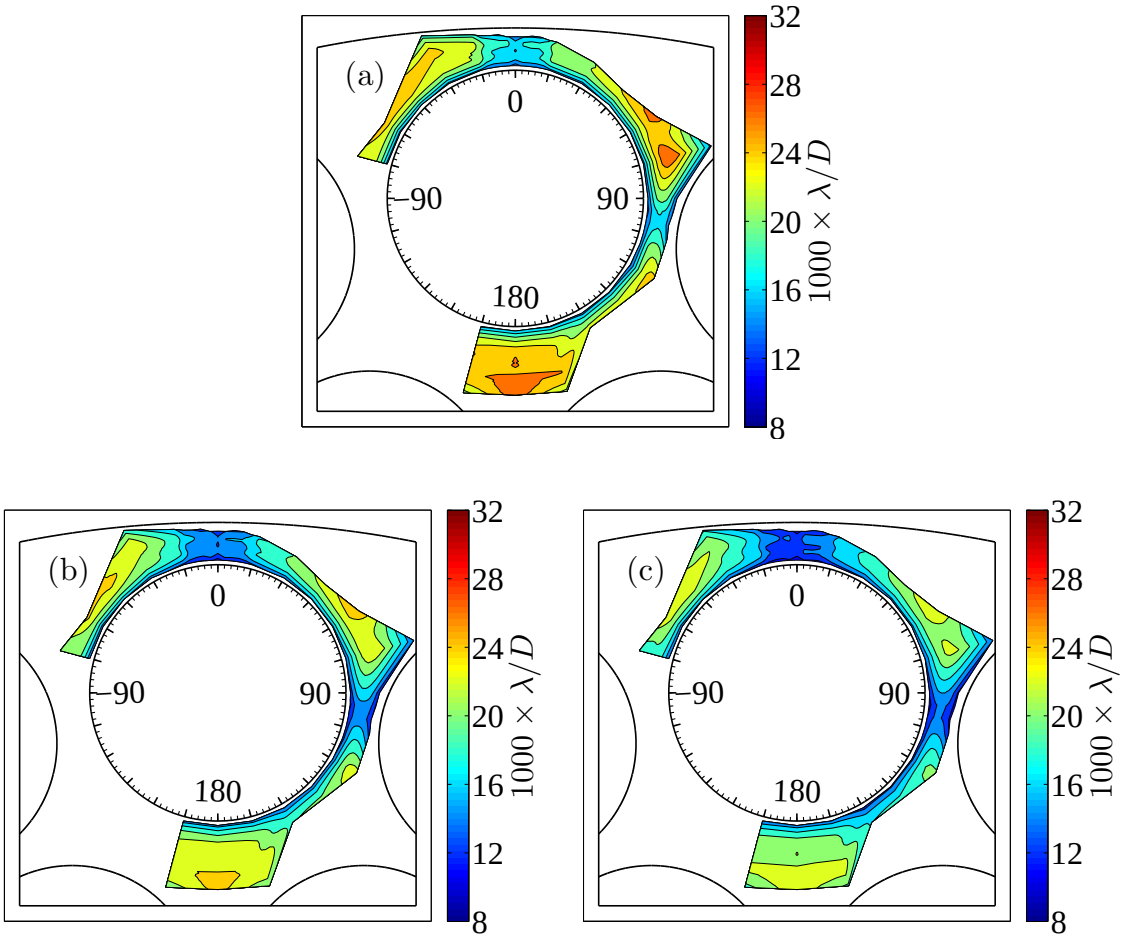

Figure 5.32: Isocontour plots of the streamwise Taylor microscale for (a) $Re = 50,000$, (b) $Re = 100,000$, (c) $Re = 130,000$.

5.8.3 Kolmogorov microscale

Representative radial profiles of the Kolmogorov microscale η normalised by the rod diameter are shown in figure 5.34. η increased away from the rod, reached local maxima, then decreased, at least in the cases where the radial distance of the measurements extended beyond the midline of the subchannel. In all cases, η decreased with increasing Reynolds number in accordance with the fact that the rate of turbulent energy dissipation was higher at larger Reynolds numbers. The Reynolds number effect on η appeared to be stronger in the range of Re from 50,000 to 100,000 than that from 100,000 to 130,000. Quantitatively, when taking the results as a whole, the magnitude of η ranged from 0.101 mm to 0.142 mm, 0.065 mm to 0.093 mm, and 0.057 mm to 0.075 mm at Re = 50,000, 100,000 and 130,000, respectively.

Unlike the other turbulence length scales, η did not vary appreciably with the subchannel size, although it tended to be a little larger in the larger subchannels compared to values in the narrow gaps, as illustrated in the contours. The contours of η also appeared to be nearly symmetric about the centreplane of the test section.

A few representative radial profiles of the isotropic dissipation rate of the kinetic energy ϵ are shown in figure 5.33. The general trends of ϵ not presented were qualitatively similar to those shown in this figure. As expected, ϵ was fastest at the closest measurement location to the wall where the conversion of the turbulent kinetic energy into thermal internal energy by viscous stresses was more effective because the magnitudes of the Kolmogorov microscale in that region were smallest.

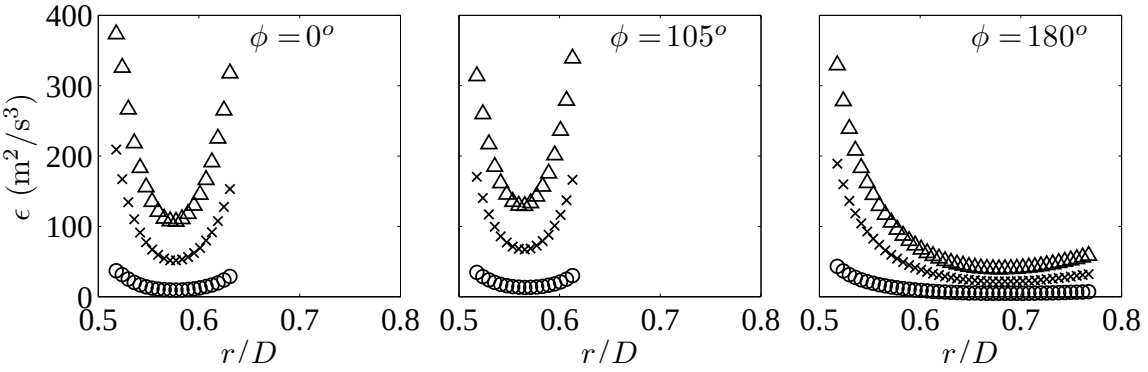

Figure 5.33: Radial profiles of the dissipation rate for $Re = 50,000$ ($\bigcirc$), $100,000$ ($\times$) and $130,000$ ($\triangle$).

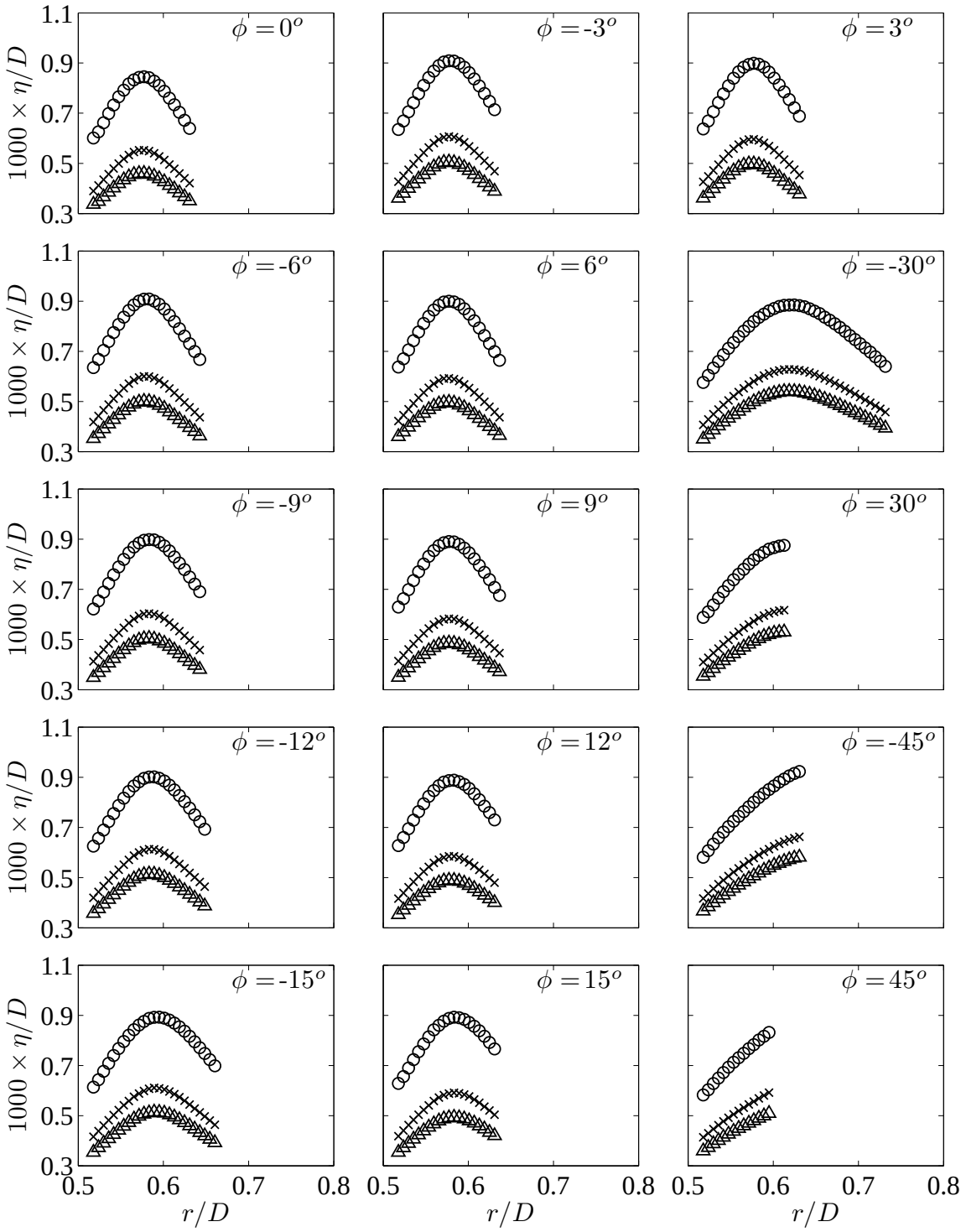

Figure 5.34: Radial profiles of the Kolmogorov microscale at various azimuthal locations and for $Re = 50,000$ (○), $100,000$ (×) and $130,000$ (△).

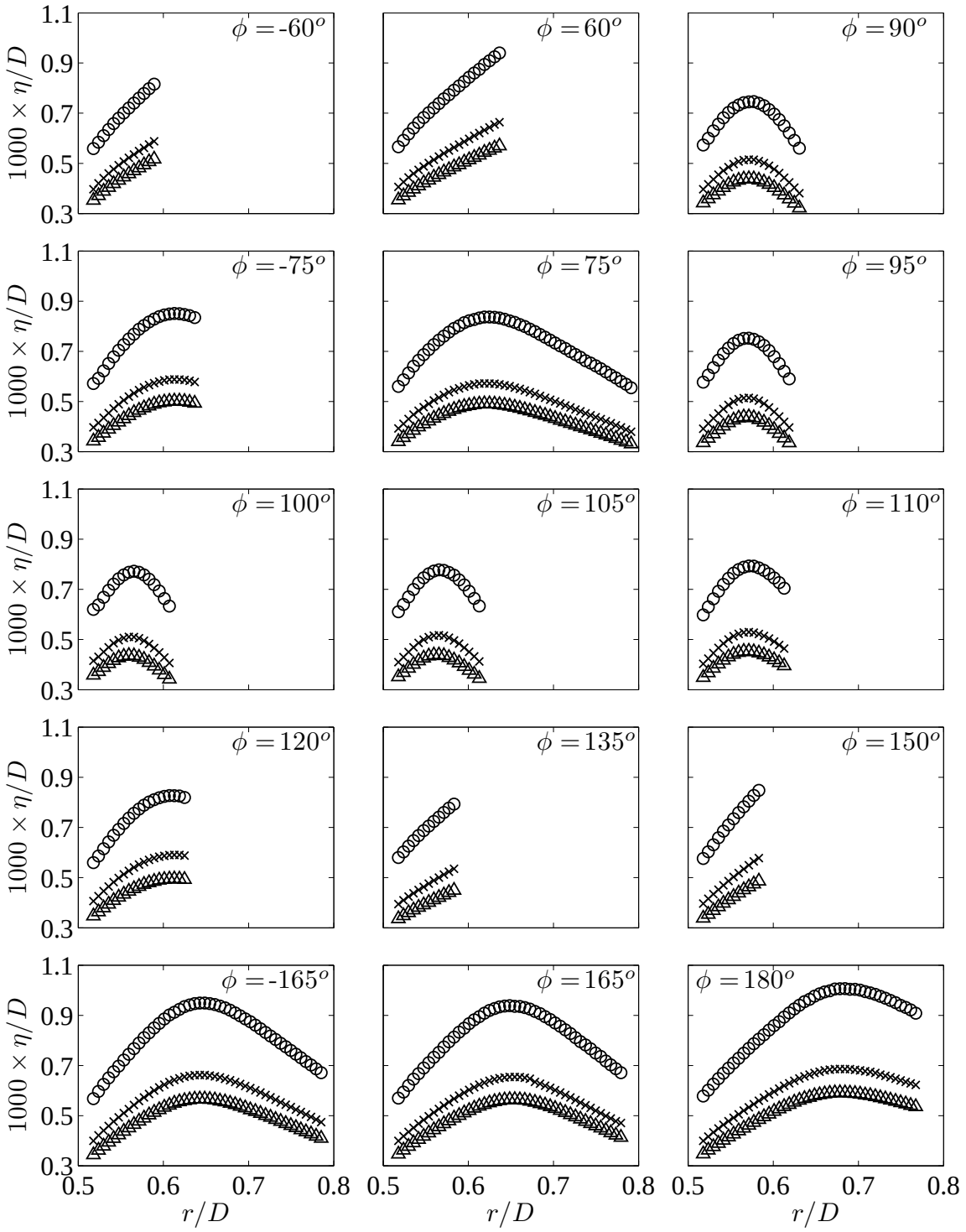

Figure 5.34 (Continued): Radial profiles of the Kolmogorov microscale at various azimuthal locations and for $Re =$ 50,000 (○), 100,000 (×) and 130,000 (△).

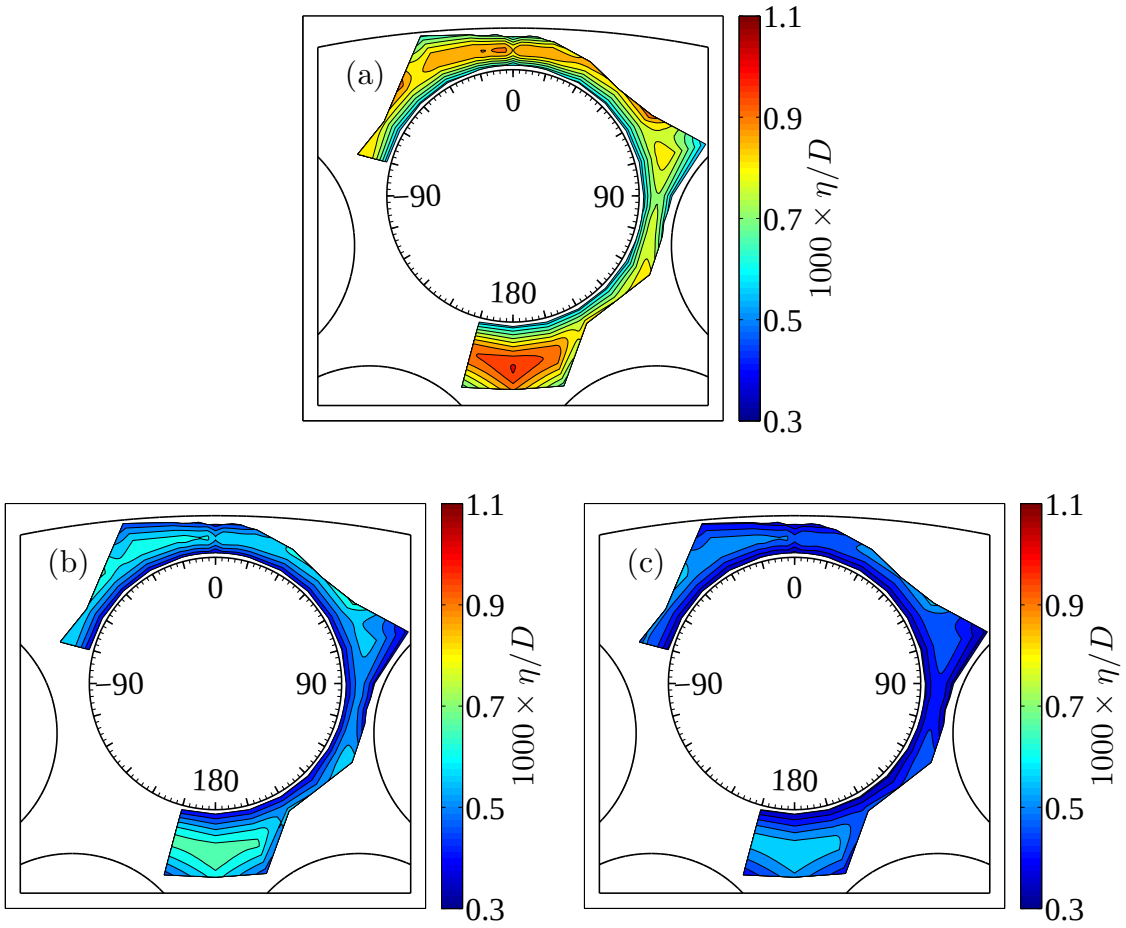

Figure 5.35: Isocontour plots of the Kolmogorov microscale for (a) $Re = 50,000$, (b) $Re = 100,000$, (c) $Re = 130,000$.

5.9 Wall shear stress variation

The variation of the wall shear stress τ_w, normalised by the corresponding azimuthal average $\tau_{w,av}$ are presented in figure 5.36. Measurements could only be taken in the range $-150^\circ \leq \phi \leq 150^\circ$ because of restrictions imposed by the rotary traverse and the mounting bracket supporting the Preston tube. The values of τ_w outside this range were estimated by extrapolation, as shown in the figure. The average wall shear stress was calculated by numerical integration of τ_w over the entire azimuthal range; its values were 0.532, 1.696 and 2.698 Pa for Re = 50,000, 100,000 and 130,000, respectively. $\tau_w/\tau_{w,av}$ reached local minima in the narrow gap regions and local maxima in the open flow regions. This is consistent with observations made earlier that the velocity gradient near the rod surface increased from the gap regions toward the open flow regions. In addition, there was no measurable effect of Reynolds number on the normalised wall shear stress variation.

Solving the momentum equations in CFD analysis usually requires a knowledge of the axial pressure loss, which then suggests assumption of a friction factor. In this study, the average friction factor was calculated as

$$f = 4\left(\frac{2\tau_{w,av}}{\rho U_b^2}\right). \tag{5.5}$$

Although in reactor design it is practical to define f as above, several studies in rod bundles commonly used a friction factor $\hat{f}$ based on the subchannel bulk velocity

$$\hat{U_b} = \frac{1}{A_r}\int_0^{\pi}\int_0^{y_m} U(r,\phi)\; r\; dr\; d\phi\;, \tag{5.6}$$

where A_r is the area bounded by the rod surface and the surrounding line of maximum velocity. Measurements of f in this study and some past experimental studies in rod bundles were plotted against the Reynolds number in figure 5.37. The same figure also shows the variation of f in smooth pipe flows, as determined from the Colebrook [1939] correlation

$$\frac{1}{\sqrt{f}} = -2\log_{10}\left(\frac{\epsilon}{37D_h} + \frac{2.51}{Re\sqrt{f}}\right)\;, \tag{5.7}$$

after setting the dimensionless roughness height ϵ/D_h to zero. In all cases, the average friction factor decreased as the Reynolds number increased, in conformity with the

literature. The values of the friction factor in this experiment are presented in table 5.1 and were higher than those for the smooth pipe flows and some of the past experimental studies presented. This is attributed to the following causes: a) the present measurements of τ_w extended over the central rod, where the speed would be higher than in the side subchannels and so wall shear stress level might be elevated as well; b) the pitch-to-diameter ratio of the present study (1.149) was lower than those of the previous ones (1.19, 1.20 and 1.22 for the measurements by Subbotin et al. [1971], Trupp and Azad [1975] and Kjellström [1974], respectively) and so, the wall shear stress would be higher for the same bulk velocity; c) additional stresses due to large-scale structures.

Re	A_r (m^2)	$\tau_{w,av}$ (Pa)	U_{max} (m/s)	U_b (m/s)	$\hat{U}_b$ (m/s)	f	$\hat{f}$
50,000	0.0064	0.532	14.29	10.65	11.34	0.0321	0.0283
100,000	0.0064	1.696	28.42	21.33	23.00	0.0255	0.0219
130,000	0.0064	2.698	37.11	27.70	30.02	0.0240	0.0205

Table 5.1: Summary of the wall shear stress and friction factor measurement

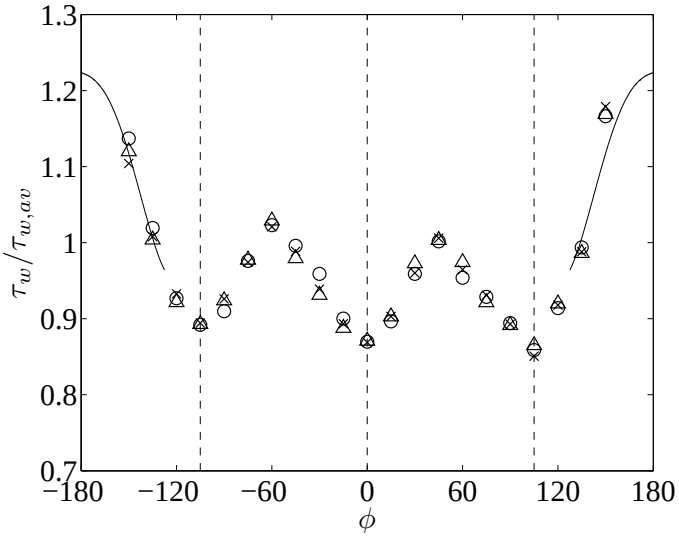

Figure 5.36: Azimuthal wall shear stress variations for $Re = 50,000$ ($\bigcirc$), $100,000$ ($\times$) and $130,000$ ($\triangle$). The dashed lines represent the narrow gap locations and the solid lines are extrapolation curves.

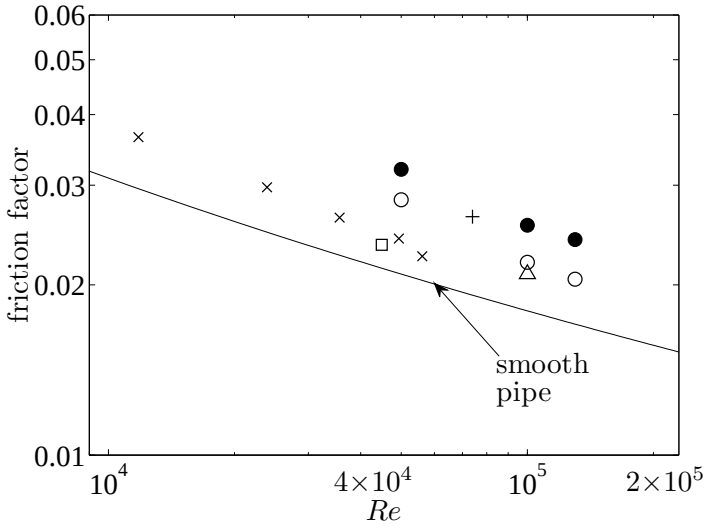

Figure 5.37: Friction factors in the present study f (●) and $\hat{f}$ (○) and those by Subbotin et al. [1971] (□), Kjellström [1974] (△), Trupp and Azad [1975] (×) and Ouma and Tavoularis [1991] (+)

5.10 Comparison with pipe flows

In this section, present turbulence measurements are compared with corresponding results in fully developed pipe flows of air. The pipe flow data were obtained by Laufer [1954] using hot-wire anemometry in a test section that had an inner diameter of 0.254 m and a length of 4.88 m; measurements were reported for two Reynolds numbers, equal to 50,000 and 500,000. For the comparison, the radial distance from the wall will be denoted as y and it will be normalised by y_m, which indicates the radial distance between the rod wall and the subchannel midline for the rod bundle results and the pipe radius for the pipe flow results.

Figure 5.38 shows profiles of the normalised mean axial velocity $\overline{U}$ in the present experiments and in pipe flow. $\overline{U}$ was normalised by the local maximum axial velocity U_m, which also indicates the centreline mean velocity for the pipe flow results. In all the cases shown, a small increase of $\overline{U}/U_m$ in the experimental data as the Reynolds number became larger could be observed and was more noticeable at radial distances close to the rod. This suggests that locally the wall layer was indeed thinner at larger Reynolds number. When all the results are viewed as a whole, the radial profiles of $\overline{U}/U_m$ obtained at each azimuthal location generally lied between the two sets of pipe

data.

Radial profiles of the normalised r.m.s fluctuating velocities u', u'_r and u'_ϕ are presented in figures 5.39, 5.40 and 5.41, respectively. These velocities were nondimensionalised by the local friction velocity calculated as $U_\tau = \sqrt{\tau_w/\rho}$. Typically, u'/U_τ decreased from the closest radial distance from the rod toward the midlines of the subchannels, which is also the case for the pipe data. The experimental u'/U_τ showed a measurable dependence on Reynolds number but at some azimuthal locations the effect of Reynolds number appeared to be weaker at the midline of the subchannel in conformity with pipe flows.

In most cases, the radial profiles of u'_r/U_τ lied at roughly 10% below the pipe data obtained at Re = 50,000, which may be attributed to the anisotropy in the radial normal Reynolds stresses. Generally, u'_r/U_τ was highest at the measuring position that was closest to the rod and decreased toward the subchannel centreline. A similar trend could also be observed in the pipe data. As the Reynolds number became larger, u'_r/U_τ seemed to increase by a relatively small amount.

Like u'/U_τ and u'_r/U_τ, the radial distributions of u'_ϕ/U_τ decreased from the measuring position closest to the surface of the rod toward the midlines of the subchannels. At most azimuthal locations presented, the profiles of u'_ϕ/U_τ lied below those of the pipe data and the values at the centerlines seemed much closer to those of pipe flows. All of these were not true in the rod-rod gap where the profiles of the measured u'_ϕ/U_τ appeared to be nearly constant over the entire range of the radial distance. Reynolds number had the same effect on u'_ϕ/U_τ in all the channels including in the rod-rod gap and, like the other two normalised r.m.s fluctuating velocities, u'_ϕ/U_τ also was larger for higher Reynolds number.

The radial distributions of the normalised Reynolds shear stresses $\overline{uu_r}$ in the experimental study and in pipe flow are illustrated in figure 5.42. The Reynolds shear stresses were normalised by the friction velocity squared. The present $\overline{uu_r}/U_\tau^2$ were generally lower than corresponding results in pipe flows. Moreover, the present data indicated an increase in $\overline{uu_r}/U_\tau^2$ with increasing Reynolds number, in agreement with the pipe flow data, which showed the same trend, albeit in a very weak form.

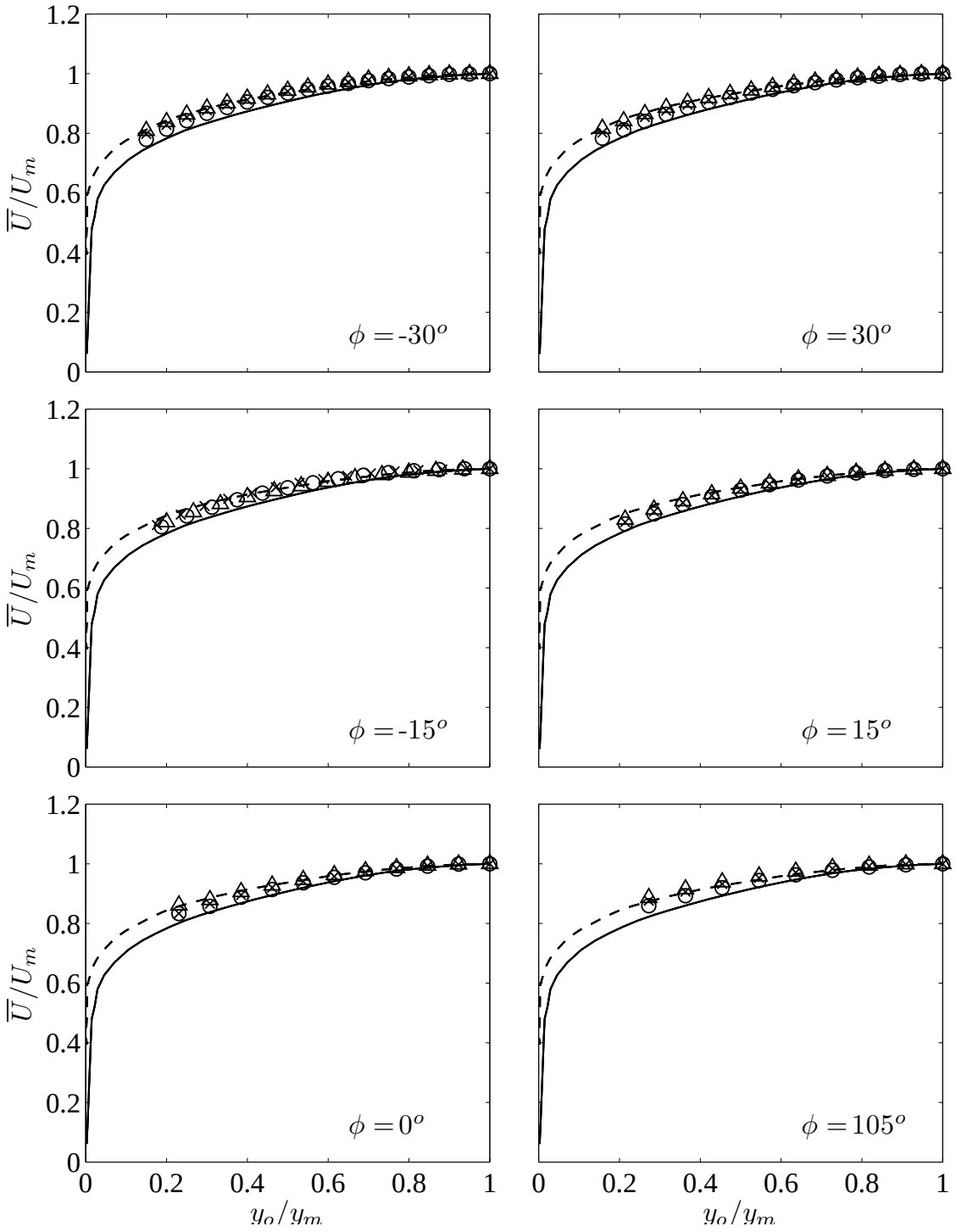

Figure 5.38: Radial profiles of the normalised mean axial velocity. Present experiment: $Re = 50,000$ ($\bigcirc$), $100,000$ ($\times$) and $130,000$ ($\triangle$). Pipe flow: $Re = 50,000$ (—) and $500,000$ ($--$).

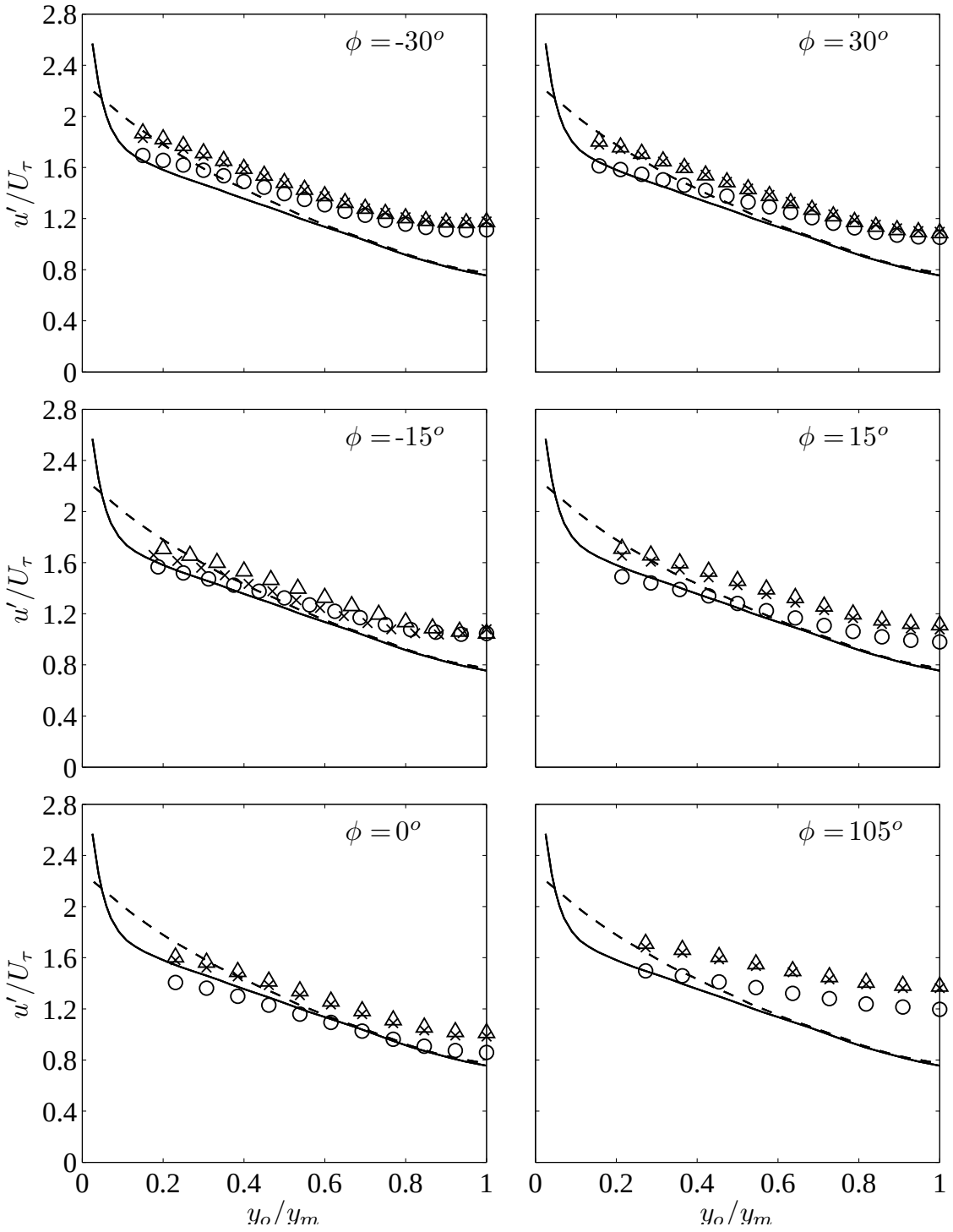

Figure 5.39: Radial profiles of the normalised axial fluctuating velocity. Present experiment: $Re = 50,000$ ($\bigcirc$), $100,000$ ($\times$) and $130,000$ ($\triangle$). Pipe flow: $Re = 50,000$ (—) and $500,000$ ($--$).

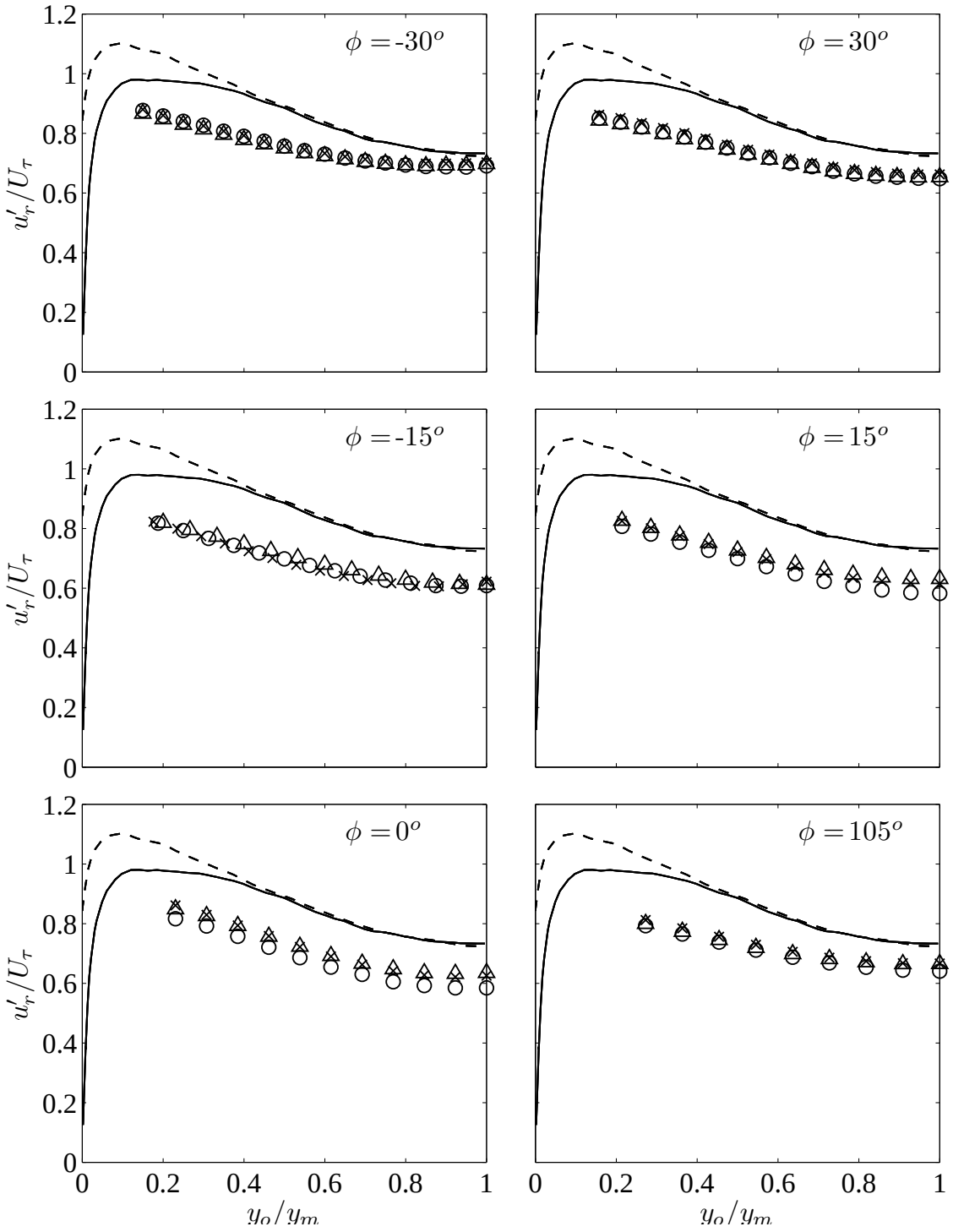

Figure 5.40: Radial profiles of the normalised radial fluctuating velocity. Present experiment: $Re = 50,000$ ($\bigcirc$), $100,000$ ($\times$) and $130,000$($\triangle$). Pipe flow: $Re = 50,000$ (—) and $500,000$ ($--$).

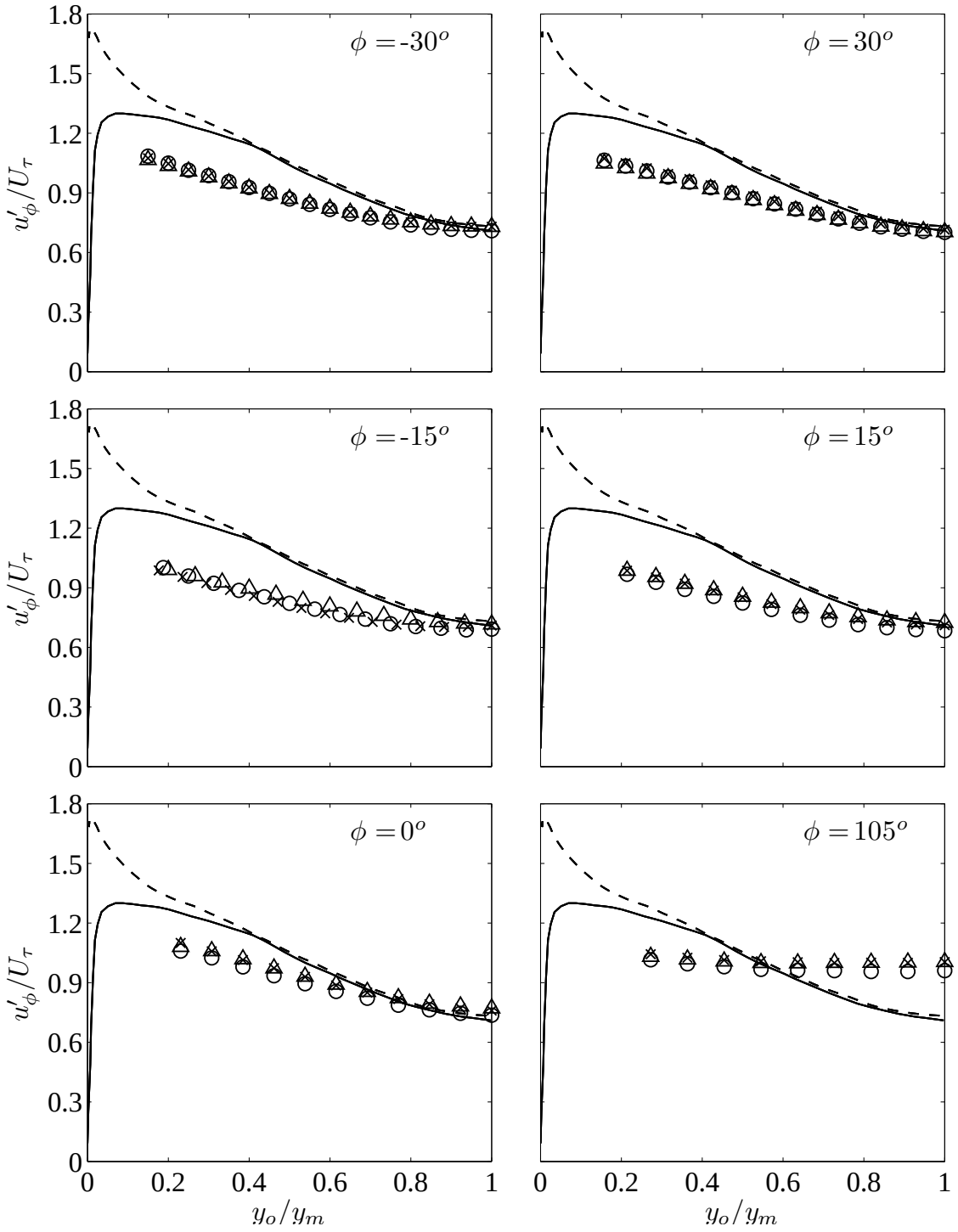

Figure 5.41: Radial profiles of the normalised azimuthal fluctuating velocity. Present experiment: $Re = 50,000$ ($\bigcirc$), $100,000$ ($\times$) and $130,000$ ($\triangle$). Pipe flow: $Re = 50,000$ (—) and $500,000$ ($--$).

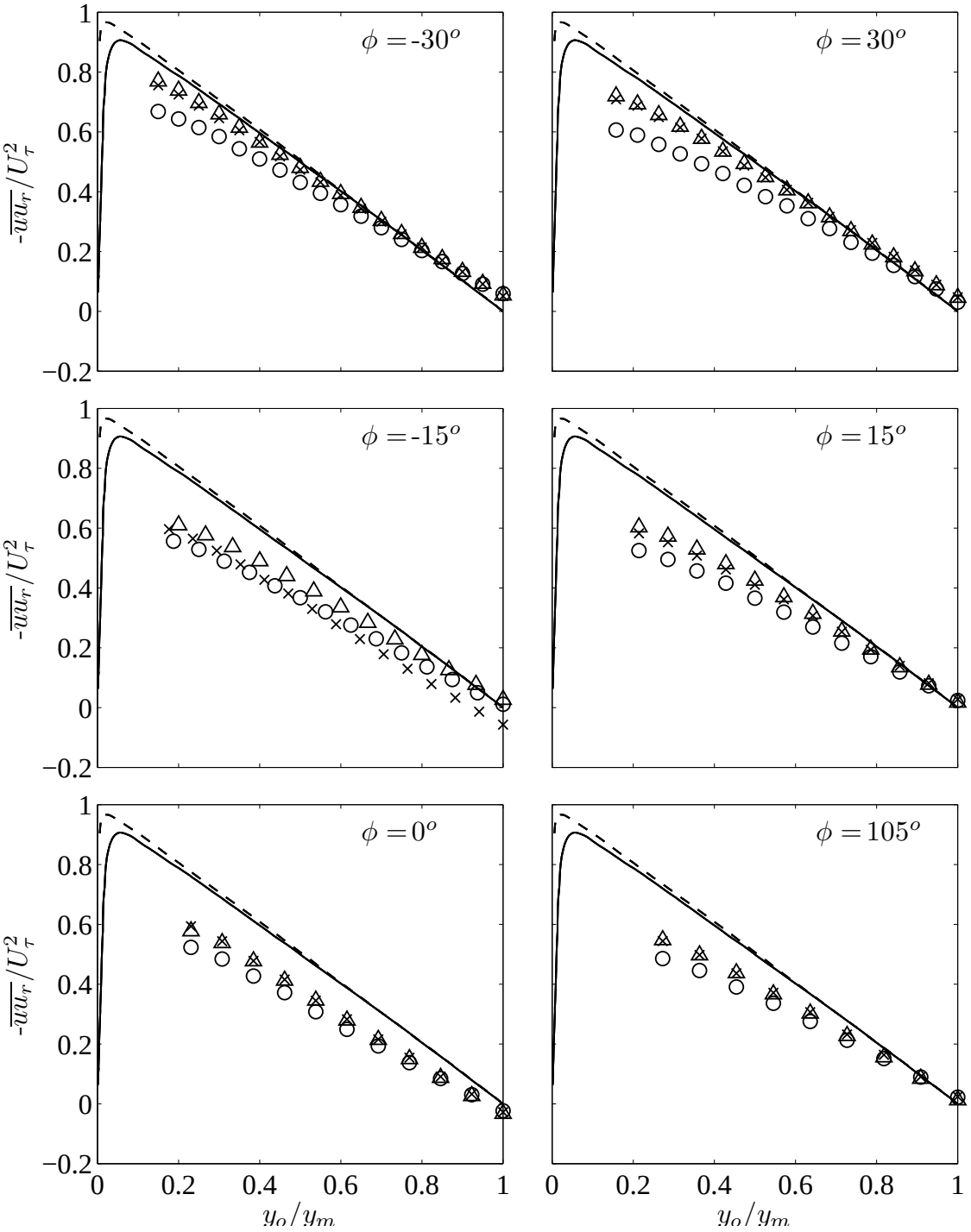

Figure 5.42: Radial profiles of the normalised radial Reynolds shear stress. Present experiment: $Re = 50,000$ (○), $100,000$ (×) and $130,000$ (△). Pipe flow: $Re = 50,000$ (—) and $500,000$ (−−).

5.11 Coherent structure characteristics

Evidence of coherent vortex streets has been reported in compound rectangular channels connected by slots, eccentric annular flows and flows in tightly packed rod bundles. In these geometries, strong velocity gradient on both sides of the narrow gap causes shear stress, which creates flow instability that generates counter-rotating alternating vortices on each side of the gap (figure 5.43). These vortices are believed to start small but become larger further downstream depending on the subchannel size.

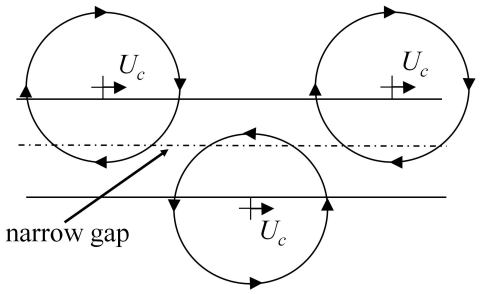

Figure 5.43: Sketch of idealized gap vortex street, according to Meyer and Rehme [1994]. Sketch from Choueiri [2014].

In the case of tightly packed rod bundles, such as the CANDU rod bundle, which contains multiple interconnected subchannels, the different gap vortex streets are believed to form a vortex network [Tavoularis, 2011], which would synchronize cross-stream exchange between the subchannels adjacent to the narrow gaps. Several studies have found that the stream exchange tended to be quasi-periodic with a relatively low frequency, and so passage of coherent vortices could be detected from the spectrum of the cross-velocity fluctuations in the narrow gap regions where the effect of the coherent vortices would be more pronounced.

In this study, to determine the distance x from the inlet of the CANDU rod bundle model at which the coherent vortices start forming, the power spectra of the azimuthal velocity fluctuations at the midline of rod-wall gap were measured at several locations along the test section using cross-wires inserted from ports installed on the curved wall. These spectra are presented in figure 5.44. With the exception of the spectrum at $x/D = 2.41$, all other spectra show a strong peak at a relatively low frequency, which is indicative of the passage of coherent vortices. The peak frequency

of the spectra, as indicated in figure 5.45, decreased gradually as the flow developed and appeared to approach a constant asymptote at the two furthest downstream locations. The spectra from $x/D = 12.07$ to $x/D = 33.81$ nearly collapsed at higher frequencies and showed that the coherent fluctuations across the rod-wall gap were generally stronger further downstream. For the three Reynolds numbers investigated, the velocity spectrum at $x/D = 2.41$ was unique, as its peak frequency was considerably higher than those at other locations downstream. This peak is attributed to vortices generated at the inlet of the test section, possibly shed from the edges of the rods or the endplate ribs, rather than the gap vortex street, which was apparently not yet developed at that location.

Autocorrelation functions of the azimuthal velocity fluctuations in the centre of the rod-wall gap at $x/D = 33.81$ are shown in figure 5.46. This plot also shows strong periodicity of the signals, with a period that decreased with increasing Reynolds number. The present observations are consistent with previously published measurements by Baratto et al. [2006], who showed an autocorrelation coefficient in the rod-wall gap that has the same shape as the present one. The Strouhal number, defined as $St = f_p D/U_b$ and plotted in figure 5.47, was found to be insensitive to Reynolds number and to approach a constant of about 0.24 towards the end of the test section. This suggests that, once formed, the overall structure of the vortex network was independent of Reynolds number in agreement with a recent study by Choueiri and Tavoularis [2015], where the coherent structure characteristics were proven to be mostly affected by the eccentricity (W/D or P/D in the case of rod bundles).

The convection speed U_c and the wavelength $\lambda_c = U_c/f_p$ of the coherent vortices near the exit of the test section were measured for several Reynolds numbers in the range from 50,000 to 130,000. As illustrated in figure 5.48, the ratio U_c/U_b was essentially constant and equal to about 1.16. λ_c appeared to be about $5D$ and insensitive to Reynolds number as shown in figure 5.49, in agreement with Meyer and Rehme's [1995] conclusion that the axial spacing of vortices in compound channels connected by slots was a function of the geometry and independent of the Reynolds number. Guellouz and Tavoularis [2000] also drew a similar conclusion and found that the magnitude of λ_c in their test rig was roughly $4.5D$ for $W/D = 1.15$.

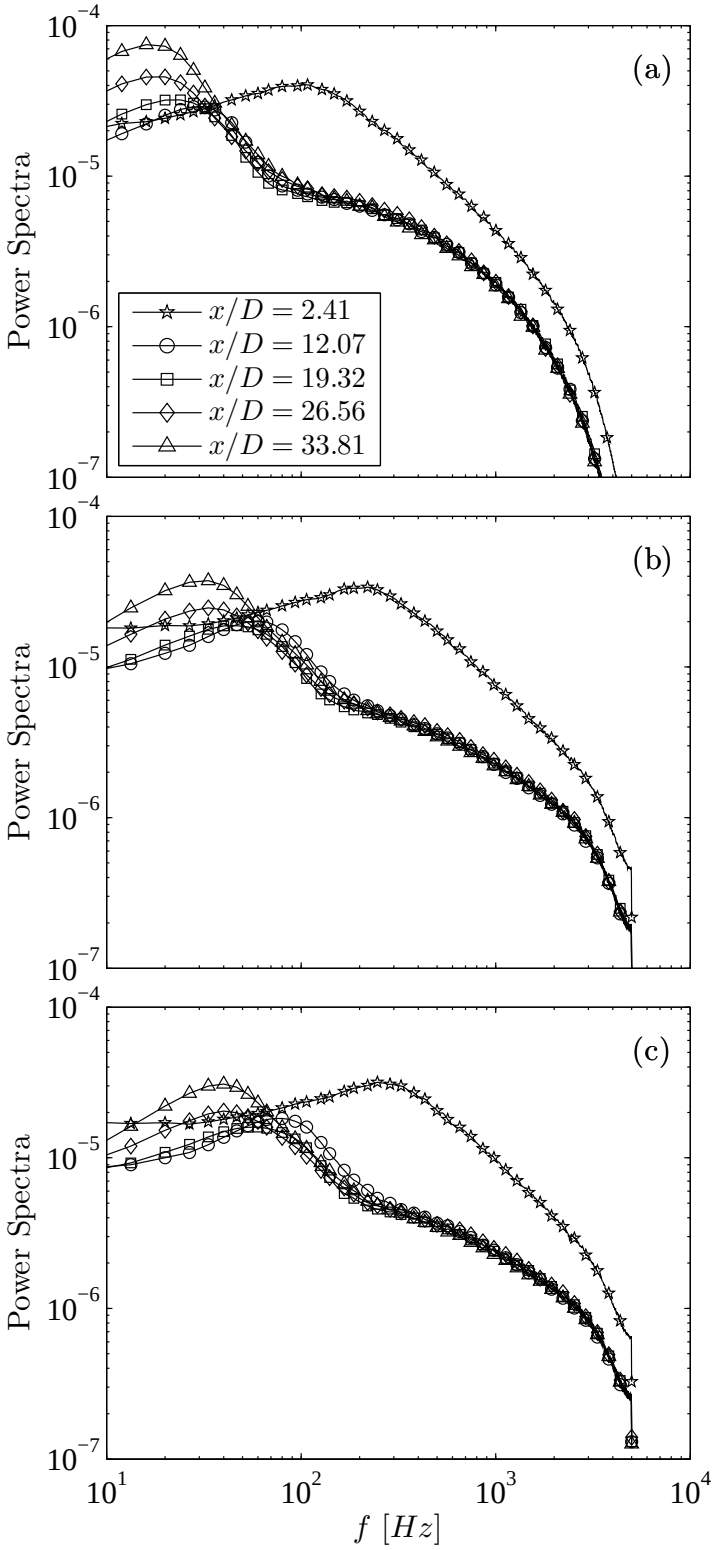

Figure 5.44: Cross-flow power spectra in the centre of the rod-wall gap along the test section for (a) $Re = 50,000$, (b) $Re = 100,000$ and (c) $Re = 130,000$.

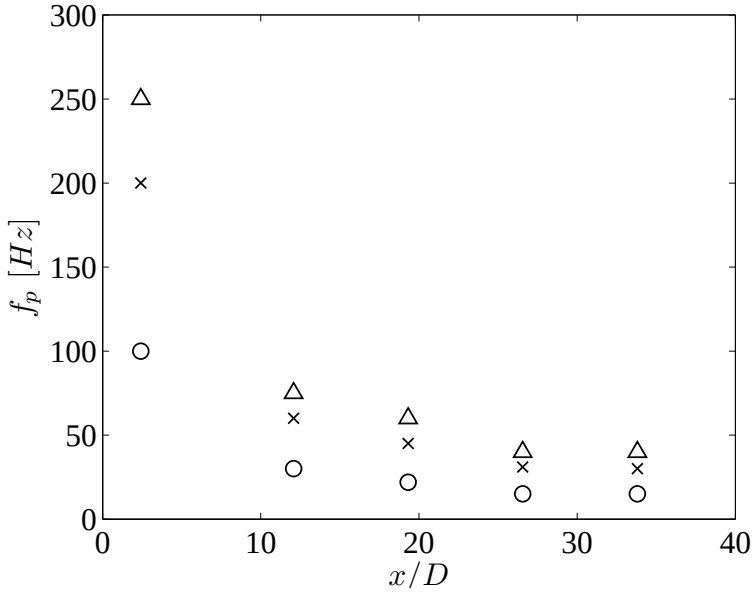

Figure 5.45: Peak frequencies of the cross-flow power spectra for $Re = 50,000$ ($\bigcirc$), $100,000$ ($\times$) and $130,000$ ($\triangle$).

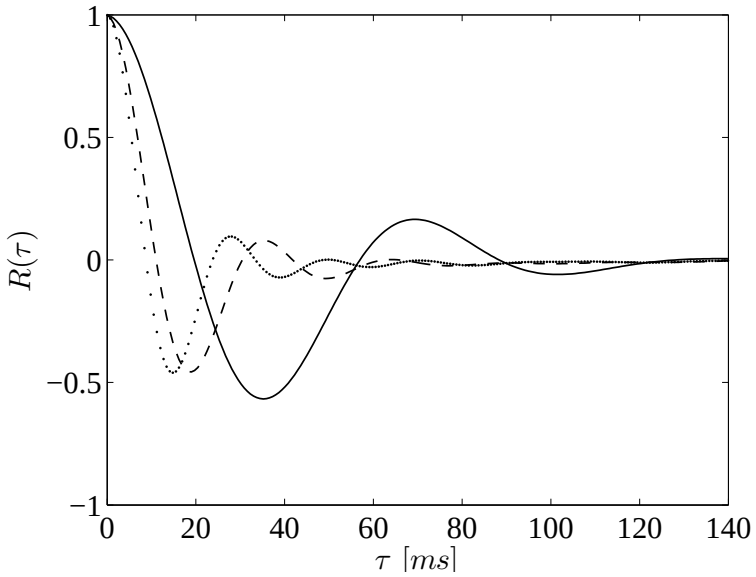

Figure 5.46: Autocorrelation coefficient of the cross velocity fluctuations at $x/D = 33.81$ for $Re = 50,000$ (—), $100,000$ ($--$) and $130,000$ ($\cdots$).

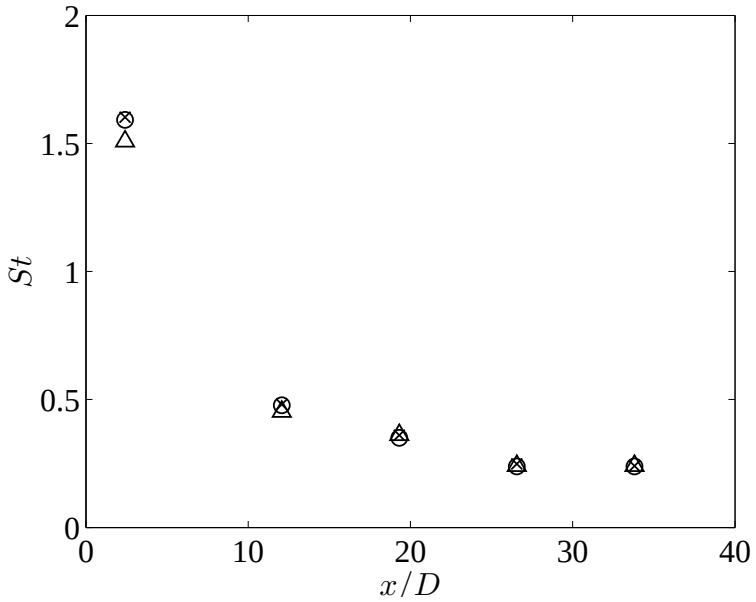

Figure 5.47: Strouhal number variation along the test section for $Re = 50,000$ ($\bigcirc$), $100,000$ ($\times$) and $130,000$ ($\triangle$).

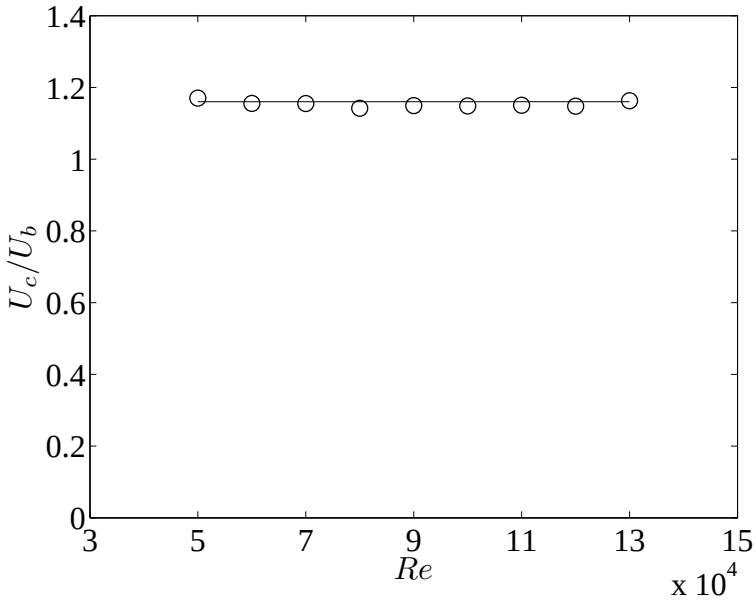

Figure 5.48: Variation of the normalized convection speed of the coherent vortices with Reynolds number. Solid line indicates $U_c/U_b = 1.16$.

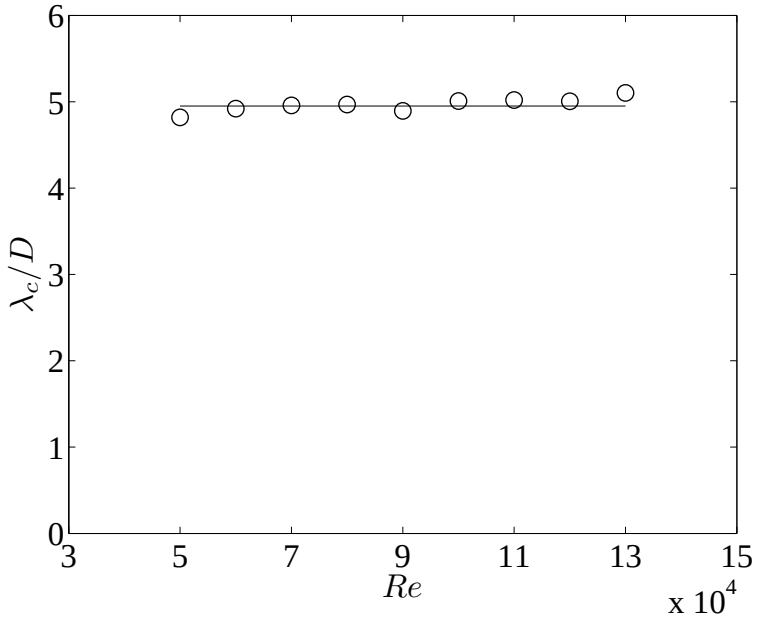

Figure 5.49: Variation of the normalised wavelength of the coherent vortices with Reynolds number. Solid line indicates $\lambda_c/D = 4.95$.

Chapter 6

Conclusion

6.1 Summary of the results

In the first part of this study, we investigated the turbulent flow statistics in the subchannels around the middle outer rod of a large-scale model of a 60° section of the CANDU rod bundle for three distinct Reynolds numbers. Measurements of the mean axial velocity, the Reynolds stresses, the turbulent kinetic energy and the anisotropy tensors were presented. Statistics of the integral length scales and the fine-scale turbulence were also included. The wall shear stress and the friction factor were measured and reported. The key conclusions of this work are as follows.

- The magnitudes of the turbulence stresses were generally found to be greater in the open channels than in the gaps.
- In general, the normalized mean and r.m.s. axial flow velocities were in good agreement with pipe flow results, whereas the normalized radial and azimuthal r.m.s velocities and the normalized Reynolds shear stress were lower than pipe flow values.
- The axial and azimuthal Reynolds stresses in the rod-rod gap were generally larger than their corresponding values in the rod-wall gap. The axial and azimuthal r.m.s velocities were also higher in the rod-rod gap and tended to deviate rather significantly from pipe data. This was attributed to a stronger effect of gap vortex streets in the rod-rod gap in comparison to the rod-wall gap.
- Most of the dimensionless turbulence statistics presented showed some dependence on Reynolds number. The sensitivity to Reynolds number was stronger for indicators of the fine turbulence structure.

- The normalized wall shear stress reached minima in the narrow gaps and maxima in the larger channels, and was insensitive to Reynolds number. The friction factor tended to decrease with increasing Reynolds number in conformity with pipe flow data, but its magnitude was higher in this experiment than in smooth pipes.

In the second part of this work, we identified several flow indicators that are relevant to the formation of gap vortex streets in a large-scale model of a CANDU rod bundle and examined their dependence on Reynolds number. These flow indicators were the frequency of cross-stream velocity pulsations between the subchannels adjacent to the rod-wall gap, the corresponding Strouhal number and the autocorrelation coefficients of these flow pulsations. The characteristics of the vortex street such as the convection speed and the distance between two consecutive coherent vortices were also studied. The main findings are as follows.

- In this model of the CANDU rod bundle, the coherent vortex street formed at a downstream location between $x/D = 2.4$ and 12.1.

- The frequency of the cross-flow pulsations was found to be proportional to Reynolds number and decreased as the flow developed but approached an asymptotic constant toward the end of the test section. A similar trend was observed in the corresponding Strouhal number, which appeared to be insensitive to Reynolds number.

- The normalized convection speed of the coherent vortices and their wavelength appeared to be independent of Reynolds number.

6.2 Main contribution and recommendations for future work

The present work follows numerous studies on similar topics by several authors over the years. However, this is the first time the effect of Reynolds number on the turbulence statistics and on the development of vortex networks in a large-scale model of the CANDU rod bundle has been documented experimentally in detail. This work provides an extensive collection of experimental data, which may serve for the

validation of computational studies. From a technical point of view, this facility was equipped with state of the art hardware and software that were not widely available 15 to 25 years ago. Therefore, we were not restricted by limitations such as low computer memory, the lack of complex algorithms that could handle large matrices or the lack of sophisticated and autonomous measurement systems that many past studies had to contend with. For that reason, we were able to efficiently acquire a very large amount of data and achieved better data convergence and more accurate turbulence statistics.

More improvements and modifications could be made to the facility to tackle other areas of studies currently not sufficiently documented. Some of these modifications are currently underway and will address for the most part the effect of transients on the structure of turbulence. An area that deserves additional investigation is the effect of transient on the development of vortex network. Further experimental investigation of the critical Reynolds number at which gap vortex streets start to develop would be beneficial. Experiments focusing on whether the flow pulsations in two distinct gaps located at a relatively close distance are synchronized may provide some insight on the interactions between the gap vortex streets. Effect of pressure tube creep, and fuel rod displacement caused by flow-induced vibrations in nuclear reactor should also be investigated more thoroughly. A final recommendation would be to conduct studies with spacers blocking the flow in some of the gaps entirely or partially and observe how that would affect the flow in subchannels, particularly in the gaps left unobstructed.

References

S. Bailey. *The interaction of a wing-tip vortex and free-stream turbulence.* PhD Dissertation, University of Ottawa, Ottawa, Canada, 2006.

F. Baratto, S. Bailey, and S. Tavoularis. Measurements of frequencies and spatial correlations of coherent structures in rod bundle flows. *Nuclear Engineering and Design*, 236(17):1830–1837, 2006.

H. Bruun. *Hot-Wire Anemometry: Principles and Signal Analysis.* Oxford University Press, Oxford; New York, 1995. ISBN 0198563426.

P. Carajilescov and N. Todreas. Experimental and analytical study of axial turbulent flows in an interior subchannel of a bare rod bundle. *Journal of Heat Transfer*, 98 (2):262–268, 1976.

D. Chang and S. Tavoularis. Unsteady numerical simulations of turbulence and coherent structures in axial flow near a narrow gap. *Journal of Fluids Engineering*, 127(3):458–466, 2005.

D. Chang and S. Tavoularis. Numerical simulation of turbulent flow in a 37-rod bundle. *Nuclear Engineering and Design*, 237(6):575–590, 2007.

D. Chang and S. Tavoularis. Numerical simulations of developing flow and vortex street in a rectangular channel with a cylindrical core. *Nuclear Engineering and Design*, 243:176–199, 2012.

G. Choueiri. *Experimental investigations of flow Development, gap instability and gap vortex street generation in eccentric annular channels.* PhD Dissertation, University of Ottawa, Ottawa, Canada, 2014.

G. H. Choueiri and S. Tavoularis. Experimental investigation of flow development and gap vortex street in an eccentric annular channel. part 1. overview of the flow structure. *Journal of Fluid Mechanics*, 752:521–542, 2014.

G. H. Choueiri and S. Tavoularis. Experimental investigation of flow development and gap vortex street in an eccentric annular channel. part 2. effects of inlet conditions, diameter ratio, eccentricity and reynolds number. *Journal of Fluid Mechanics*, 768: 294–315, 2015.

C. F. Colebrook. Turbulent flow in pipes, with particular reference to the transition region between the smooth and rough pipe laws. *Journal of the Instituion of Civil Engineers*, 11(4):133–156, 1939.

J. Downie, R. Jordinson, and F. Barnes. On the design of three-dimensional wind tunnel contractions. *Aeronautical Journal*, 88:287–295, 1984.

R. S. El Tahry. Discussion of the role of coherent structures. In *Whither Turbulence? Turbulence at the Crossroads*, pages 170–191. Springer, 1990.

M. Fakory and N. Todreas. Experimental investigation of flow resistance and wall shear stress in the interior subchannel of a triangular array of parallel rods. *Journal of Fluids Engineering*, 101(4):429–434, 1979.

A. Gosset and S. Tavoularis. Laminar flow instability in a rectangular channel with a cylindrical core. *Physics of Fluids*, 18(4):044108, 2006.

M. Guellouz and S. Tavoularis. Heat transfer in rod bundle subchannels with varying rod-wall proximity. *Nuclear Engineering and Design*, 132(3):351–366, 1992.

M. Guellouz and S. Tavoularis. The structure of turbulent flow in a rectangular channel containing a cylindrical rod-part 1: Reynolds-averaged measurements. *Experimental Thermal and Fluid Science*, 23(1):75–91, 2000.

M. S. Guellouz. Heat transfer in rod bundle subchannels. Master Dissertation, University of Ottawa, Ottawa, Canada, 1989.

D. Gunn and C. Darling. Fluid flow and energy losses in non-circular conduits. *Trans. Inst. Chem. Eng*, 41:163–173, 1963.

D. Home, G. Arvanitis, M. Lightstone, and M. Hamed. Simulation of flow pulsations in a twin rectangular sub-channel geometry using unsteady reynolds averaged navier–stokes modelling. *Nuclear Engineering and Design*, 239(12):2964–2980, 2009.

J. Hooper. Developed single phase turbulent flow through a square-pitch rod cluster. *Nuclear Engineering and Design*, 60(3):365–379, 1980.

A. F. Hussain. Coherent structuresreality and myth. *Physics of Fluids (1958-1988)*, 26(10):2816–2850, 1983.

T. Ikeno and T. Kajishima. Analysis of dynamical flow structure in a square arrayed rod bundle. *Nuclear Engineering and Design*, 240(2):305–312, 2010.

F. Jerome, D. Guitton, and R. Patel. Experimental study of the thermal wake interference between closely spaced wires of a x-type hot-wire probe. Technical report, DTIC Document, 1970.

B. Kjellström. Studies of turbulent flow parallel to a rod bundle of triangular array. Technical report, Aktiebolaget Atomenergi, Studsvik (Sweden), 1974.

T. Krauss and L. Meyer. Experimental investigation of turbulent transport of momentum and energy in a heated rod bundle. *Nuclear Engineering and design*, 180 (3):185–206, 1998.

J. Laufer. The structure of turbulence in tully developed pipe flow. Technical report, National Advisory Committee for Aeronautics, Washington, DC, NACA Report, 1954.

M. Lesieur. *Turbulence in Fluids*, volume 84. Springer Science & Business Media, 2008.

L. Meyer. From discovery to recognition of periodic large scale vortices in rod bundles as source of natural mixing between subchannelsa review. *Nuclear Engineering and Design*, 240(6):1575–1588, 2010.

L. Meyer and K. Rehme. Large-scale turbulence phenomena in compound rectangular channels. *Experimental Thermal and Fluid Science*, (8):286–304, 1994.

L. Meyer and K. Rehme's. Periodic vortices in flow through channels with longitudinal slots or fins. In *Proceedings of the Tenth Symposium on Turbulent Shear Flows*, pages 14–16, 1995.

B. Ouma and S. Tavoularis. Flow measurements in rod bundle subchannels with varying rod-wall proximity. *Nuclear Engineering and Design*, 131(2):193–208, 1991.

V. Patel. Calibration of the preston tube and limitations on its use in pressure gradients. *Journal of Fluid Mechanics*, 23(01):185–208, 1965.

E. Rind and S. Tavoularis. Design, instrumentation and performance of a large-scale rod-bundle air flow facility. Technical report, University of Ottawa, Ontario, Canada, 2012.

A. Strohl and G. Comte-Bellot. Aerodynamic effects due to configuration of x-wire anemometers. *Journal of Applied Mechanics*, 40(3):661–667, 1973.

V. Subbotin, P. Ushakov, Y. D. Levchenko, and A. Aleksandrov. Velocity fields in turbulent flow past rod bundles. Technical report, Inst. of Physics and Energetics, Obninsk, USSR, 1971.

S. Tavoularis. *Measurement in Fluid Mechanics*. Cambridge University Press, Cambridge; New York, 2005. ISBN 9780521138390.

S. Tavoularis. Rod bundle vortex networks, gap vortex streets, and gap instability: A nomenclature and some comments on available methodologies. *Nuclear Engineering and Design*, 241(7):2624–2626, 2011.

A. C. Trupp and R. Azad. The structure of turbulent flow in triangular array rod bundles. *Nuclear Engineering and Design*, 32(1):47–84, 1975.

J. Wyngaard. Spatial resolution of the vorticity meter and other hot-wire arrays. *Journal of Physics E: Scientific Instruments*, 2(11):983, 1969.